UNIVERSITÄT  OSNABRÜCK

Surface functionalization of nanoparticles for probing and manipulation of proteins inside living cells

Dissertation

Presented to the department of Biology/Chemistry, University of Osnabrück

in partial fulfillment of the requirements for the degree of

"Doctor Rerum Naturalium"

Domenik Liße

Osnabrück

November 2013

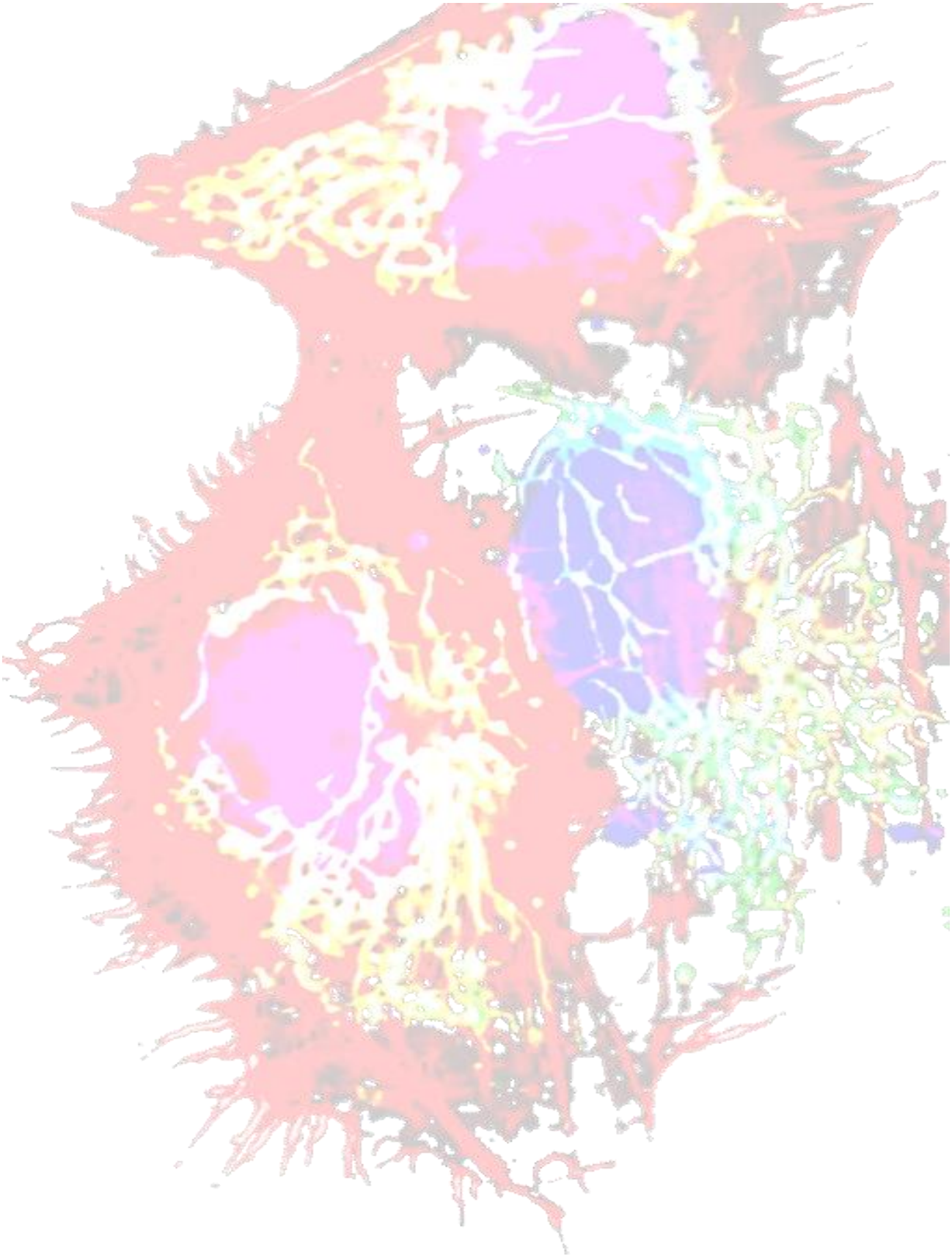

Für meine Mutter, Brigitte

Danksagung

Ich danke allen denjenigen, die zu dem erfolgreichen Gelingen dieser Arbeit beigetragen haben.

Insbesondere, Herrn Prof. Dr. Jacob Piehler, Dir danke ich für das besondere Vertrauen und der Möglichkeit auf einem interdisziplinären und spannenden Thema zu promovieren. Darüber hinaus für die Inspirationen und vor allem für die Freiheiten während der gesamten Promotion, sowie für die stetige Bereitschaft auch interdisziplinär privat zu diskutieren. „*Science is Fun*“

Zudem, Herrn Prof. Dr. Günther Jeromin, Ihnen möchte ich an dieser Stelle noch einmal herzlich danken für das Vertrauen und den Beistand in besonders schweren Zeiten. „*Vielen Dank*“

Den Franzosen – Dr. Fred, Dr. Mathieu & Mr. Prof. Dr. Maxime Dahan, sehr sehr schön war es bei Euch. Die spannende und fruchtvolle Zusammenarbeit hat mir stets viel Spaß gemacht. „*to be continued*“

Gabi und Hella für die technische Unterstützung und dafür dass Ihr einfach nett seid.

Und natürlich den Rest der Truppe für den wissenschaftlichen Austausch und vieles mehr.

Frau Prof. Dr. Karin Busch und Verena Wilkens für die erfolgreiche Zusammenarbeit.

Christoph, OBi. und Felix für das geduldige Korrekturlesen dieser Arbeit.

Herrn Dr. Ing. Uli für das stets offene Ohr und die Unterstützung in so vielen Dingen.

Vera & OBe für die Freundschaft.

Table of Contents

I Introduction

1 Nanotechnology

"A biological system can be exceedingly small. Many of the cells are very tiny, but they are very active; they manufacture various substances; they walk around; they wiggle; and they do all kinds of marvelous things – all on a very small scale. Also, they store information. Consider the possibility that we too can make a thing very small which does what we want – that we can manufacture an object that maneuvers at that level."

(Richard P. Feynman in 1959)

On December 1959, at the California Institute of Technology *Richard P. Feynman* gave a talk titled "*There's plenty of room at the bottom*".[1] He presented a vision while talking about the challenge of manipulating and controlling things on the smallest scale. Feynman envisioned a technology, building smallest objects, based on known physical laws.

More than 50 years later, the technological vision of *Feynman* is termed nanotechnology and it is one of the most promising new technologies of the 21st century. The term nanotechnology was used for the first time by *Norio Taniguchi* in a 1974 conference to describe semiconductor processes. He stated: *"'Nano-technology' mainly consists of the processing of separation, consolidation, and deformation of materials by one atom or one molecule",*[2] and this still stands as the basic definition today.

Nowadays, nanotechnology basically means any technology performed on the nanometer scale. In nanotechnology, nanomaterials and nanodevices (nanosystems) are the result of the manipulation of atoms, molecules or larger entities in a user defined manner and with certain desired properties.[3] For the fabrication of synthetic nanomaterials and nanodevices, two main strategies are used.[4] In the "bottom-up" approach, nanosystems are constructed from the atomic or molecular level by chemical self-assembly. In contrast to "bottom-up" approaches, the strategy by which nanosystems are built from larger entities without atomic level control is called "top-down" approach. Typical applications of nanotechnology are in material science, nanoelectronics, medicine and healthcare, energy production, biology, chemistry, biotechnology, information

technology, food or the cosmetic industry. In all these fields, nanomaterials and nanodevices provide novel opportunities for the development of innovative applications.

Nanosystems are defined in a size range of 1 to 100 nm with at least one dimension less than 100 nm (National Nanotechnology Initiative).[5] The lower limit is set by the size of atoms (e.g. the smallest atom, hydrogen, with ~2.5 Å in diameter), since atoms are the smallest possible building blocks. The upper limit is given more or less arbitrarily by those sizes which allow characteristic phenomena to occur. These phenomena cannot be observed in larger entities or in the bulk of the same material and will only become pronounced as the size of the material decreases. Thus, the properties of solid nanomaterials can be substantially altered compared to that of the bulk material.[6] For example, the quantum efficiency of semiconductor nanomaterials (Quantum dots) yield highly efficient light emission that is far beyond what has been achieved from their bulk materials.[7]

Nanotechnology at the interface of biology is termed “bionanotechnology” or “nanobiotechnology”. Bionanotechnology is guided by studying how biological “nanomachines” work and adapting this knowledge into existing nanotechnologies or creating new ones. Nanobiotechnology, on the other hand, is a discipline in which nanotechnology is used to create novel materials and devices for investigating biological systems. Nanomaterials and nanodevices in nanobiotechnology are mostly derived from fundamentals of nanotechnology. Approaches of nanotechnology in biology are, for instance, bio micro/nano electromechanical systems (BIO-MEMS/NEMS) as highly sensitive biosensors for chemical and biochemical analysis and diagnostics,[8] nanolithography for advanced protein arrays.[9] Furthermore, functionalized colloidal nanomaterials, i.e. nanoparticles (NPs), are of growing interest. Nanoparticles are utilized in a wide range of approaches like biomedical applications and biomedical diagnostics,[10,11] as well as for probing and manipulation of proteins, cells, and whole organisms.[12-19] Their unique physicochemical properties provide the potential to generate new insights into how biological systems function.

2 Nanoparticles in cell biology

The unique properties and utility of NPs arise from several attributes. (I) Nanoparticles can be designed with tailored optical, electrical or magnetical properties or in combinations of these attributes.[20,21] (II) Nanoparticles typically utilized in cellular approaches are 10 – 20 nm in diameter and, thus similar in size with large biomolecules like proteins (Figure I.1).[22,23] In addition, nanoparticles often exhibit colloidal behavior comparable to that of proteins.

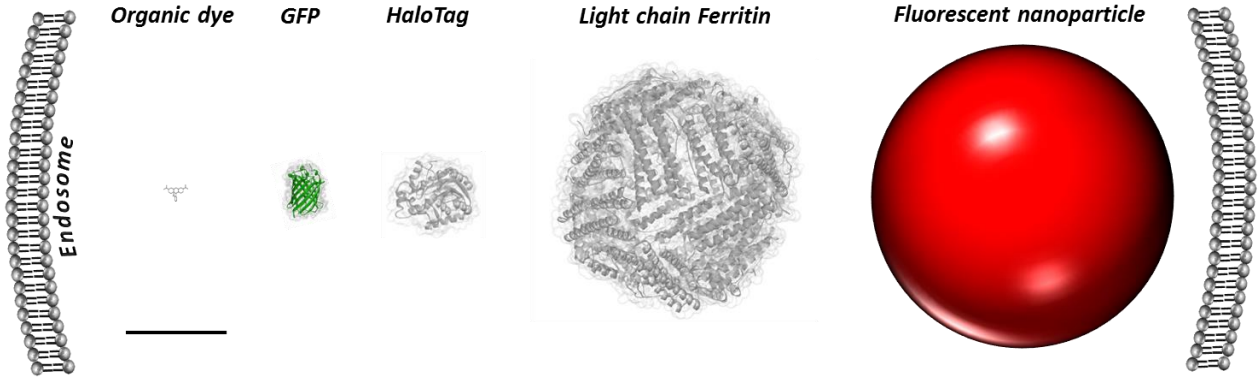

Figure I.1 Size comparison of a fluorescent nanoparticle and other chemical & biological molecules. Organic dye (~1 nm); GFP (~3 nm); HaloTag (~4 nm); Light chain Ferritin (12 nm); Fluorescent nanoparticle (15 nm);. All objects are compared within an endosome of 60 nm in diameter. Scale bar corresponds to 5 nm.

(III) For specific application, NPs can be functionalized with biologically active compounds.[24-28] These functionalities can encompass a variety of molecules such as small organic ligands, DNA, peptides, proteinaceous-ligands or enzymes. Functionalized NPs have been employed as fluorescent molecular probes, biosensors or actuators in several cellular applications. For example, quantum dots (QDs) bio-conjugates have been employed for cellular imaging.[12] In comparison with fluorescent proteins and organic fluorophores, which are widely spread in use for cellular fluorescence imaging, QDs provide ultra-bright and highly photo stable fluorescent probes. These unique properties enable fast, sensitive and long term imaging of biomolecules.[29] In addition, the size-dependent emission properties (1 - 10 nm in core diameter) of semiconductor materials facilitate multiplex imaging based on their narrow emission spectra.[30] Among other examples, QDs have been successfully employed for long term tracking of cell surface receptors with ultra-high spatial and temporal resolution.[31]

Unlike fluorescent proteins, which can be simply utilized by fusion to the protein of interest, the application of nanoparticles is much more complicated. In other words, laborious, as well as time-consuming coating and functionalization of nanoparticles has to be established for their often highly specialized application.[32] A general key challenge in the application of nanoparticles in biological fluids, i.e. blood, serum or the cytoplasm, derives from their large fraction of surface atoms per total volume and thus large surface energies making them highly reactive.[33] This susceptibility to unwanted intermolecular interactions further complicated the applications of NPs as will be discussed in more detail below.

2.1 Fabrication and solubilization of nanoparticles

Mostly, nanoparticles are synthesized utilizing "bottom-up" approaches with atoms or molecules as building blocks. By contrast, protein based nanoparticles such as Ferritin[34] and analogues[35] or virus capsids[36] can be produced recombinantly or purified from biological samples. In "bottom-up" approaches, nanoparticles can be synthesized from a variety of distinct building blocks. These building blocks comprise metals in form of chalcogenides, nitrides, arsenide, oxides or elementary, as well as saccharides and non-fluorescent or fluorescent synthetic monomers, depending on the desired properties.[37,38]

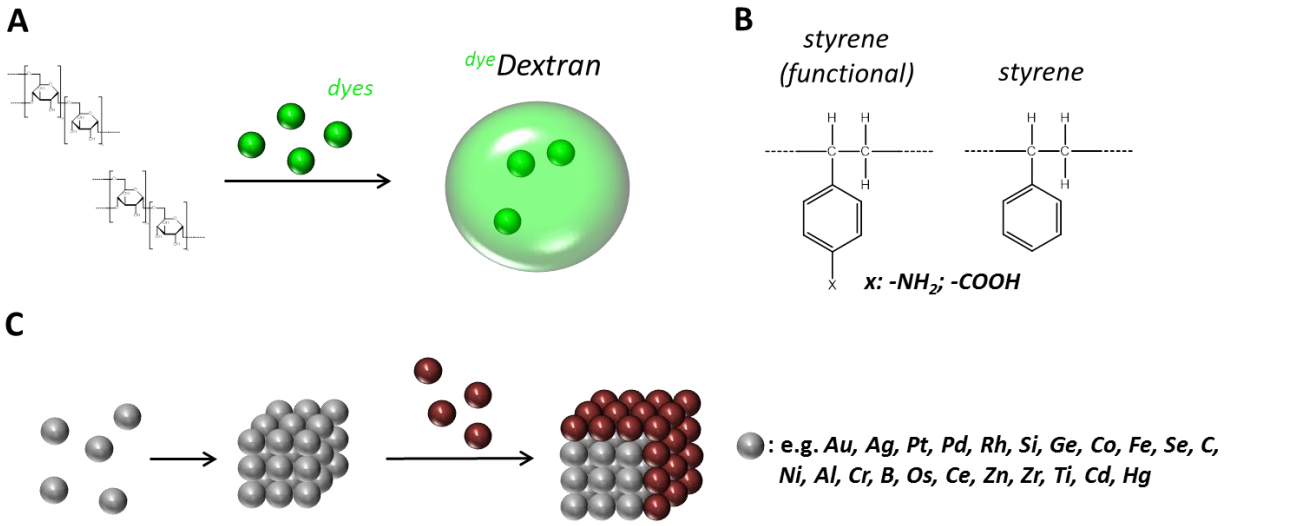

Figure I.2 Bottom-up synthesis of nanoparticles. (A) Scheme: Synthesis of dye doped Dextran nanoparticles. (B) Building blocks for the synthesis of functional polystyrene nanoparticles. (C) Scheme: Synthesis of inorganic nanoparticles.

For example, non-fluorescent monomers can be doped with organic fluorophores yielding fluorescent polymeric nanoparticles (Figure I.2 A).[39] In addition, chemical groups (e.g. -NH_2, -COOH etc.) can be introduced by co-polymerization using a functional building block of the same material (Figure I.2 B). These chemical groups facilitate further functionalization of nanoparticles with a variety of synthetic or biological compounds and contribute to an enhanced colloidal stability in water. Similar to polymeric nanoparticles, inorganic NPs can be synthesized with a second species for passivation or in order to obtain advanced or novel properties, respectively (Figure I.2 C).[40,41] The synthesis of many types of inorganic nanoparticles is a well-established field yielding NPs of high quality and with narrow size distribution.[42,43] These NPs are mostly synthesized in organic solvents at high temperatures which has several advantages.[44] (I) Temperature control of the nucleation kinetics allows growth of single NPs with better control of size and shape. (II) In the presence of steric a stabilizer (e.g. TOPO), much higher particle concentrations can be achieved than it is feasible in water. (III) Higher temperatures enable annealing out of impurities.

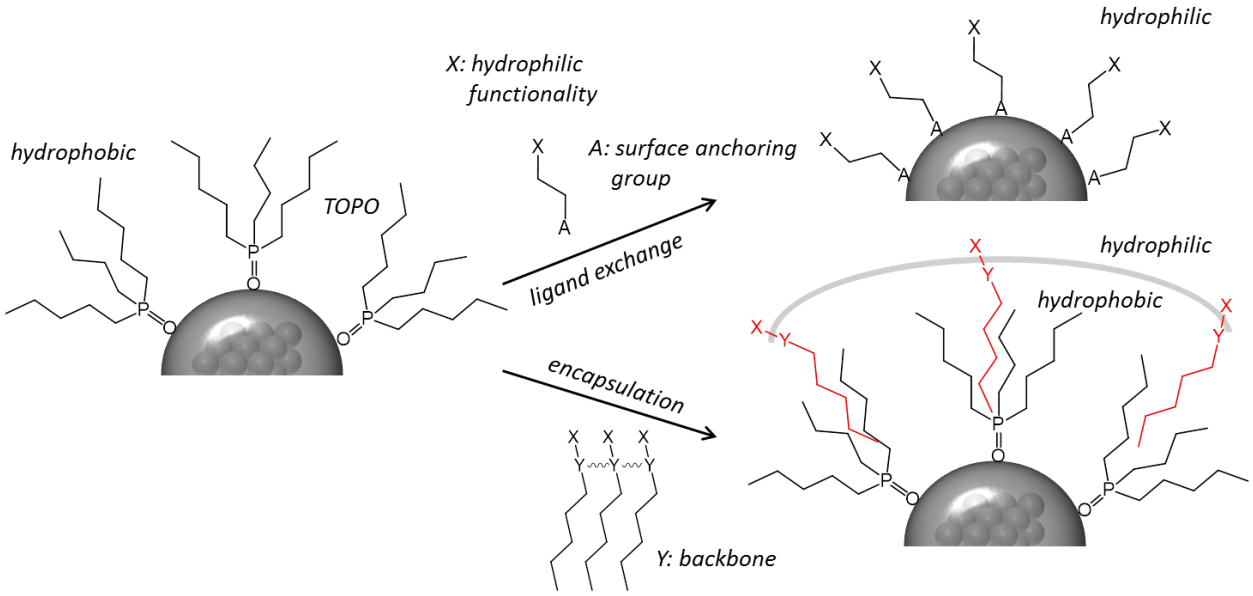

Figure I.3 Solubilization and coating of inorganic nanoparticles. Basic strategies utilized for solubilization of inorganic nanoparticles by ligand exchange or encapsulation.

The resulting NPs are hydrophobic and have to be solubilized for further application. For phase-transfer of hydrophobic nanoparticles into aqueous solution, two basic strategies can be employed (Figure I.3). First, the ligand exchange strategy which is based on the exchange of the steric

stabilizer for functional hydrophilic ligands.[45] On the other hand, nanoparticles can be encapsulated with heterofunctional organic polymers[46] or by polymerization of silica coats[47]. Since plenty of distinct ligands and polymers have been described,[48-51] the choice of the coating depends on the desired properties of the NPs like colloidal stability, bio-compatibility, size or further functionalization. In both strategies, the outer hydrophilic functionality mediates aqueous solubility and often simultaneously provides chemical groups for further functionalization.

2.2 Functionalization of nanoparticles

Specific application of nanoparticles requires functionalization with synthetic or biological compounds. This can be accomplished by a variety of distinct reactive groups on the surface of nanoparticles (Figure I.4 A), which can be employed either for non-covalent or covalent binding of molecules.

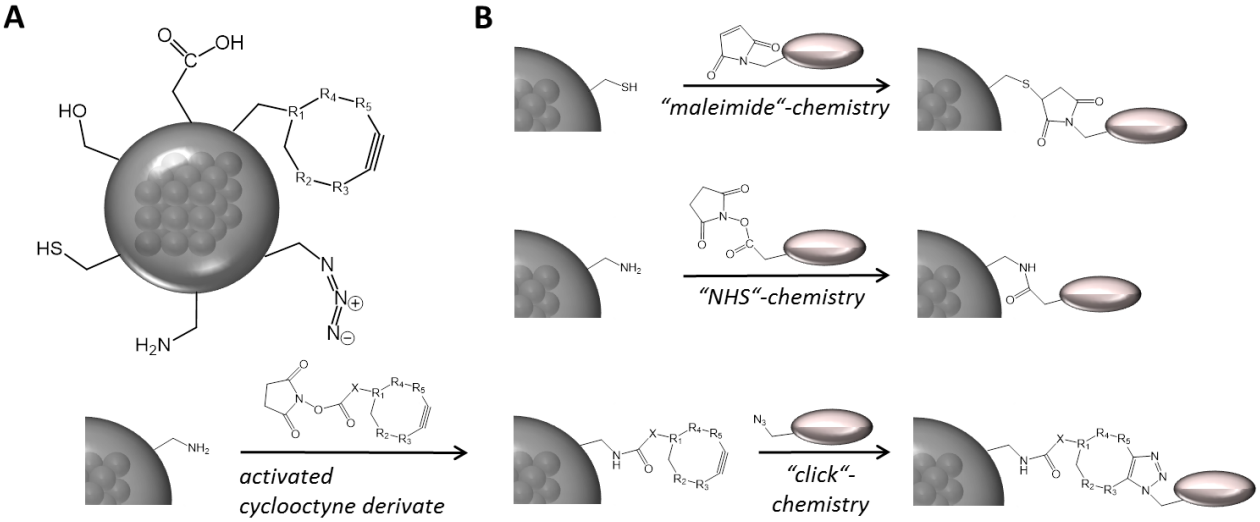

Figure I.4 Bioconjugation chemistries. (A) Nanoparticle surface posing distinct chemical functionalities, which can be employed for further conjugation. (B) Commonly used bioconjugation chemistries for the covalent modification of NP surfaces.

Non-covalent functionalization of NPs is mostly based on electrostatic interactions and yields nanoparticle conjugates with a number of drawbacks due to a low stability in biological fluids.[44] A more stable functionalization is obtained by covalent coupling of molecules to chemical groups on the NP surface. The stability of covalent NP conjugates is mostly only limited by the stability of the NPs itself or by the stability of the conjugated molecules.

A multitude of chemical reactions suitable for covalent surface functionalization of NPs have been described.[52] Often, nanoparticles present amine-, thiol- or carboxyl-groups on the surface. These chemical functionalities allow well established bioconjugation chemistries that can be performed under mild conditions in buffered aqueous solutions within a pH range of 5 – 9 (Figure I.4 B). Coupling to thiols can be achieved utilizing maleimide chemistry yielding stable thioether bonds. NHS-chemistry is exploited for coupling of activated carboxyl groups to amines yielding stable amide bounds. Alternatively, existing chemical groups can be converted to other functionalities. For instance, a NHS activated cyclooctyne derivative can be coupled to amines yielding a chemical functionality that facilitates click-chemistry.[53] The capabilities of biologically chemical functionalities, i.e. -SH, $-NH_2$ and -COOH are sufficient to solve almost any conceivable nanoparticle modification or conjugation challenge *in vitro* either by direct coupling or by converting to other chemical functionalities.[52] However, possible issues of nanoparticle surface modification that must be taken into account are altered physicochemical properties affecting e.g. the colloidal stability, as well as an altered biological recognition.

2.3 Physicochemical properties of nanoparticles

The physicochemical properties of nanoparticles contribute to the fact that NPs behave as colloids. A special case of colloids is represented by proteins that can be ascribed to their heterogeneous structures.[54] Proteins are amphoteric polyelectrolytes and simultaneously possess hydrophobic and hydrophilic patches. The distribution of charges, as well as hydrophobic and hydrophilic patches on nanoparticle surfaces on the other hand can be assumed to be more homogeneous. Nanoparticle with densities lower or similar to that of the continuous phase are not significantly affected by gravitational forces and inertia.[55] Thus, gravitational settling is negligible. The main characteristic to identify colloidal behavior is based on the ability of *Brownian* motion of the particles. This is caused by fluctuating momentum transfer from the solvent to the dispersed particles.

One challenge in the application of nanoparticles is based on their large surface areas per total volume, which can facilitate strong intermolecular interactions. These interactions between nanoparticles in aqueous solution are mainly determined by electric double layer forces (electrostatic), van der Waals forces, as well as short range depletion forces, hydration forces and

hydrophobic forces. Electrostatic interaction arises when particles are dissolved in water. The charging of the surface can be ascribed to two charging mechanism: (I) by the ionization or dissociation of surface groups or (II) by the adsorption of ions from solution onto the previously uncharged surface.[56]

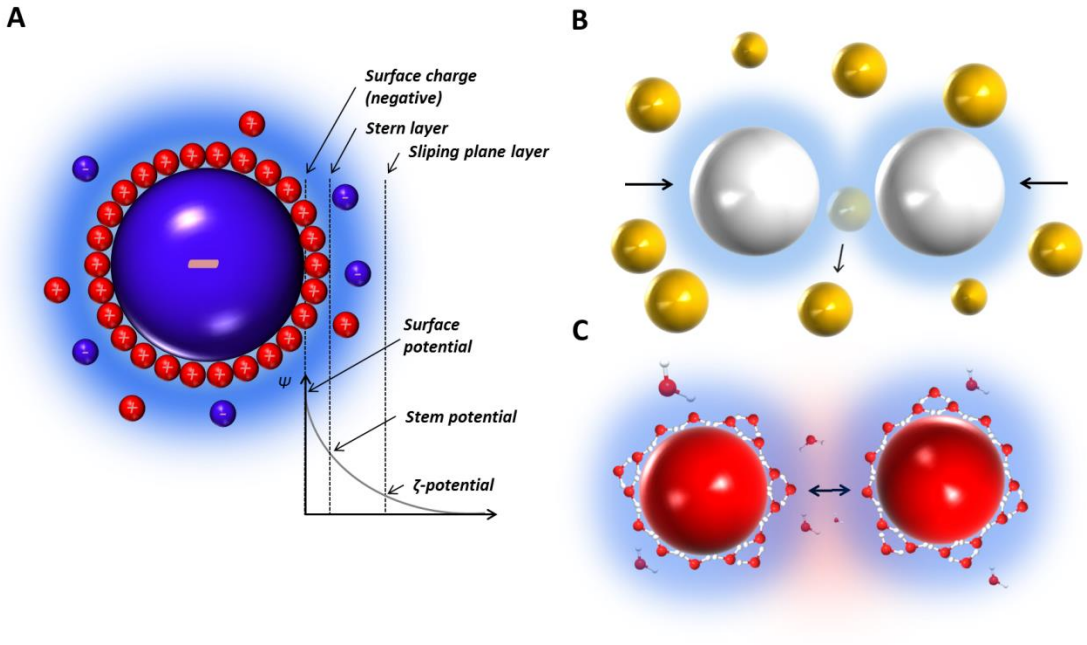

Figure I.5 Interaction forces of nanoparticles. (A) Schematic illustration: Formation of an electric double layer around a negatively charged colloid. (B) Attractive depletion forces arise in a dilute solution of smaller depletants. (C) Repulsive hydration forces depend on the affinity of the particles to bind water.

For example, when spherical nanoparticles exhibiting acidic groups on their surface are dispersed in water, the surface acquires a net charge due to the dissociation of protons (Figure I.5 A). The dissociated protons in combination with ions of dissociated water at room temperature form an electric double layer (EDL) around the particles. A first layer called “Stern layer” is formed by strong adsorption of cations onto the negatively charged particle surface. The second layer on top is composed of less firmly associated co- and counterions. The boundary of this diffusive layer is termed “slipping plane”, within which the particles act as single entity. The electric potential at the slipping plane is the zeta potential (ζ-potential) or the overall charge that a particle acquires in a specific medium. Electric double layer forces are repulsive between particles of the same type and the magnitude depends on the number of charged surface groups. By contrast, van der Waals forces (VDW) are omnipresent and are attractive between the same particles in water.[57] The VDW

forces originate from interactions of dipoles in the molecules of two opposing nanoparticles and can be regarded as the sum of three distinct types of force contributions: (I) Orientation forces between two permanent dipoles; (II) Induction forces between a permanent dipole and a corresponding induced dipole and (III) London dispersion forces between instantaneously induced dipoles (usually referred to as VDW). The total force acting between the nanoparticles dispersed in water can reach several nanometers across the intervening medium.[56] Furthermore, depletion forces arise when colloids are dispersed in a dilute solution of smaller depletants (Figure I.5 B).[58] Depletants can be small molecules or macromolecules. When the distance of two particles is below the diameter of the depletant, the depletant is excluded. The resulting osmotic imbalance causes an attractive force. Depletion forces are entropic in origin and the range is directly related to the radius of gyration, whereas the strength is proportional to osmotic pressure of the depletant. An additional repulsive force is based on the formation of an extensive protective layer of structured water around the particles (Figure I.5 C).[59] The strength and range of hydration forces depends on the affinity of the particles to bind water molecules and thereby, on the physicochemical properties, i.e. hydrophilicity of the particles, as well as on the structure of water. The structure of water in turn is determined by the presence or absence of a "structure breaker" such as chaotropic salts. By contrast, attraction will occur when the affinity of two interacting particle surfaces to bind water is much lower than the affinity between the water molecules themselves, the so-called "hydrophobic effect".

2.4 Stabilization of nanoparticles in aqueous solution

The stability of a nanoparticle dispersion in water is defined as the capability of the dispersion to remain as it is. For example, nanoparticles exhibiting hydrophobic and non-charged surfaces are referred to as metastable. These particles coagulate over time due to the large surface energies which cause strong intermolecular attractive forces. Thus, colloidal stability of a particle suspension in water must be mediated. These can be facilitated by steric or electrostatic stabilization. A combination of the two mechanism (electrosteric) is also possible. Steric stabilization is based on grafting particle surfaces with polymeric chains which creates repulsive forces (Figure I.6 A).[60] For example, frequently used polymers are based on poly(ethylene glycol) (PEG).[61,62] The repulsion arises from steric effects based on the reduction of freedom of the grafted

chains. Steric stabilization is a thermodynamic process due to the decrease of entropy when two polymer coated particles approach each other. These repulsive entropic forces cause an increase of free energy of the system.

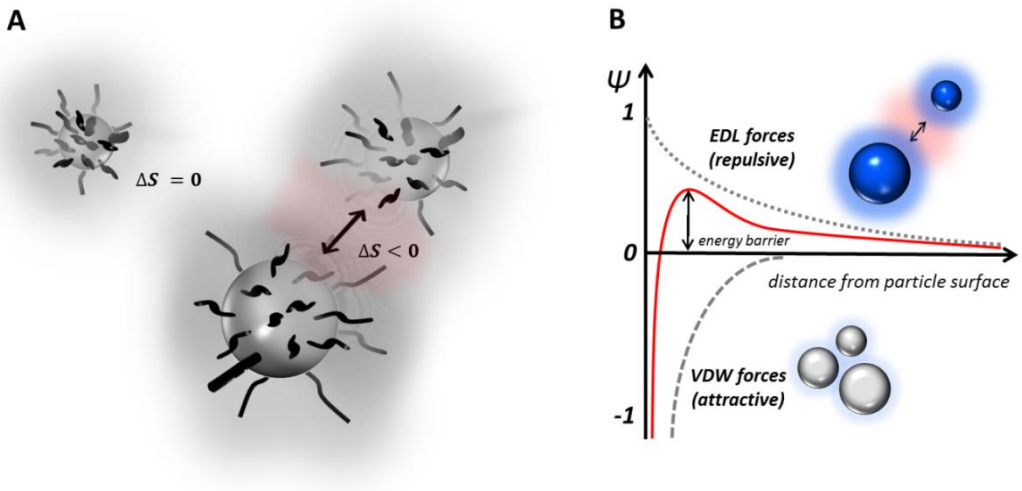

Figure I.6 Stabilization of nanoparticles. (A) Steric stabilization of metastable colloids by grafting with polymers. Stabilization occurs through entropic repulsion. (B) Illustration of the DLVO theory: Interaction potentials between charged particles in water. Adapted and modified from Deryaguin et al. 1941 and Verwey et al. 1948.[63,64]

The entropic potential that arises from the polymeric graft depends on the chain length, chain density and on the chemical properties of the chain itself.[65] In addition, attachment of charged groups on the surface also creates a repulsive interaction. For reasons of simplification, one can assume two major long range forces acting between two charged nanoparticles in water.[66] These forces are attractive van der Waals (VDW) and repulsive electric double layer forces. The combined effect of EDL repulsion and VDW attraction between two particles is described by the DLVO theory.[63,64] This theory is built on the assumption that the forces between two particle surfaces are additive. This means that the stability of charged particles in water is given as long as EDL are the dominating forces. As shown in Figure I.6 B, by overcoming the energy barrier either by lowering the separation of the particles or by reducing the surface charge, electrostatic repulsion turns into VDW attraction and consequently in loss of stability.

2.5 The nanoparticle protein-corona

When nanoparticles enter biological fluids the situation becomes substantially more complicated, since the particles are exposed to a plethora of different ions, molecules and macromolecules (biomolecules). First of all, intermolecular interactions between nanoparticles and biomolecules are underlying the same principles as described above for the interaction between nanoparticles in water.[67] Under physiological ionic strength, electrostatic interactions are restricted and usually occur only a few nanometers above the nanoparticle surface. Interactions of permanent dipoles are restricted as well. Whereas, London dispersion forces, depletion forces, hydrophobic forces and hydration forces remain still operative. These interactions can vary significantly due to the specific physicochemical properties of nanoparticles and in presence of biomolecules.[67-69] For instance, nanoparticle aggregation in water, i.e. the stability, only results from the sum of all intermolecular interactions between the nanoparticles themselves. By contrast, in biological fluids the intermolecular interactions between nanoparticles and biomolecules can modify the nanoparticle surface by forming a biomolecular layer around the particles. This biomolecular layer has been shown to be governed by proteins.[70-73] Thus, the surface properties and biological identity of the newly formed nanoparticle-protein hybrid will also be determined by the adsorbed proteins.[74,75] The composition of the associated proteins within a “protein-corona” have been demonstrated to be determined by the physicochemical properties of the NPs such as size, shape, chemical composition and physicochemical surface characteristics, as well as the abundance and the kinetic properties of the proteins within the biological fluid.[67,69,76,77] Furthermore, it has been shown that the formation of the protein-corona is a dynamic process of continuous adsorption and desorption events (Figure I.7 A).[78] The first layer of the formed protein-corona consists of proteins of high abundance and of proteins with high affinities towards the NPs. Over time, loosely bound proteins are replaced with proteins exhibiting lower dissociation rates, which form the protein “hard-corona”. The proteins of the hard-corona can further interact with free proteins forming the protein “soft-corona”. For example, the association of the hard-corona on distinct nanomaterials has been found to occur fast in serum, while the soft-corona is formed much slower.[72,79] Dissociation in turn has been found to occur fast for proteins of the soft-corona, whereas the hard-corona is more stable.

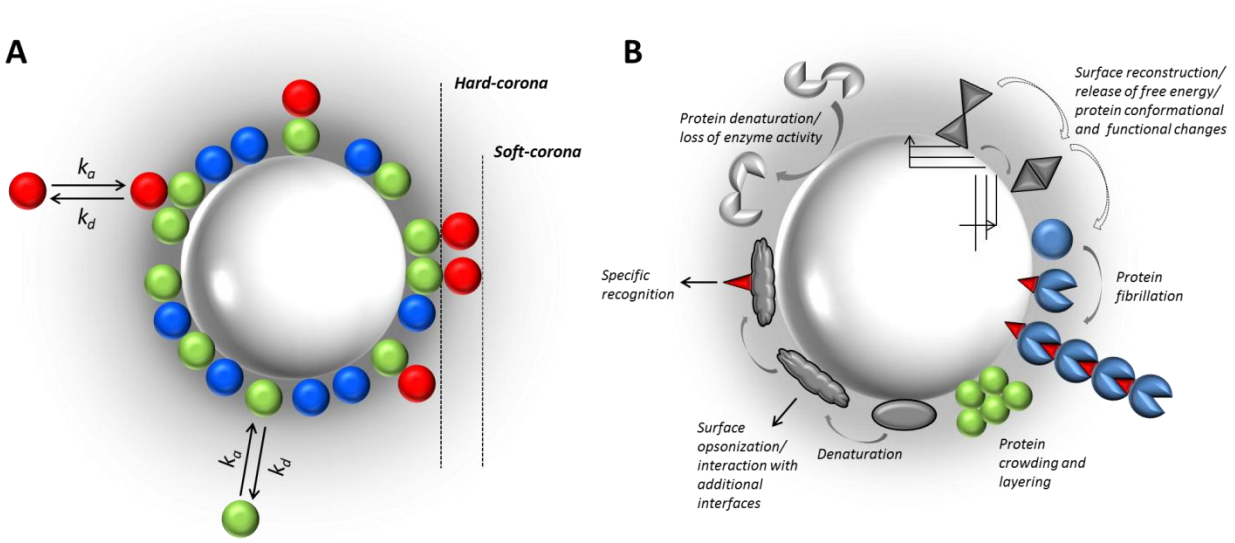

Figure I.7 The protein-corona of nanoparticles in biological fluids. (A) Schematic illustration: Model of the protein-corona formed on the nanoparticle surface in biological fluids. Adapted and modified from Walkey et al. 2012.[78] (B) Schematic illustration: Effects on protein structure and function as a result of protein adsorption on nanoparticle surfaces. Adapted and modified from Nel et al. 2009.[69]

Thus, the biological identity of NPs that is screened continuously alters over time due to the exchange of proteins in different enviroments. These changes in the composition of the protein-corona are referred to as the "Vroman Effect".[80] Depending on the biological environment and the proteins which are involved, the formation and the evolution of the protein-corona may have a significant effect on the physiological response to a nanomaterial.[78,81]

Vice versa, the effects of nanoparticles on protein structure and function can be diverse as well (Figure I.7 B). For example, nanoparticle surface reconstruction has been observed upon protein binding to zinc sulfur particles.[82] It is thought that contact forces such as the release of free energy upon protein binding and surface reconstruction is involved in protein denaturation. It has also been shown that co-polymer particles, cerium oxide particles, quantum dots and carbon nanotubes enhance the probability of $ß_2$-microglobulin fibrillation in a size and surface chemistry dependent manner.[83] In addition, a nanoparticle size-dependent loss of enzyme activity has been shown for chicken egg lysozyme bound to silica nanoparticles.[84]

2.6 Unspecific interactions of fluorescent nanoparticles inside living cells

As described above, in biological fluids the identity and fate of nanoparticles is determined by intermolecular interactions with biomolecules. In the cytoplasm of living cells, the diverse fates of nanoparticles exhibiting different sizes, ζ-potentials and surface chemistries are shown in Figure I.8.

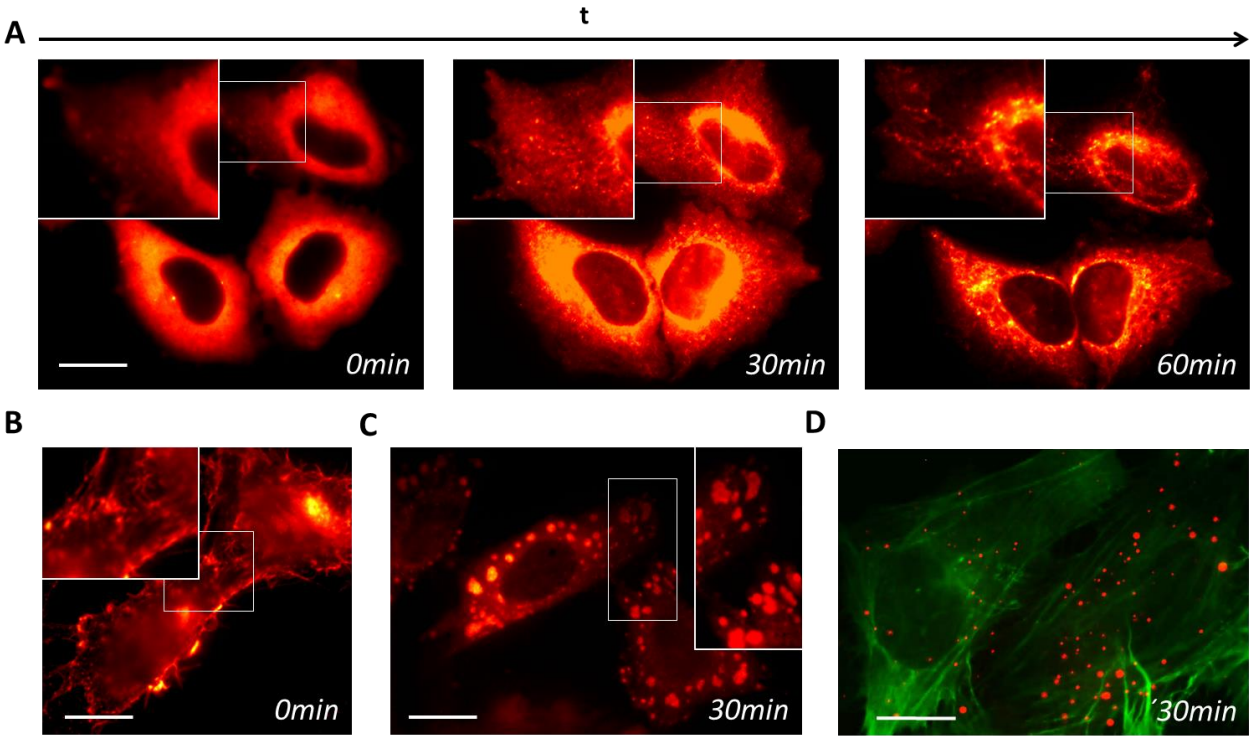

Figure I.8 Unwanted interactions of nanoparticles with intracellular compounds or compartments according to their physicochemical properties. Microinjection of (A) 250 nM Streptavidin coated QDs; (B) 100 nM Silica NPs (ζ: +20 mV); (C) 100 nM Silica NPs (ζ: -5 mV) and (D) 250 nM PEGylated Silica NPs into HeLa cells. In figure (D) actin was stained by Lifeact::mEGFP. Scale bar corresponds to 5 µm in all images.

Upon microinjection, streptavidin coated quantum dots (Invitrogen, ~16 nm in diameter, ζ: -1 mV) are freely diffusing in the cytoplasm. However, unspecific interaction with intracellular structures can be observed 30 minutes upon microinjection (Figure I.8 A). Silica nanoparticles (~40 nm in diameter, ζ: +20 mV) are predominantly localized at the plasma membrane immediately after microinjection (Figure I.8 B). By contrast, when the surface exposed amines are partially converted to carboxyl groups (ζ: -5 mV), the particles seems to be localized in cellular compartments 30 minutes after microinjection (Figure I.8 C). PEGylated silica nanoparticles (~ 12 nm in diameter)

form clusters in the cytoplasm (Figure I.8 D). Also, aggregation and clustering of quantum dots exhibiting different surface chemistries have recently been observed inside living cells.[85,86]

2.7 Diffusion properties of nanoparticles inside living cells

Inside living cells, the diffusion of molecules and macromolecules is determined (I) by the properties of the cytoplasm such as fluid-phase viscosity and solute concentration; (II) by the physicochemical properties of the solutes, i.e. the size and intermolecular interactions and (III) by the characteristics of the cell including composition, organization and geometry of cellular compartments.[87,88] When intermolecular interactions are negligible, as it is the case for GFP (green fluorescent protein),[89] and fluorescein labeled dextrans (FITC-dextrans; MW <500 kDa equivalent to a radius of gyration (R_G) <30 nm),[90] diffusion has been shown to be 4-5 fold lower in the cytoplasm compared to diffusion in water (D_{cyto}/D_{water} ~ 0.25-0.2) (Figure I.9 A). The decelerated diffusion could predominantly be ascribed to molecule collisions (molecular crowding), as well as to a slightly increased fluid-phase viscosity of the cytoplasm compared to that of water.[91,92]

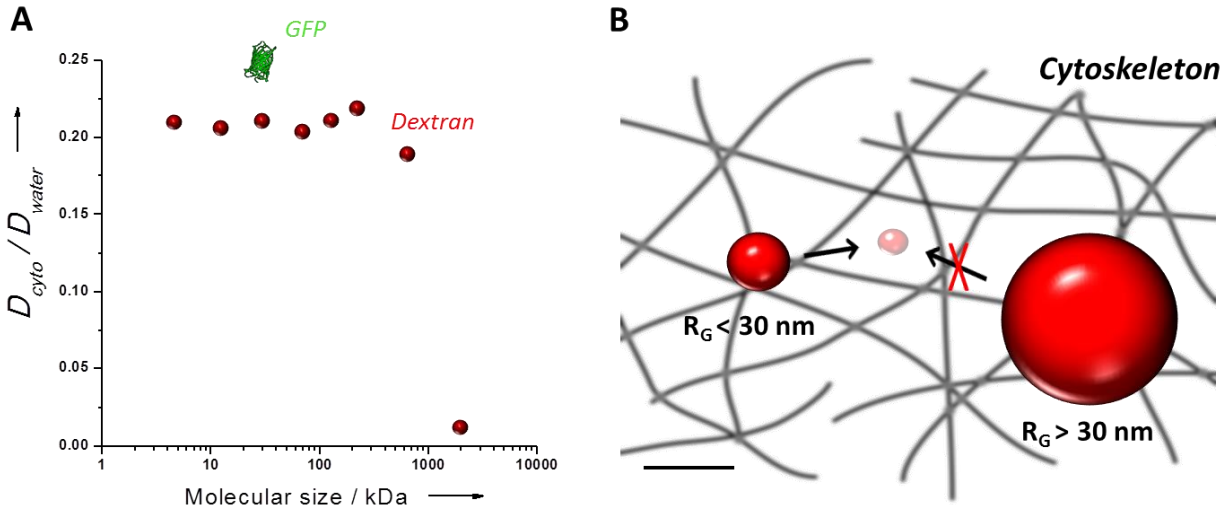

Figure I.9 Diffusion of molecules and macromolecules inside living cells. (A) Diffusion coefficients for indicated molecules/macromolecules in the cytoplasm normalized to the diffusion coefficients in water. Adapted and modified from Verkman 2002.[88] (B) Schematic Illustration: While non-interacting macromolecules (R_G <30 nm) can freely diffuse in the cytoplasm, larger molecules (R_G >30 nm) seem to be entrapped in cellular compartments. The scale bar corresponds to 60 nm.

By contrast, diffusion of higher molecular weight FITC-dextrans (MW >500 kDa) was biased.[90] A similar behavior has been observed for FITC-ficolls of comparable size.[93] This molecular size

dependent threshold was attributed to a network of obstructions, most likely the cytoskeleton (Figure I.9 B).[87] Thus, unbiased intracellular diffusion of nanoparticles (R_G <30 nm) can be achieved if intermolecular interactions are negligible.

3 Aims and strategies of the PhD thesis

Nanoparticles provide great potential for investigating intracellular processes down to the level of individual machineries. NPs with advanced optical and magnetical properties have been employed for probing and manipulation of cell surface proteins. The unbiased application of nanoparticles inside living cells, however, requires overcoming non-specific interactions with a plethora of biomolecules and metabolic machineries. To this end, this thesis aimed to provide nanoparticle surface functionalization for unbiased and specific application of nanoparticles in the cytoplasm of living cells. This goal was approached from two directions. First, a nanoparticle targeting strategy was developed for site-specific and rapid targeting of nanoparticles to proteins. This was achieved by systematic engineering of the HaloTag technology. Second, nanoparticle surfaces were systematically engineered in order to obtain “stealth” nanoparticles, as well as to ensure labeling of intracellular proteins in a 1:1 stoichiometry. Finally, the know-how and technology in terms of intracellular NP functionalization were exploited to develop a novel technique that we referred to as magnetogenetics. In this technique 500 nm superparamagnetic nanoparticles were utilized as self-assembled and displaceable signaling platforms.

3.1 Site-specific targeting of nanoparticles to proteins inside living cells.

The HaloTag technology has been developed as a versatile tag, especially for specific labeling proteins in living cells.[94,95] This technology consists of the HaloTag protein and the HaloTag ligand (HTL). The HaloTag protein is an engineered *Rhodococcus* dehalogenase (DhaA, Figure I.10 A) and was designed to covalently bind to synthetic ligands. The covalent bond formation in the active center of the enzyme is illustrated in Figure I.10 B. The enzyme can be fused either to the N-terminus or to the C-terminus of the protein of interest. HaloTag ligands comprise a chloroalkane chain, ethylene glycol units as spacer and a chemical functionality (-NH_2, -SH_2 or –COOH) (Figure I.10 C). These chemical functionalities facilitate the coupling of the HTL to a variety of molecules such as organic dyes, affinity handles, solid surfaces and the surface of nanoparticles.

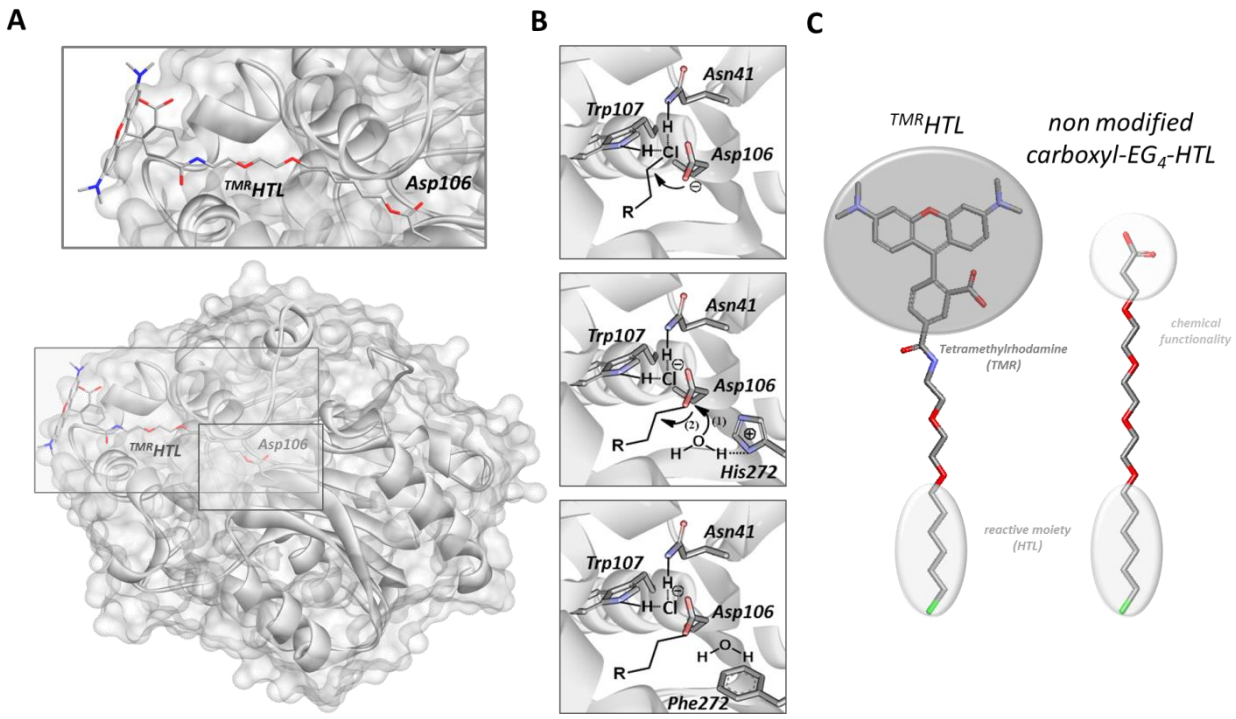

Figure I.10 The HaloTag system. (A) HaloTag protein model with HTL conjugated to TMR inside the binding pocket. The active center is highlighted by the rectangle. (B) Reaction mechanism of wild type DhaA and mutant dehalogenase (HaloTag). (top) Nucleophilic attack by Asp106 leads to the displacement of the terminal chloride and to the formation of a covalent alkyl-(ester)-enzyme intermediate. (middle) In the wild type enzyme (DhaA), the presence of a base, mediated by His272, causes the hydrolysis of the ester bond and the release of the product. (bottom) In the HaloTag protein, Phe was substituted for His, which is inactive as potential base and traps the reaction intermediate as covalent adduct. (C) (left) Tetramethylrhodamine conjugated to the HTL; (right) non-modified carboxyl-HTL facilitates coupling to amine presenting compounds. Adapted and modified from Los et al.[95]

3.2 Manipulation of protein activities

Magnetogenetic means genetically encoded targeting of specific proteins in combination with magnetic nano-manipulation (Figure I.11 A).

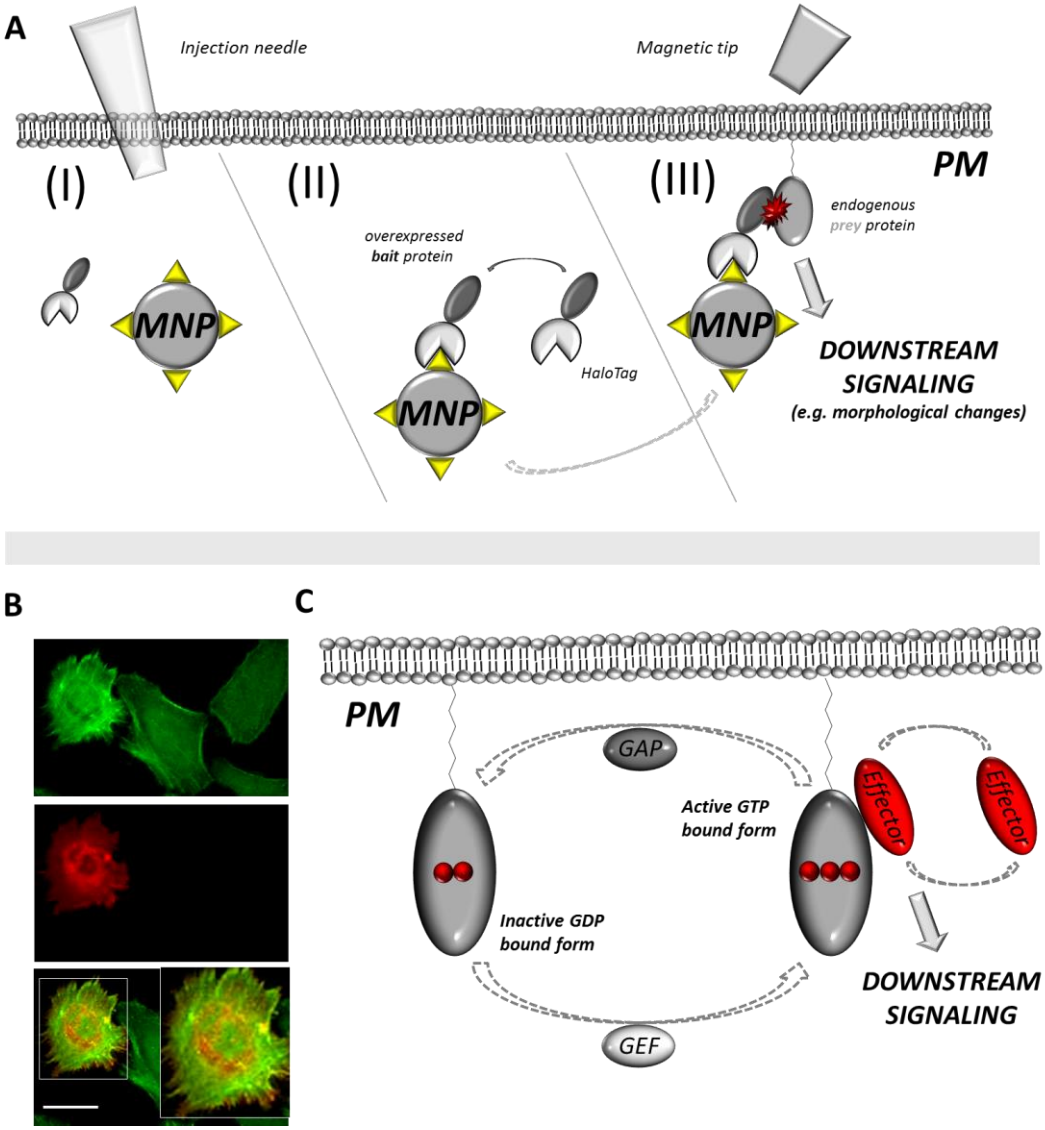

Figure I.11 Schematic illustration of magnetogenetics and regulation of small Rho GTPases. (A) Microinjection of functionalized MNPs (I) allows the self-assembly of an active signaling platform on the surface of MNPs (II). Application of a magnetic field by using a small magnetic-tip facilitates to specifically displace bfMNPs to any region of the cell (III). In this approach, the signaling platform is thought to propagate a signal to cellular functions by locally activating a pool of endogenous proteins. (B) HeLa cells co-expressing constitutively active cdc42^{Q61L} fused to mCherry and Lifeact:meGFP (green: Lifeact::mEGFP; red: mCherry::cdc42^{Q61L}; yellow: merge). The scale bar corresponds to 10 µm. (C) Regulation of small Rho GTPases. Adapted and modified from Heasman et al. 2008.[96]

The general strategy is that upon microinjection of MNPs (I), site-specific bio-functionalization of these particles with a protein takes place in the cytoplasm of living cells (II). Subsequently, controlled spatial displacement of bio-functionalized MNPs (bfMNPs) by applying magnetic forces allows propagating a functional signal, carried by the immobilized protein, specifically, to cellular functions (III). Small GTPases of the Rho family were employed as model proteins, since their activation causes strong morphological changes (Figure I.11 B).[97] These morphological changes can be observed by remodeling of the actin-cytoskeleton, which can be monitored by using a fluorescent reporter. Small GTPases of the Rho family act as molecular switches and cycle between a GDP-bound inactive state and a GTP-bound active state (Figure I.11 C).[98] The binding to a guanine nucleotide-exchange factor (GEF) stimulates the exchange of GDP for GTP. Upon activation, the binding of effector proteins mediates the propagation of downstream signaling. The intrinsic GTPase activity is enhanced after binding to a GTPase-activating protein (GAP), resulting in an inactive GDP-bound GTPase.

4 References

1. Feynman, R.P. There's plenty of room at the bottom. *Eng. Sci.* **23**, 22-36 (1960).
2. Taniguchi, N. On the Basic Concept of 'Nano-Technology. *Proc. Intl. Conf. Prod. Eng. Tokyo, Part II, Japan Society of Precision Engineering* (1974).
3. Behari, J. Principles of nanoscience: an overview. *Indian J Exp Biol* **48**, 1008-19 (2010).
4. Rodgers, P. Nanoelectronics: Single file. *Nat Nano*, 1748-3387 (2006).
5. Initiative, N.N. What is Nanotechnology.
6. Hodes, G. When Small Is Different: Some Recent Advances in Concepts and Applications of Nanoscale Phenomena. *Advanced Materials* **19**, 639-655 (2007).
7. Smith, A.M. & Nie, S. Semiconductor Nanocrystals: Structure, Properties, and Band Gap Engineering. *Accounts of Chemical Research* **43**, 190-200 (2009).
8. Louizos, L.A., Athanasopoulos, P.G. & Varty, K. Microelectromechanical systems and nanotechnology: a platform for the next stent technological era. *Vasc Endovascular Surg* **46**, 605-9 (2012).
9. Tinazli, A., Piehler, J., Beuttler, M., Guckenberger, R. & Tampe, R. Native protein nanolithography that can write, read and erase. *Nat Nanotechnol* **2**, 220-5 (2007).
10. Zhang, L. et al. Nanoparticles in medicine: therapeutic applications and developments. *Clin Pharmacol Ther* **83**, 761-9 (2008).
11. Drummen, G.P. Quantum dots-from synthesis to applications in biomedicine and life sciences. *Int J Mol Sci* **11**, 154-63 (2010).
12. Medintz, I.L., Uyeda, H.T., Goldman, E.R. & Mattoussi, H. Quantum dot bioconjugates for imaging, labelling and sensing. *Nat Mater* **4**, 435-46 (2005).
13. Lee, S., Lee, K.H., Ha, J.S., Lee, S.G. & Kim, T.K. Small-molecule-based nanoassemblies as inducible nanoprobes for monitoring dynamic molecular interactions inside live cells. *Angew Chem Int Ed Engl* **50**, 8709-13 (2011).
14. Kim, S.E. et al. Fluorescent ferritin nanoparticles and application to the aptamer sensor. *Anal Chem* **83**, 5834-43 (2011).
15. Lee, J.H. et al. Artificial control of cell signaling and growth by magnetic nanoparticles. *Angew Chem Int Ed Engl* **49**, 5698-702 (2010).
16. Srikun, D., Albers, A.E., Nam, C.I., Iavarone, A.T. & Chang, C.J. Organelle-Targetable Fluorescent Probes for Imaging Hydrogen Peroxide in Living Cells via SNAP-Tag Protein Labeling. *Journal of the American Chemical Society* **132**, 4455-4465 (2010).
17. Van de Bittner, G.C., Dubikovskaya, E.A., Bertozzi, C.R. & Chang, C.J. In vivo imaging of hydrogen peroxide production in a murine tumor model with a chemoselective bioluminescent reporter. *Proc Natl Acad Sci U S A* **107**, 21316-21 (2010).
18. Xu, J. et al. Labeling Cytosolic Targets in Live Cells with Blinking Probes. *J Phys Chem Lett* **4**, 2138-2146 (2013).

19. Huang, H., Delikanli, S., Zeng, H., Ferkey, D.M. & Pralle, A. Remote control of ion channels and neurons through magnetic-field heating of nanoparticles. *Nat Nanotechnol* **5**, 602-6 (2010).

20. Smith, A.M., Mohs, A.M. & Nie, S. Tuning the optical and electronic properties of colloidal nanocrystals by lattice strain. *Nat Nanotechnol* **4**, 56-63 (2009).

21. Mahajan, K.D., Fan, Q., Dorcéna, J., Ruan, G. & Winter, J.O. Magnetic quantum dots in biotechnology – synthesis and applications. *Biotechnology Journal*, n/a-n/a (2013).

22. Pelaz, B. et al. The state of nanoparticle-based nanoscience and biotechnology: progress, promises, and challenges. *ACS Nano* **6**, 8468-83 (2012).

23. Michalet, X. et al. Quantum Dots for Live Cells, in Vivo Imaging, and Diagnostics. *Science* **307**, 538-544 (2005).

24. Liu, D.S., Phipps, W.S., Loh, K.H., Howarth, M. & Ting, A.Y. Quantum dot targeting with lipoic acid ligase and HaloTag for single-molecule imaging on living cells. *ACS Nano* **6**, 11080-7 (2012).

25. You, C. et al. Electrostatically controlled quantum dot monofunctionalization for interrogating the dynamics of protein complexes in living cells. *ACS Chem Biol* **8**, 320-6 (2013).

26. Clarke, S. et al. Covalent monofunctionalization of peptide-coated quantum dots for single-molecule assays. *Nano Lett* **10**, 2147-54 (2010).

27. Shin, J., Zhang, X. & Liu, J. DNA-functionalized gold nanoparticles in macromolecularly crowded polymer solutions. *J Phys Chem B* **116**, 13396-402 (2012).

28. Ilyas, S., Ilyas, M., van der Hoorn, R.A. & Mathur, S. Selective Conjugation of Proteins by Mining Active Proteomes through Click-Functionalized Magnetic Nanoparticles. *ACS Nano* (2013).

29. Resch-Genger, U., Grabolle, M., Cavaliere-Jaricot, S., Nitschke, R. & Nann, T. Quantum dots versus organic dyes as fluorescent labels. *Nat Methods* **5**, 763-75 (2008).

30. Jaiswal, J.K., Mattoussi, H., Mauro, J.M. & Simon, S.M. Long-term multiple color imaging of live cells using quantum dot bioconjugates. *Nat Biotechnol* **21**, 47-51 (2003).

31. Pinaud, F., Clarke, S., Sittner, A. & Dahan, M. Probing cellular events, one quantum dot at a time. *Nat Methods* **7**, 275-85 (2010).

32. De, M., Ghosh, P.S. & Rotello, V.M. Applications of Nanoparticles in Biology. *Advanced Materials* **20**, 4225-4241 (2008).

33. Gref, R. et al. 'Stealth' corona-core nanoparticles surface modified by polyethylene glycol (PEG): influences of the corona (PEG chain length and surface density) and of the core composition on phagocytic uptake and plasma protein adsorption. *Colloids Surf B Biointerfaces* **18**, 301-313 (2000).

34. Kramer, R.M., Li, C., Carter, D.C., Stone, M.O. & Naik, R.R. Engineered Protein Cages for Nanomaterial Synthesis. *Journal of the American Chemical Society* **126**, 13282-13286 (2004).

35. Allen, M., Willits, D., Young, M. & Douglas, T. Constrained synthesis of cobalt oxide nanomaterials in the 12-subunit protein cage from Listeria innocua. *Inorg Chem* **42**, 6300-5 (2003).

36. Li, F. et al. Monofunctionalization of protein nanocages. *J Am Chem Soc* **133**, 20040-3 (2011).

37. Glotzer, S.C., Solomon, M.J. & Kotov, N.A. Self-assembly: From nanoscale to microscale colloids. *AIChE Journal* **50**, 2978-2985 (2004).

38. Wu, C. & Chiu, D.T. Highly fluorescent semiconducting polymer dots for biology and medicine. *Angew Chem Int Ed Engl* **52**, 3086-109 (2013).

39. Holzapfel, V., Musyanovych, A., Landfester, K., Lorenz, M.R. & Mailänder, V. Preparation of Fluorescent Carboxyl and Amino Functionalized Polystyrene Particles by Miniemulsion Polymerization as Markers for Cells. *Macromolecular Chemistry and Physics* **206**, 2440-2449 (2005).

40. Haase, M. & Schafer, H. Upconverting nanoparticles. *Angew Chem Int Ed Engl* **50**, 5808-29 (2011).

41. Xie, W., Herrmann, C., Kompe, K., Haase, M. & Schlucker, S. Synthesis of bifunctional Au/Pt/Au Core/shell nanoraspberries for in situ SERS monitoring of platinum-catalyzed reactions. *J Am Chem Soc* **133**, 19302-5 (2011).

42. Pelaz, B. et al. The State of Nanoparticle-Based Nanoscience and Biotechnology: Progress, Promises, and Challenges. *ACS Nano* **6**, 8468-8483 (2012).

43. Zubarev, E.R. Nanoparticle synthesis: any way you want it. *Nat Nanotechnol* **8**, 396-7 (2013).

44. Zhang, F. et al. Polymer-coated nanoparticles: a universal tool for biolabelling experiments. *Small* **7**, 3113-27 (2011).

45. Mattoussi, H. et al. Self-Assembly of CdSe−ZnS Quantum Dot Bioconjugates Using an Engineered Recombinant Protein. *Journal of the American Chemical Society* **122**, 12142-12150 (2000).

46. Dubertret, B. et al. In Vivo Imaging of Quantum Dots Encapsulated in Phospholipid Micelles. *Science* **298**, 1759-1762 (2002).

47. Kim, S. & Bawendi, M.G. Oligomeric Ligands for Luminescent and Stable Nanocrystal Quantum Dots. *Journal of the American Chemical Society* **125**, 14652-14653 (2003).

48. Jiang, W., Mardyani, S., Fischer, H. & Chan, W.C.W. Design and Characterization of Lysine Cross-Linked Mercapto-Acid Biocompatible Quantum Dots. *Chemistry of Materials* **18**, 872-878 (2006).

49. Mitchell, G.P., Mirkin, C.A. & Letsinger, R.L. Programmed Assembly of DNA Functionalized Quantum Dots. *Journal of the American Chemical Society* **121**, 8122-8123 (1999).

50. Prakash, A. et al. Bilayers as Phase Transfer Agents for Nanocrystals Prepared in Nonpolar Solvents. *ACS Nano* **3**, 2139-2146 (2009).

51. Wu, X. et al. Immunofluorescent labeling of cancer marker Her2 and other cellular targets with semiconductor quantum dots. *Nat Biotechnol* **21**, 41-6 (2003).

52. Hermanson, G.T. Bioconjuagte Tequniues **Second Edition**.

53. Jewett, J.C. & Bertozzi, C.R. Cu-free click cycloaddition reactions in chemical biology. *Chem Soc Rev* **39**, 1272-9 (2010).

54. Piazza, R. Protein interactions and association: an open challenge for colloid science. *Current Opinion in Colloid & Interface Science* **8**, 515-522 (2004).

55. Lyklema, J. Fundamentals of Interface and Colloid Science. Volume I: Fundamentals. *Academic Press* (1991).

56. Israelachvili, J.N. Intermolecular and Surface Forces, 2nd ed. *Academic Press: New York* (1998).

57. Liang, Y., Hilal, N., Langston, P. & Starov, V. Interaction forces between colloidal particles in liquid: Theory and experiment. *Advances in Colloid and Interface Science* **134–135**, 151-166 (2007).

58. Mao, Y., Cates, M.E. & Lekkerkerker, H.N.W. Depletion force in colloidal systems. *Physica A: Statistical Mechanics and its Applications* **222**, 10-24 (1995).

59. Israelachvili, J. & Wennerstrom, H. Role of hydration and water structure in biological and colloidal interactions. *Nature* **379**, 219-25 (1996).

60. Napper, D.H. Polymeric Stabilization of Colloidal Dispersions. *Academic Press, New York* (1983).

61. Zhang, Y. et al. PEG-Polypeptide Dual Brush Block Copolymers: Synthesis and Application in Nanoparticle Surface PEGylation. *ACS Macro Lett* **2**, 809-813 (2013).

62. Perry, J.L. et al. PEGylated PRINT nanoparticles: the impact of PEG density on protein binding, macrophage association, biodistribution, and pharmacokinetics. *Nano Lett* **12**, 5304-10 (2012).

63. Deryaguin, B.V. & Landau, L.D. A theory of the stability of strongly charged lyophobic sols and of the adhesion of strongly charged particles in solutions of electrolytes. *Acta Physicochim. USSR* **14**(1941).

64. Verwey, E.J.W. & Overbeek, J.T.G. Theory of the Stability of Lyophobic Colloids. *Elsevier, Amsterdam* (1948).

65. Lourenco, C., Teixeira, M., Simões, S. & Gaspar, R. Steric stabilization of nanoparticles: Size and surface properties. *International Journal of Pharmaceutics* **138**, 1-12 (1996).

66. Hunter, R.J. Foundations of Colloid Science Vol. 1. *Clarendon, Oxford* (1989).

67. Nel, A.E. et al. Understanding biophysicochemical interactions at the nano-bio interface. *Nat Mater* **8**, 543-57 (2009).

68. Min, Y., Akbulut, M., Kristiansen, K., Golan, Y. & Israelachvili, J. The role of interparticle and external forces in nanoparticle assembly. *Nat Mater* **7**, 527-38 (2008).

69. Nel, A., Xia, T., Madler, L. & Li, N. Toxic potential of materials at the nanolevel. *Science* **311**, 622-7 (2006).

70. Dobrovolskaia, M.A. et al. Interaction of colloidal gold nanoparticles with human blood: effects on particle size and analysis of plasma protein binding profiles. *Nanomedicine* **5**, 106-17 (2009).

71. Rocker, C., Potzl, M., Zhang, F., Parak, W.J. & Nienhaus, G.U. A quantitative fluorescence study of protein monolayer formation on colloidal nanoparticles. *Nat Nanotechnol* **4**, 577-80 (2009).

72. Walczyk, D., Bombelli, F.B., Monopoli, M.P., Lynch, I. & Dawson, K.A. What the cell "sees" in bionanoscience. *J Am Chem Soc* **132**, 5761-8 (2010).

73. Lynch, I. & Dawson, K.A. Protein-nanoparticle interactions. *Nano Today* **3**, 40-47 (2008).

74. Monopoli, M.P. et al. Physical-chemical aspects of protein corona: relevance to in vitro and in vivo biological impacts of nanoparticles. *J Am Chem Soc* **133**, 2525-34 (2011).

75. Monopoli, M.P., Aberg, C., Salvati, A. & Dawson, K.A. Biomolecular coronas provide the biological identity of nanosized materials. *Nat Nanotechnol* **7**, 779-86 (2012).

76. Luyts, K., Napierska, D., Nemery, B. & Hoet, P.H.M. How physico-chemical characteristics of nanoparticles cause their toxicity: complex and unresolved interrelations. *Environmental Science: Processes & Impacts* **15**, 23-38 (2013).

77. Saptarshi, S.R., Duschl, A. & Lopata, A.L. Interaction of nanoparticles with proteins: relation to bio-reactivity of the nanoparticle. *J Nanobiotechnology* **11**, 26 (2013).

78. Walkey, C.D. & Chan, W.C. Understanding and controlling the interaction of nanomaterials with proteins in a physiological environment. *Chem Soc Rev* **41**, 2780-99 (2012).

79. Cedervall, T. et al. Understanding the nanoparticle-protein corona using methods to quantify exchange rates and affinities of proteins for nanoparticles. *Proc Natl Acad Sci U S A* **104**, 2050-5 (2007).

80. Vroman, L., Adams, A.L., Fischer, G.C. & Munoz, P.C. Interaction of high molecular weight kininogen, factor XII, and fibrinogen in plasma at interfaces. *Blood* **55**, 156-9 (1980).

81. Tenzer, S. et al. Rapid formation of plasma protein corona critically affects nanoparticle pathophysiology. *Nat Nanotechnol* **8**, 772-81 (2013).

82. Gilbert, B., Huang, F., Zhang, H., Waychunas, G.A. & Banfield, J.F. Nanoparticles: strained and stiff. *Science* **305**, 651-4 (2004).

83. Linse, S. et al. Nucleation of protein fibrillation by nanoparticles. *Proc Natl Acad Sci U S A* **104**, 8691-6 (2007).

84. Vertegel, A.A., Siegel, R.W. & Dordick, J.S. Silica nanoparticle size influences the structure and enzymatic activity of adsorbed lysozyme. *Langmuir* **20**, 6800-7 (2004).

85. Muro, E. et al. Comparing intracellular stability and targeting of sulfobetaine quantum dots with other surface chemistries in live cells. *Small* **8**, 1029-37 (2012).

86. Xu, J. et al. Nanoblade delivery and incorporation of quantum dot conjugates into tubulin networks in live cells. *Nano Lett* **12**, 5669-72 (2012).

87. Luby-Phelps, K. Cytoarchitecture and physical properties of cytoplasm: volume, viscosity, diffusion, intracellular surface area. *Int Rev Cytol* **192**, 189-221 (2000).

88. Verkman, A.S. Solute and macromolecule diffusion in cellular aqueous compartments. *Trends Biochem Sci* **27**, 27-33 (2002).

89. Swaminathan, R., Hoang, C.P. & Verkman, A.S. Photobleaching recovery and anisotropy decay of green fluorescent protein GFP-S65T in solution and cells: cytoplasmic viscosity probed by green fluorescent protein translational and rotational diffusion. *Biophys J* **72**, 1900-7 (1997).

90. Seksek, O., Biwersi, J. & Verkman, A.S. Translational diffusion of macromolecule-sized solutes in cytoplasm and nucleus. *J Cell Biol* **138**, 131-42 (1997).

91. Kao, H.P., Abney, J.R. & Verkman, A.S. Determinants of the translational mobility of a small solute in cell cytoplasm. *J Cell Biol* **120**, 175-84 (1993).

92. Fushimi, K. & Verkman, A.S. Low viscosity in the aqueous domain of cell cytoplasm measured by picosecond polarization microfluorimetry. *J Cell Biol* **112**, 719-25 (1991).

93. Luby-Phelps, K., Castle, P.E., Taylor, D.L. & Lanni, F. Hindered diffusion of inert tracer particles in the cytoplasm of mouse 3T3 cells. *Proc Natl Acad Sci U S A* **84**, 4910-3 (1987).

94. Los, G.V. & Wood, K. The HaloTag: a novel technology for cell imaging and protein analysis. *Methods Mol Biol* **356**, 195-208 (2006).

95. Los, G.V. et al. HaloTag: a novel protein labeling technology for cell imaging and protein analysis. *ACS Chem Biol* **3**, 373-82 (2008).

96. Heasman, S.J. & Ridley, A.J. Mammalian Rho GTPases: new insights into their functions from in vivo studies. *Nat Rev Mol Cell Biol* **9**, 690-701 (2008).

97. Hall, A. Rho GTPases and the actin cytoskeleton. *Science* **279**, 509-14 (1998).

98. Mackay, D.J. & Hall, A. Rho GTPases. *J Biol Chem* **273**, 20685-8 (1998).

II Site-specific targeting of nanoparticles to proteins inside living cells

5 Introduction

Biocompatible and functionalized nanoparticles (NPs) offer a large number of opportunities to investigate intracellular processes, such as spatiotemporal organization and dynamics of proteins and protein-protein interactions.[1,2] Fluorescent nanoparticles (FNPs) have successfully been applied as probes for highly-resolved localization and long term tracking of cell surface proteins.[3-8] Site-specific labeling of these proteins with FNPs has been accomplished using biomolecules like antibodies, streptavidin/biotin and active-ligands as well as chemical recognition based on immobilized transition metal ions.[3-6,9-12] These recognition units are not applicable for targeting FNPs to cytosolic proteins, because of the missing intracellular bioorthogonality. For instance, the cysteine-based structural integrity of antibodies is often affected by the reducing conditions of the cytoplasm, streptavidin is blocked with endogenous biotin, active-ligands are often limited by the stability of their transient interaction, and transition-metal ions can be coordinated by cysteine-rich proteins. Strategies for intracellular labeling of proteins with nanoparticles have been developed over the last decade, but they are either highly specialized or restricted to the use of fixed cells. [2,13-17]

Therefore, an approach for site-specific and efficient NP targeting to proteins inside living cells is desired. A strategy for a generic use has to be robust, rapid and applicable to a variety of distinct proteins. The development of such an approach, however, remains highly challenging. In contrast to the labeling of cell surface proteins with NPs, the intracellular application is furthermore complicated by the fact that washing out of non-bound NPs is not possible.

Recently, the HaloTag technology has been developed as a highly reactive and modular protein tagging system. It allows covalent binding of a variety of functionalities, via synthetic ligands (HTLs), to a single genetic fusion protein *in cellulo*.[18] This technology has successfully been employed for specific binding of streptavidin coated QDs (^{SAV}QDs) to a cell surface protein fused to the HaloTag.[19]

In this part of the project, we aimed to develop surface functionalization of nanoparticles in order to site-specifically and efficiently target FNPs to HaloTag fusion proteins in the cytoplasm of living cells. First, we investigated binding of FNPs functionalized with a commercial HTL (^{HTL}FNPs) *in cellulo* as well as *in vitro*. Neither significant binding of ^{HTL}FNPs to purified and immobilized HaloTag was observed *in vitro,* nor efficient targeting to HaloTag fusion proteins inside living cells. For this reason, the reaction kinetics of non-modified HTL and HTL-conjugates were investigated in more detail using reflectance interferometry (RIf) and total internal reflection fluorescence spectroscopy (TIRFS) simultaneously.[20] Based on these results, a novel approach for surface functionalization of FNPs was developed using "click"-chemistry. By using this approach, efficient and specific targeting of FNPs functionalized with clickHTL (^{clickHTL}FNPs) to HaloTag fusion proteins was achieved *in cellulo*. Finally, functionalization of FNPs at a very low degree of functionalization allowed tracking of the dynamics of individual mitochondrial membrane proteins labeled by ^{clickHTL}FNPs.

6 Materials and Methods

6.1 Materials

Amine-functionalized fluorescent polystyrene nanoparticles (micromer®-redF, ~20 nm diameter) loaded with rhodamine B (~7 dye molecules/nanoparticle) (amine-FNP) were purchased from Micromod GmbH, (Rostock-Warnemünde/Germany). Dibenzylcyclooctyne-(ethylen glycole)$_{12}$-N-hydroxysuccimid (DBCO-EG$_{12}$-NHS) was purchased from Click Chemistry Tools (Scottsdale/USA). Diamino(polyethylene glycol) MW 2000 was purchased from Rapp Polymere (Tübingen/Germany). Thiol-EG$_4$-functionalized HaloTag-ligand was purchased from Promega (Mannheim/Germany). pEGFP-N1-Lifeact was obtained from Roland Wedlich-Söldner (MPI Martinsried/Germany). pSet7-SNAP::H12 and pSems-Snap-1-26m were obtained from Covalys Bioscience (Witterswil, Switzerland). Protease inhibitor mix was purchased from Serva Electrophoresis (Heidelberg). Other chemicals were purchased from Sigma Aldrich.

6.2 Molecular biology

Cloning of dodecahistidine-tagged HaloTag (pSet7-HaloTag::H12) for prokaryotic expression: The SNAP-Tag gene in the vector pSet7-SNAP::H12 (Covalys Bioscience) was exchanged with the HaloTag gene after restriction with NdeI and NotI. The HaloTag gene was amplified from the vector pFC17A-HaloTag (Promega).

Cloning of hexahistidine-tagged HaloTag fused to mEGFP (pET28b-HaloTag::mEGFP) for prokaryotic expression: Monomeric EGFP (mEGFP) was created by introducing an altered codon A206K into the mEGFP sequence of the Clontech vector pEGFP-N1 (gift from J. Sieber, Göttingen). A HaloTag::mEGFP fusion gene was generated by using pSems-Snap-1-26m (from Covalys Bioscience). After substituting the SNAP gene for the HaloTag gene by restriction with *EcoR*I and *Sbf*I, mEGFP amplified by PCR from pmEGFP-N1 was inserted afterrestriction with *Xho*I and *Not*I. The HaloTag::mEGFP construct was then restricted by *Nde*I and *Not*I and inserted into the prokaryotic expression vector pET28b (purchased from Novagen).

Cloning of Lifeact and Tom_{20} fused to mEGFP and the HaloTag (pSems-Lifeact::mEGFP::HaloTag and pSems-Tom_{20}::mEGFP::HaloTag) for eukaryotic expression: pSems-Lifeact::mEGFP::HaloTag7 and Tom_{20}::mEGFP::HaloTag7 were generated by cassettes cloning as in principle described before.[21] The SNAP-Tag of pSems-Snap-1-26m was substituted for mEGFP after restriction with *EcoR*I and *Xho*I. HaloTag7 was amplified by PCR from pFC17A-HaloTag and inserted into pSems-mEGFP restricted by *Xho*I and *Not*I, resulting into a 48 base pair spacer between mEGFP and HaloTag. Tom_{20} and Lifeact were amplified by PCR from pSems-Tom_{20}::Snap-1-26m (purchased from Covalys) and from pEGFP-N1-Lifeact, respectively and inserted into pSems-mEGFP::HaloTag restricted by *EcoR*V and *EcoR*I.

All cloning steps were performed according to manufacturer's instructions.

6.3 Protein biochemistry

For preparative protein expression *E. coli* BL21 (DE3) (Novagen) were transformed with pSet7-HaloTag::H12 or pET28b-HaloTag::mEGFP. Expression was induced with 0.5 mM IPTG at OD_{600}: 0.6-0.8. Expressing cells were grown for 4 h at 37 °C. Harvested cells were resuspended in 50 mM HEPES, 150 mM NaCl, pH 8.0 supplemented with lysozyme and protease inhibitors. From cell lysate of 1 L *E. coli* culture, the His-tagged proteins were purified to homogeneity by

immobilized metal ion affinity chromatography (5 ml HiTrap Chelating, GE Healthcare) followed by size exclusion chromatography (SEC, Superdex 200 16/60, GE Healthcare) using standard protocols[22,23]. Purity was confirmed by SDS-PAGE MW(HaloTag::H12): ~36 kDa; MW(H6::HaloTag::mEGFP): ~63 kDa). All chromatography steps were performed using a FPLC system (Äkta Explorer, GE Healthcare).

6.4 Organic chemistry and bio-conjugation chemistry

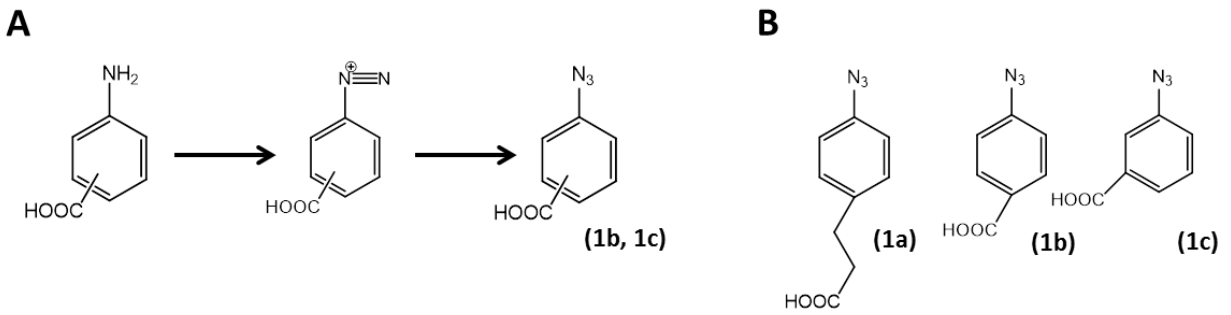

Scheme II.1 Synthesis of (A) Azido-benzoic acid derivatives. (B) Azido derivatives used for structure-function analysis.

Synthesis of 3-azidobenzoic acid (1a) and 4-azidobenzoic acid (1b): A pre-cooled solution of $NaNO_2$ (794 mg, 11,5 mmol) was added dropwise within 2 min on ice to pre-cooled suspensions of 3-aminobenzoic acid or 4-aminobenzoic acid (both 1370 mg, 10 mmol) in 10 ml H_2O and 11 ml conc. HCL. The resulting clear solution was stirred for 20 min. Subsequently, a pre-cooled solution of NaN_3 (715 mg, 11 mmol) in H_2O (8 ml) was drop wise added to obtain the azidobenzoic acid derivate. The final suspension was stirred for 1 h on ice. The product was isolated by filtration, washed four times with 10 ml ice cooled water and dried in the air. ESI-MS: *m/z* 162.1 [M^{-1}]; calc. 163.1.

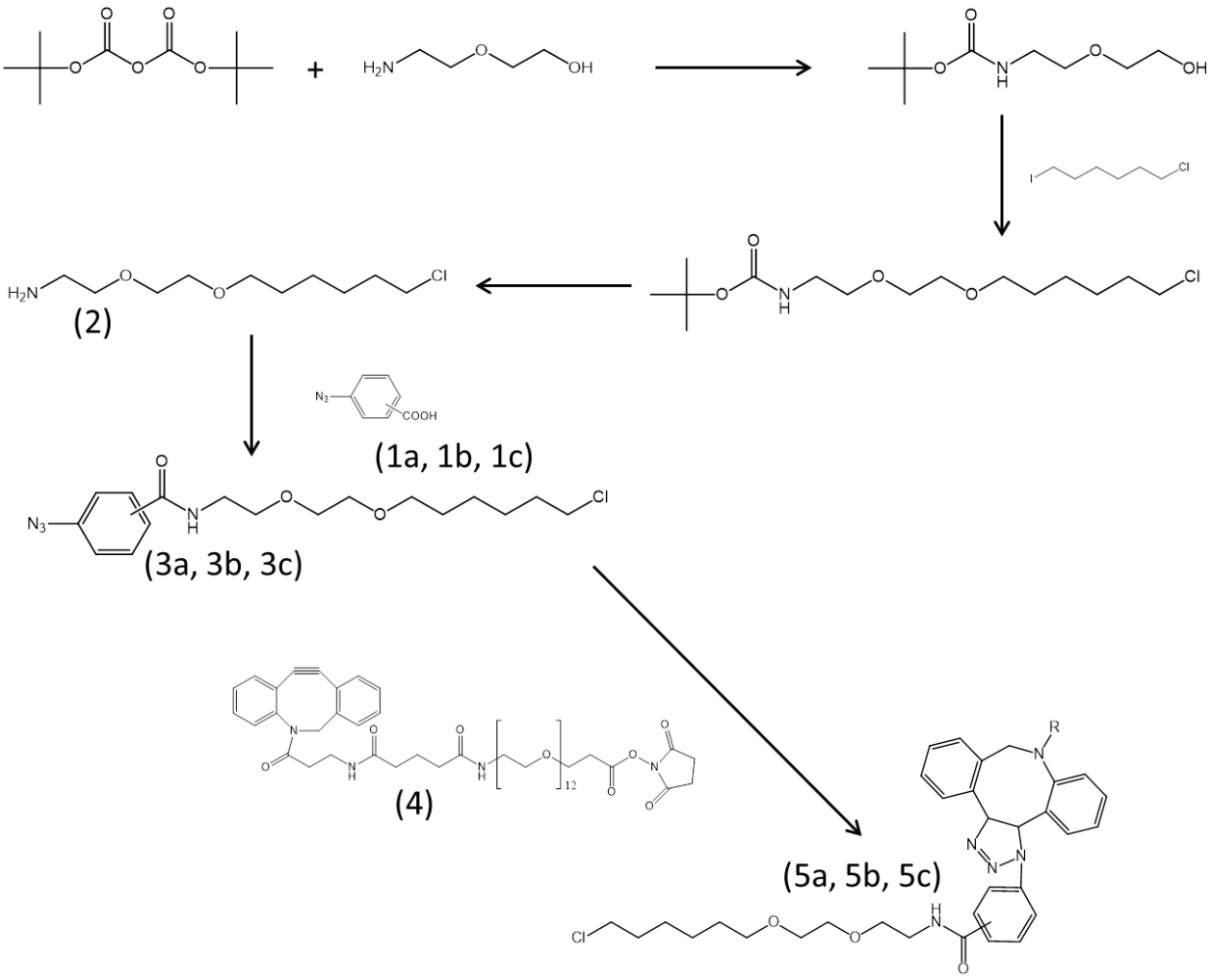

Scheme II.2 Synthesis of clickHTL.

Synthesis of 2-(2-((6-chlorohexyl)oxy)ethoxy)ethanamine (2): Synthesis was performed as described previously.[19] The compound was purified by normal phase chromatography (Vydac 218TP C18) isocratic elution using a 4:1 mixture of ethyl acetate/hexane as eluent. ESI-MS: *m/z* 224.1 [M^{+1}]; calc. 223.1.

Synthesis of azido-(2-(2-(6-chlorohexyloxy)ethoxy)ethyl)amide derivates (3a, 3b, 3c): The coupling agent *O*-(Benzotriazol-1-yl)-N,N,N',N'-tetramethyluronium hexafluorophosphate (HBTU) was added equimolar to a solution of azido derivate **(1a, 1b, 1c)** in anhydrous DMF and the reaction mixture was stirred for 10 min at room temperature. Subsequently, a mixture of an equivalent of **(2)** and five equivalents of N,N-Diisopropoylethylamine (DIPEA) in anhydrous DMF was added further stirred for 2 h at room temperature. After removal of the solvent *in vacuo*, the residue was dissolved in 1 ml acetonitrile and precipitated by the addition of 9 ml water to

obtain compound **(3a, 3b, 3c)** as yellow oil. ESI-MS m/z 397.2 [M^{+1}]; calc. 396.2. For solid surface-based binding assays, compounds **(3a, 3b, 3c)** were further purified. After precipitation, ~0.5 mg of **(3a, 3b, 3c)** were dissolved in 150 µl acetonitrile (ACN) containing 0.2% TFA and diluted with 350 µl H_2O containing 0.2% TFA. The solutions were loaded onto a C18 RP column (Grace Vydac 218TP5u) and eluted using a linear 15-75 % ACN gradient in a HPLC system (Jasco). Finally, the solvent was removed *in vacuo* to obtain **(3a, 3b, 3c)** as yellow oil.

Synthesis of clickHTL derivates (5a, 5b, 5c): 3 fold excess of Dibenzylcyclooctyne-(Ethylen glycol)$_{12}$-N-hydroxysuccimid **(4)** was incubated with **(3a, 3b, 3c)** in 20 mM HEPES, 150 mM NaCl, pH 8.0 for 2 h at room temperature. Solid surface-based binding assays were directly performed with the reaction mixture

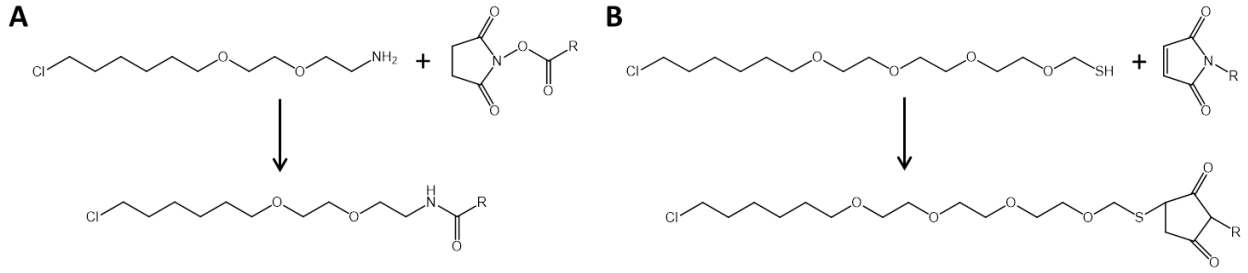

Scheme II.3 Synthesis of HTL-conjugates. (A) Synthesis of HTL-EG$_2$-conjugates by amine/NHS chemistry. (B) Synthesis of HTL-EG$_4$-conjugates by thiol/maleimide chemistry

Coupling of amine containing ligands (A): The reaction of amine-functionalized HTL with succinimidyl esters was carried out with equimolar concentrations of both reactants in DMF in the presence of ten equivalents DIPEA. The reaction mixture was incubated overnight at room temperature and the solvent was evaporated. Subsequently, the product was dissolved in 5% acetonitrile and 0.2% TFA, loaded onto a Halo C8 column (Advanced Materials Technology) and eluted using a linear 5-100 % ACN gradient. Finally, the solvent was removed *in vacuo*.

Coupling of thiol containing ligands (B): The reaction of sulfhydryl-functionalized HTL with maleimide was carried out with equimolar concentrations of both reactants in 20 mM HEPES, 150 mM NaCl, 0.1 mM EDTA, pH 7.5. The reaction mixture was incubated for 1.5 h at room temperature and the solvent was evaporated. Subsequently, the product was dissolved 5% acetonitrile and 0.2% TFA, loaded onto a Halo C8 column (Advanced Materials Technology) and eluted using a linear 5-100 % ACN gradient. Finally, the solvent was removed *in vacuo*.

Reversed phase chromatography was performed using a HPLC system (Jasco). Binding assays were performed with the purified products and without further characterization.

6.5 Nanoparticle functionalization and characterization

Coupling of DBCO-EG$_{12}$-NHS (4): 20 µl of amine-functionalized fluorescent latex beads in water (amine-FNP, 9.5 µM) and 20 µl **(4)** (0.95 mM-4.75 mM, 100-500-fold excess) in 40 mM HEPES, 0.2 mM EDTA, 5 % DMF, pH 8.0 were mixed and allowed to react at room temperature for 1.5 h. Subsequently, FNP were purified by SEC (Superdex 200 5/150) in a HPLC system (Jasco).

Coupling of (3): 2 µl **(3a, 3b, 3c):** (5 mM) in DMF were added into the DBCO-FNP solution and reacted for 3 h at room temperature. ClickHTL-functionalized FNP (clickHTL-FNP) were purified by SEC (Superdex 200 5/150) in PBS, pH 7.4.

Simultaneous coupling of (4) and Biotin-N-Hydroxysuccinimide (Biotin-NHS): 20 µl of H_2N-FNP stock solution (9.5 µM), 1.9 µl Biotin-NHS (10 mM) and 18.1 µl DBCO-EG12-NHS (9.5 mM) in 40 mM HEPES, 0.2 mM EDTA, 5% DMF, pH 8.0 were mixed and allowed to react at room temperature for 1.5 h. Purification was carried out by SEC (Superdex 200 5/150) in HBS, pH 7.4. Coupling of **(3)** was done as described above. ClickHTL-Biotin-FNPs were purified by SEC in HBS, pH 7.4.

Coupling of 3-(Maleimido)propionic acid N-Hydroxy-succinimide ester (MPA-NHS): 20 µl of H_2N-FNP stock solution (H_2N-FNP, 9.5 µM) and 20 µL 3-maleimidopropionic acid NHS ester (MPA-NHS, 9,5 mM) in 40 mM HEPES, 0.2 mM EDTA, 5 % DMF, pH 8.0 containing were mixed and allowed to react at room temperature for 30 min. Maleimide-functionalized FNP (maleimide-FNP) were purified twice using Sephadex G10 spin columns (Harvard Apparatus, Holliston, MA) equilibrated in 20 mM HEPES, 0.1 mM EDTA, pH 7.5.

Coupling of thiol-EG$_4$-HTL: 2.4 µl thiol-EG$_4$-HTL (HS-EG$_4$-HTL, 20 mM) in DMSO were added to 50 µl freshly prepared maleimide-FNP (~3.5 µM). The mixture was incubated for 1.5 h at room temperature. Excess maleimide moieties were blocked by incubation with 2 mM ß-mercaptoethanol at room temperature for 1 h. After blocking, the mixture was purified by SEC in 20 mM HEPES, 0.1 mM EDTA, pH 7.5 as described above.

Coupling of MPA-NHS and Biotin-NHS: 20 µl of amine-FNP in water (9.5 µM), 1.9 µl Biotin-NHS (10 mM) and 18.1 µl MPA-NHS (9.5 mM) in 40 mM HEPES, 0.2 mM EDTA, 5 % DMF, pH 8.0 were mixed and allowed to react at room temperature for 30 min. FNPs were purified by SEC and coupling of HS-EG_4-HTL was done as describe above.

Analytical size-exclusion chromatography (aSEC): To determine the concentration of HTL moieties on functionalized FNPs, a mixture of functionalized FNP (50 nM) and 1.5 µM purified HaloTag::mEGFP in 50 µl HBS, pH 7.4 were incubated for 60 min. The sample was loaded onto a SEC column (Superdex 200 5/150, GE Healthcare), equilibrated with HBS, pH 7.4, using a HPLC system (Jasco) and elution was monitored by a spectral diode array detector (MD-2015 plus, Jasco). To determine the relative amount of proteins of interest bound to HTL-functionalized FNP, the relative concentration was estimated from the signal at 562 nm for clickHTL-FNP and from the signal at 488 nm for EGFP. The final amount of HaloTag::mEGFP bound per FNP was calculated by:

$$DOF = \frac{A_{488} - (0.089 * A_{562})}{A_{562} * 0.083} \qquad \text{(Eqn. II.1)}$$

where *DOF* is the degree of functionalization and *A* is the absorbance at a certain wavelength.

Colloidal properties of FNP: FNP diameter and zeta potential were measured by Malvern Zetasizer Nano ZS (Malvern Instruments Ltd, Worcestershire, UK.). FNP size was determined by NIBS (Non-Invasive Back-scatter) and DLS (Dynamic Light Scattering).

6.6 Solid surface-based binding assays

Surface modification for interaction assays *in vitro:* Surface chemistry was carried out on transducer slides for reflectance interference detection (a thin silica layer on a glass substrate).[24] Surface coating with a thin, amine-terminated PEG polymer brush was carried out as described previously.[25] After surface cleaning in fresh Piranha solution (one part H_2O_2 30 % and two parts concentrated H_2SO_4) the surface was activated with pure (3-Glycidyloxypropyl)trimethoxysilane for 1 h at 75 °C. Subsequently, the surface was incubated with diamino-PEG MW: 2000 Da for 4 h at 75 °C. For immobilization of HaloTag-H12, these

surfaces were functionalized with tris-NTA, as described elsewhere.[26] For immobilization of streptavidin, the PEG-transducer slides were incubated with 10 µl Biotin-NHS (10 mM) in DMF for 10 min at room temperature. Subsequently, the surfaces were washed with DMF.

Interaction assays by real-time solid phase detection: Real-time surface binding assays were carried out by simultaneous fluorescence and mass-sensitive detection based on total internal reflection fluorescence (TIRF) and reflectance interference spectroscopy (RIfS), respectively, using a home-built set-up, which has been described in detail before.[20,27] Green- and orange-fluorescent dyes (EGFP, AF488, TMR and FNP) were excited with the 488 nm line of an argon ion laser (~100 µW excitation energy) and detected through band pass filters 500-600 nm (for EGFP and AF488) and 607/36 (for FNP and TMR), respectively. All surface binding assays were carried out in HBS supplemented with 50 µM EDTA (HBSE). For probing the reaction of HaloTag with fluorescent HTL derivatives as well as functionalized FNPs, HaloTag-H12 was immobilized on a PEG polymer brush functionalized with tris-NTA.[26] Subsequently, HTL-derivatives (100 nM in HBSE) were injected, followed by regeneration of the surface with 200 mM imidazole. The resulting binding curves were fitted using a model for pseudo first-order reaction using Bia-evaluation software. For competitive assays, binding of 150 nM ^{AF488}HTL to immobilized HaloTag-H12 was probed in presence of another HTL derivate in different concentrations. The binding kinetics was fitted by the differential equation for competive binding numerical using Berkley Madonna software.

$$-\frac{dE}{dt} = k_1 * E * S_1 + k_2 * E * S_2 \qquad \text{(Eqn. II.2)}$$

where *k* are the rate constants, *E* is the enzyme concentration and *S* are the substrate concentrations

The reaction of the HaloTag::EGFP with clickHTL-functionalized FNP was probed by immobilizing these FNPs on PEG polymer brush functionalized with biotin. For this purpose, FNP were functionalized with both biotin and clickHTL ($^{clickHTL\text{-}Biotin\text{-}}$FNP) as describe above. $^{clickHTL\text{-}Biotin\text{-}}$FNP were immobilized on biotin-functionalized surfaces after pre-incubation of these FNPs with

a threefold molecular excess of streptavidin. Subsequently, HaloTag::EGFP 1 µM was injected and binding was monitored by RIF and TIRFS.

6.7 Cell biology

Cell culture and transfection. HeLa cells were cultivated at 37°C, 5% CO_2 in MEM supplemented with 10% fetal calf serum (MEM/FCS) and 1% NEAA without addition of antibiotics. HeLa cells were plated on sterilized glass-coverslips in 35 mm cell-culture dishes to a density of about 50% confluence. One day after seeding, cells were transfected *via* calcium phosphate precipitation as described earlier.[21] 24 h after transfection, cells were washed twice with PBS-buffer and medium was exchanged. Cells were typically used for labeling and tracking experiments 48 h after transfection. For the generation of stable cell lines, transfected cells were selected for stable neomycine resistance by cultivation in the presence of 0.8 µg/ml G418 (Calbiochem 345810). Cell clones with homogeneous and moderate expression of labelled proteins were chosen and proliferated.

Microinjection. Functionalized nanoparticles were injected into HeLa cells based on published protocols using an Eppendorf micro manipulation system (InjectMan NI2 and FemtoJet Express). Injection was performed at a capillary pressure between 15-25 psi. Depending on the desired staining density, a solution of 20-75 nM clickHTL-functionalized FNP in PBS was injected. Injection needles (Sutter Instruments; Borosilicate glass with filaments; O.D.: 1.0 mm, I.D. 0.78 mm) were made with a Sutter Instruments P97 micropipette puller using the following parameters: heat: 444; pull: 100; velocity; 38-40; pressure: 500; time: 100.

6.8 Fluorescence microscopy

All cell experiments were performed at 37 °C if not stated otherwise.

Confocal imaging. Ensemble fluorescence imaging was performed in a confocal laser-scanning microscope (CLSM, FluoView 1000, Olympus) equipped with an Argon ion laser (488 nm line for excitation of EGFP) and a 559 nm diode laser (excitation of FNP) as well as two spectral detectors. Sequential line scan was used for dual color imaging. Co-localization analysis was done using Jacob.[28]

Single particle imaging and tracking. Rapid time-lapse imaging for tracking of individual FNPs was carried out with an inverted microscope (Olympus IX71) equipped with a triple color TIR-illumination condenser (Olympus) and a back-illuminated electron multiplied CCD camera (iXon DU897D, 512×512 pixel from Andor Technology). A 488 nm solid state laser (200 mW Sapphire, Coherent) for excitation of EGFP and a 561 nm solid state laser (200 mW, CrystaLaser) for excitation of FNPs were coupled to the microscope through polarization maintaining monomode fibers (KineFlex, Pointsource). A 60× oil objective (PLAPON 60×/1.45 TIRFM, Olympus) with a further 1.6-fold magnification or a 150× oil objective (UAPO 150×/1.45 TIRFM, Olympus) were used for light sheet excitation in EPI-mode. The excitation beam was reflected into the objective by a triple-line dichroic beamsplitter for reflection at 405, 488 and 561 nm and the fluorescence was detected through a triple bandpass filter (filter cube U-M3TIR 405/488/561, Olympus). For simultaneous dual color imaging, an image splitter (DualView, Optical Insight) was employed with a 585 DCXR dichroic beamsplitter (Chroma) in combination with the bandpass filter HQ 525/50 (Chroma) for detection of EGFP and HC 620/52 (Semrock) for detection of FNP. The camera was operated at -80°C at a frame rate of 30 Hz. All fluorescence images were taken at room temperature.

Individual FNP were tracked using the multi-target tracing (MTT) algorithm.[29] Trajectories were further evaluated as described previously.[9] Only trajectories of FNP, which co-localized with mitochondria over the full imaging period, were selected for further evaluation.

7 Results and discussion

7.1 Reaction kinetics of non-modified HTL and HTL-derivates

For targeting nanoparticles to proteins we chose the HaloTag technology because of the reported high reactivity, with a reaction rate constant k_a of 2.7 x 10^6 M^{-1} s^{-1} for HTL conjugated to tetramethylrhodamine (TMR) ($^{TMR}HTL_{EG2}$; Figure II.1 A).[30] However, fluorescent polystyrene nanoparticles covalently functionalized with a commercial and non-modified HTL (Figure II.1 B), yielded no significant binding *in cellulo* and *in vitro*. These results suggested that the reactivity of the used HTL was too low for rapid and efficient FNP targeting. Comparison of both molecule structures (Figure II.1 A and B) indicated that the high reactivity of the $^{TMR}HTL_{EG2}$ might be

mediated by additional interactions of the conjugated dye. In order to optimize this approach for efficient targeting of NPs to proteins, the structure-activity relationship of non-modified HTL and HTL-dye conjugates was investigated in more detail by TIRF/RIfS.

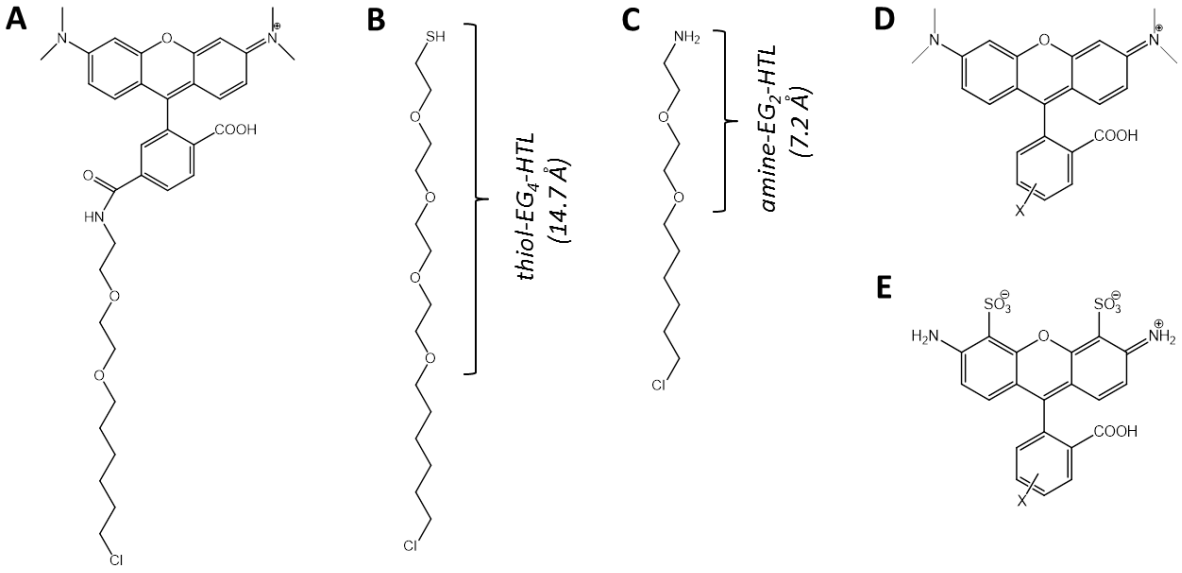

Figure II.1 Non-modified HTL, HTL-conjugate and different chromosphores used for structure activity studies. (A) Tetramethylrhodamine conjugated to amine-EG_2-HTL. (B) Thiol-EG_4-HTL. (C) Amine-EG_2-HTL. (D) Tetramethylrhodamine. (E) Alexa Fluor 488 (AF488).

For these experiments, different dye-scaffolds exhibiting different physicochemical properties in terms of charge and lipophilicity as well as the arrangement of hydrophobic groups (Figure II.1 D-E and 1.4 A), were conjugated to different HTLs, either containing 2 ethylene glycol units as linker (-EG_2-; Figure II.1 C) or an elongated ethylene glycol linker (-EG_4-; Figure II.1 B). The reactivity of HTL-dye conjugates was probed by monitoring in real time the binding to HaloTag-H12, site-specifically immobilized on a poly(ethylene glycol) (PEG) brush (Figure II.2 A). Rapid binding of HTL_{EG2} conjugated to AlexaFluor 488 ($^{AF488}HTL_{EG2}$) was observed (Figure II.2 B, C), yielding a reaction rate constant of 1.3×10^5 M^{-1} s^{-1}.

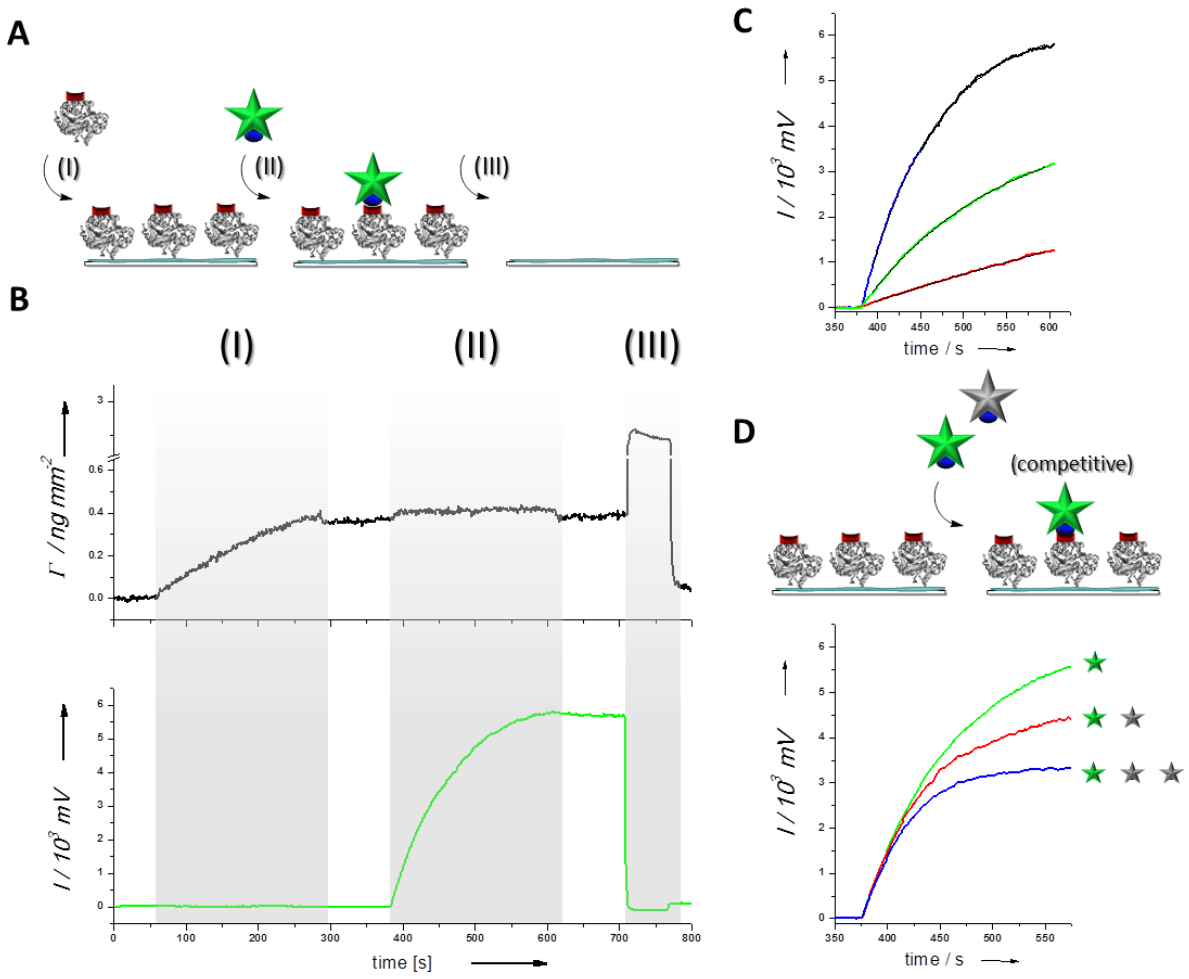

Figure II.2 Solid surface-based binding assays for structure-activity analysis. (A) Schematic illustration of the direct binding assay: Immobilization of HaloTag-H12 on a tris-NTA surface (I), binding of a fluorescent HTL derivate (II), surface regeneration with imidazole (III). (B) Typical measurement: Mass signal (top) and fluorescent signal (bottom) during injection of 100 nM HaloTag-H12 followed by 125 nM $^{AF488}HTL_{EG2}$. (C) Rate constants are given as the mean of three independent measurements at different concentrations (red: 25 nM; green: 50 nM; blue: 125 nM). (D) Competitive binding assay. Reaction of $^{AF488}HTL_{EG2}$ with immobilized HaloTag-H12 in the absence and in the presence of another HTL derivate

In order to directly compare the reaction rate constants of fluorescent and non-fluorescent HTL-conjugates, a competition assay was established with $^{AF488}HTL_{EG2}$ as fluorescent tracer. In this assay, binding of $^{AF488}HTL_{EG2}$ to immobilized HaloTag-H12 was probed in absence and in presence of another HTL derivate at different concentration (Figure II.2 D). Employing the

inhibition assay, the reaction rate constants of non-modified HTL and $HTL_{EG(X)}$-dye conjugates were determined.

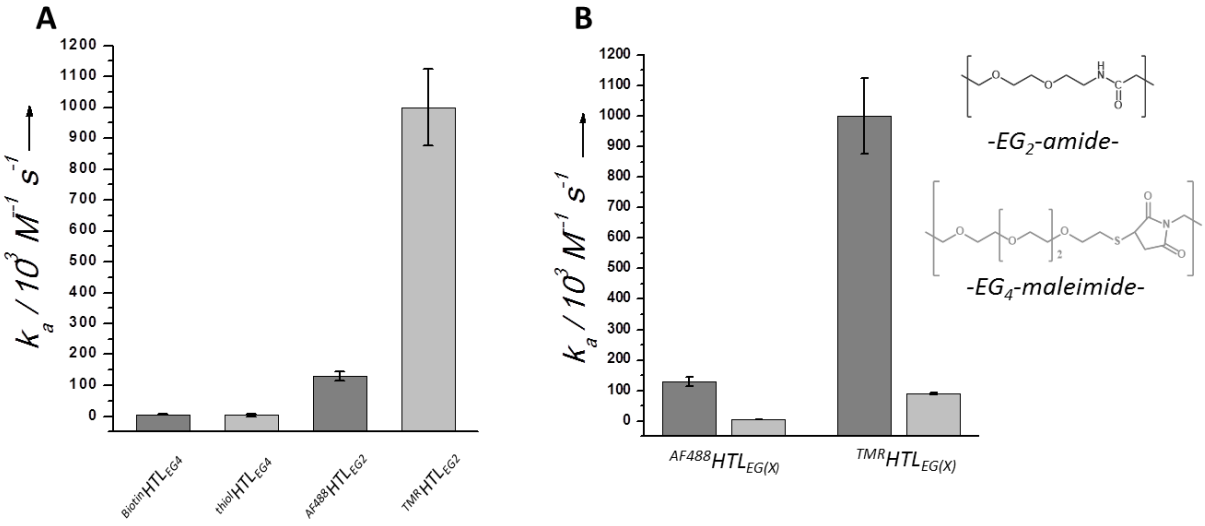

Figure II.3 Comparison of the reactivity of non-modified HTL and different HTL conjugates. (A) Comparison of the reaction rate constants k_a of non-modified HTL and HTL-dye conjugates and the impact of (B) different linker length on k_a.

A high reaction rate constant of > 10^6 M^{-1} s^{-1} was observed for $^{TMR}HTL_{EG2}$ (Figure II.3 A), which is c omparable to the published rate constant of this reaction measured in solution.[30] The reaction rate constants of biotin conjugated to HTL_{EG4} ($^{Biotin}HTL_{EG4}$) and non-modified HTL ($^{thiol}HTL_{EG4}$) were about three orders of magnitude lower (both: ~10^3 M^{-1} s^{-1}). Furthermore, comparison of the reaction rate constants of $^{AF488}HTL_{EG2}$ and $^{TMR}HTL_{EG2}$ (both rhodamine derivatives) indicated that a negative net charge decreases the reactivity (~10 fold). Conjugation of both dyes to an elongated ethylene glycol linker ($^{AF488}HTL_{EG4}$ and $^{TMR}HTL_{EG4}$; Figure II.3 B) substantially decreased the reaction rate constants by about two orders of magnitude compared to the HTL_{EG2}-conjugates. These results provided clear evidence that the conjugated fluorescent dyes play a critical role for the association kinetics, most likely by stabilizing the non-covalent enzyme-substrate complex (ES), based on short range (hydrophobic) interactions, prior to the formation of the covalent "dead-end" complex (EP). Indeed, engineering of the wild type dehalogenase by mutagenesis and screening of the resulting phage display library for enhanced binding rates using $^{TMR}HTL_{EG2}$ involved incorporation of hydrophobic residues in proximity of the HTL binding site.[30] Finally, in order to investigate the binding specificity of the conjugated dye-structure, the

reaction rate constants of three hydrophobic and net non-charged dyes conjugated to HTL_{EG2} were measured (Figure II.4 A).

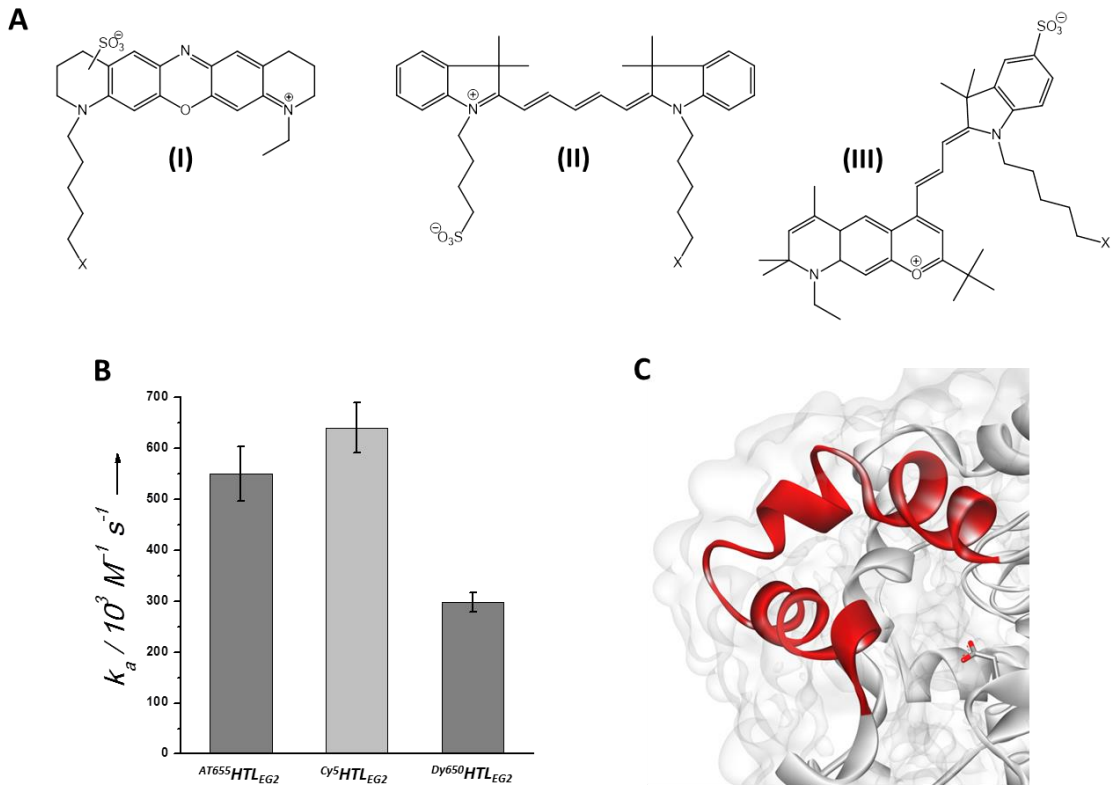

Figure II.4 Binding specificity of the conjugated dye-structure. (A) Chromophores used for structure reactivity analysis. (I) Atto655 (an oxazine derivate), (II) Cy5 (a cyanine derivate) and (III) Dy650 (a cyanine-like derivate). (B) Reaction rate constants k_a of the dyes conjugated to HTL_{EG2}. (C. HTL binding site of the HaloTag. The surface structure involved in substrate recognition and binding is highlighted in red.

High reaction rate constants were observed irrespective of the conjugated dye structure (Figure II.4 B), ranging from 2.9 – 6.5 x 10^5 M^{-1} s^{-1}. This result suggested that the recognition specificity of the enzyme towards the hydrophobic structure conjugated to the HTL_{EG2} is relatively low, maybe due to a high spatial flexibility of the conjugated structure as well as the protein structure depicting the HTL binding pocket on the surface of the HaloTag-enzyme (Figure II.4 C). Computational work on complexes in which one of the reactants is neutral or weakly charged has demonstrated that hydrophobic interactions can be the main driving forces in binding.[31] For the formation of the plastocyanin and cytochrome f complex, it has been shown experimentally that hydrophobic interaction predominantly guided both encounter complex formation and stabilization of the final complex.[32]

7.2 A novel approach for surface functionalization of nanoparticles

Based on the observation that hydrophobic rather than electrostatic interactions play the key role in the association kinetics, we engineered a novel HaloTag-ligand conjugate for surface functionalization of NPs which exhibits hydrophobic moieties. For this purpose, a commercially available dibenzylcyclooctyne-like (DBCO) derivate was conjugated to the HTL_{EG2} functionalized with azidophenylpropionic acid (APP) **(1a)** (Figure II.5 B) by click reaction (clickHTL). In this approach, DBCO and APP were employed as hydrophobic moieties similar to the HTL-dye conjugates (Figure II.5 A and Scheme II.2).

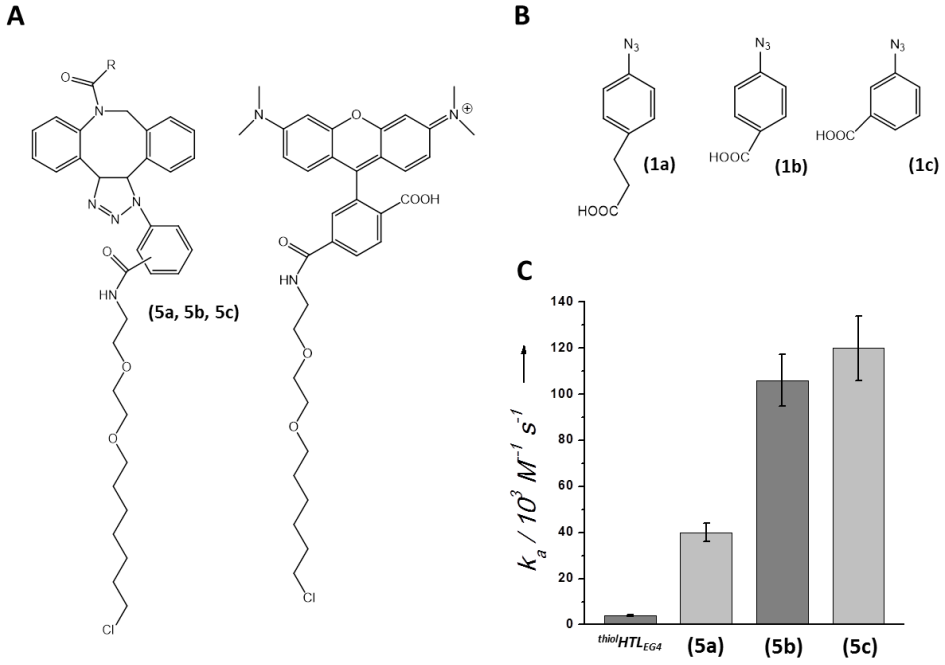

Figure II.5 Reactivity of clickHTL. (A) Structure comparison of clickHTL and $^{TMR}HTL_{EG2}$. (B) Azido-phenylcarboxylic acid derivatives used for structure reactivity analysis. (C) Reaction rate constants k_a of clickHTL derivatives in comparison with the non-modified HTL.

Using the competitive binding assay, an enhanced reactivity of clickHTL **(5a)** towards the HaloTag was obtained, with a rate constant of > 10^4 M^{-1} s^{-1} (Figure II.5 C). This confirmed the stabilization of the non-covalent ES complex by introducing hydrophobic moieties. However, this rate constant was still 1 - 1.5 orders of magnitude lower compared to the hydrophobic HTL_{EG2}-dye conjugates (Figure II.4 A), most likely due to the elongated azidophenylpropionic acid employed as cross linker. In order to obtain a faster reactive clickHTL derivate, two additional azidobenzoic acid derivatives **(1b and 1c)** (Figure II.5 B) were synthezied, with the

azido group in *meta*- and *para*-position, respectively. As expected, the shorter benzoic acid derivatives further increased the reactivity of the clickHTL **(5b and 5c)**, in an orientation independent manner, yielding reaction rate constants of ~ 10^5 M^{-1} s^{-1} (Figure II.5 C). Finally, the reaction rate constant of optimized clickHTL was increased by about two orders of magnitude compared to non-modified HTL.*

7.3 Characterization of ^{clickHTL}FNP targeting *in vitro*

With the improved clickHTL in our hand, amine-presenting polystyrene FNPs loaded with rhodamine B with an average hydrodynamic diameter of 20 nm and a ζ-potential of -26.7 ± 3.6 mV were functionalized with clickHTL **(5a)** (^{clickHTL}FNP) according to Scheme II.4.

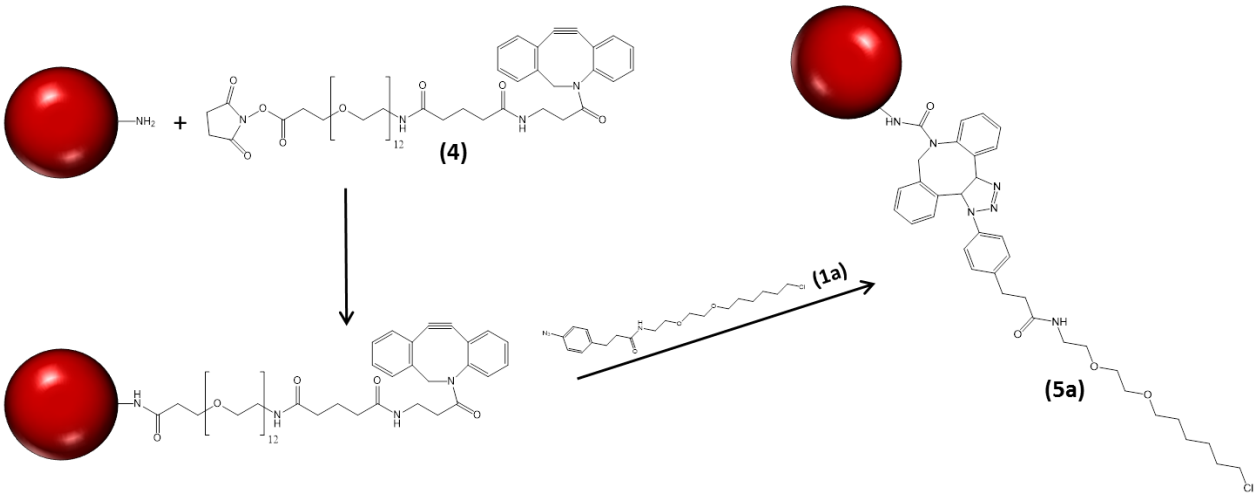

Scheme II.4 Coupling of clickHTL to amine-presenting polystyrene FNPs.

The average degree of functionalization (DOF) was estimated by analytical size exclusion chromatography based on the absorption ratio of mEGFP co-eluted with FNPs (Section 6.5, Eqn. II.1). In so doing, FNPs with DOFs of up to 25 clickHTL units per FNP were synthesized. For direct comparison, FNPs were also functionalized with the non-modified $^{thiol}HTL_{EG4}$ and binding of ^{HTL}FNPs and ^{clickHTL}FNPs to immobilized HaloTag was monitored by simultaneous TIRFS-RIf detection. For ^{clickHTL}FNPs (DOF: 20), fast and specific binding was observed (Figure II.6 A and B), whereas the reaction of ^{HTL}FNPs (DOF: 20) was much slower (Figure II.6 B). In comparison, ^{clickHTL}FNPs yielded a ~ 4 fold higher binding amplitude than ^{HTL}FNPs, confirming the improved

* Since the optimization of the clickHTL was done later in the study, compound **(5a)** was used in chapter II, IV and compound **(5c)** in chapter III

reactivity. However, fitting the resulting binding curves using a model for pseudo first order reactions was not possible due to binding of multivalent FNPs to immobilized HaloTag.

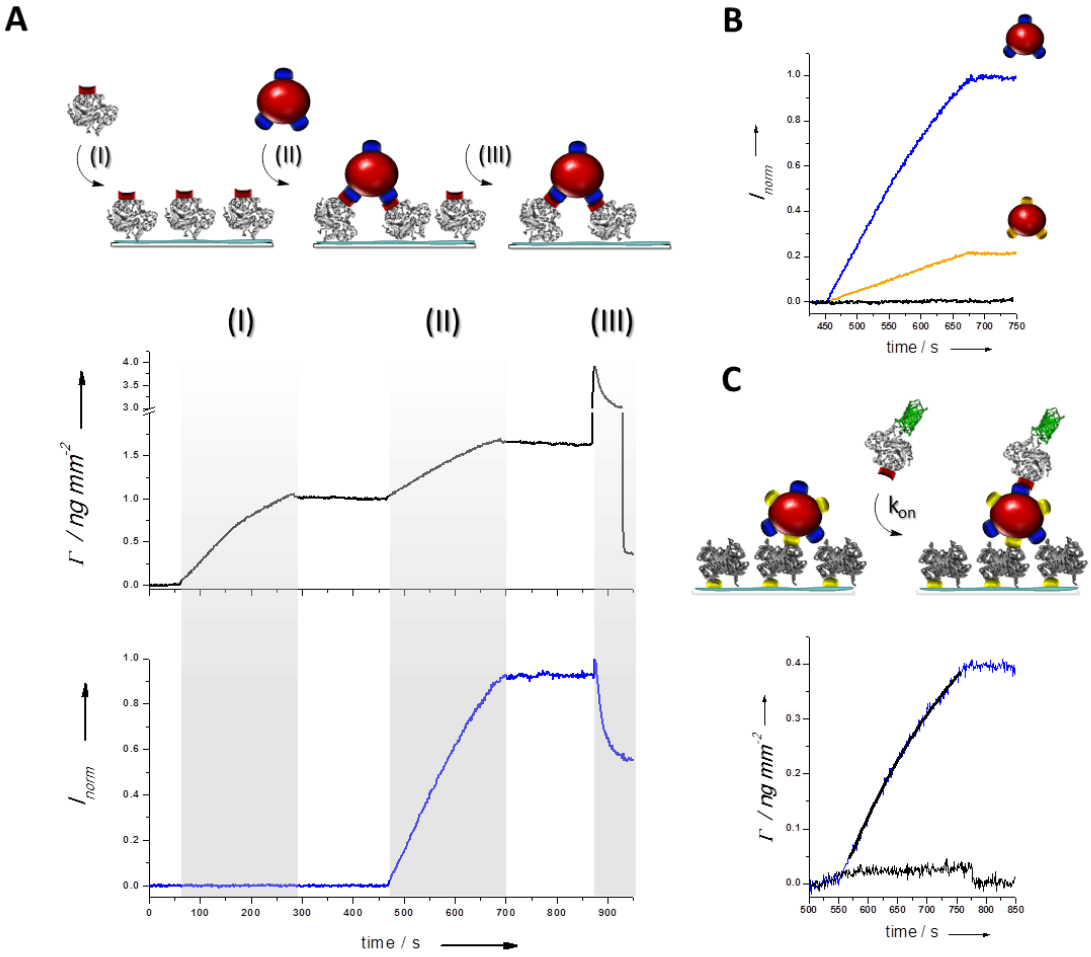

Figure II.6 Reactivity of ^{HTL}FNPs and ^{clickHTL}FNPs in vitro. (A) Binding of ^{clickHTL}*FNPs (5 nM) to immobilized HaloTag-H12 on a tris-NTA surface and (B) in comparison with ^{HTL}FNPs (5 nM; orange) and non-functionalized FNPs (black). Binding signals are normalized with respect to the amount of immobilized HaloTag. (C) Binding of HaloTag::mEGFP (1 µM) to immobilized ^{clickHTL}FNPs (blue) and non-functionalized FNPs (black) as control.*

For this reason, ^{HTL}FNPs as well as ^{clickHTL}FNPs were co-functionalized with biotin for immobilization onto a streptavidin functionalized surface and binding of purified HaloTag fused to mEGFP (HaloTag::mEGFP) (Figure II.6 C) was monitored. Binding of HaloTag::mEGFP to immobilized ^{clickHTL}FNPs yielded a reaction rate constant of 4 x 10^3 M^{-1} s^{-1}, i.e. by one order of magnitude lower compared to direct binding of clickHTL alone. Moreover, binding of HaloTag::mEGFP to immobilized ^{HTL}FNPs was hardly detectable. In comparison with the binding

of $^{thiol}HTL_{EG4}$ and clickHTL (Section 7.2), respectively, these results revealed that the reactivity of both HTL derivatives was strongly decreased when conjugated to FNPs. Thus, the substantially reduced reaction rate constants indicated that binding of HaloTag::mEGFP (pI_{calc}: 5.46) was probably affected by the physicochemical properties of the FNPs. For polystyrene FNPs, the highly negative surface charge (-26.7 ± 3.6 mV) pointed towards electrostatic repulsion, similar to the decreased reactivity of the negatively charged $^{AF488}HTL_{EG2}$.

7.4 Characterization of ^{clickHTL}FNP targeting *in cellulo*

Given by the successful nanoparticle targeting *in vitro*, we next investigated FNP targeting *in cellulo*. For this purpose, Lifeact, a short peptide (17 aa) that reversibly interacts with actin,[33] was fused to both mEGFP and HaloTag (Lifeact::mEGFP::HaloTag). This fusion protein enabled staining of the actin cytoskeleton of living cells and simultaneously served as target for the FNPs. For comparison, FNPs functionalized with HTL, clickHTL and solely with DBCO (^{DBCO}FNPs) as negative control were microinjected into Hela cells stably expressing Lifeact::mEGFP::HaloTag.

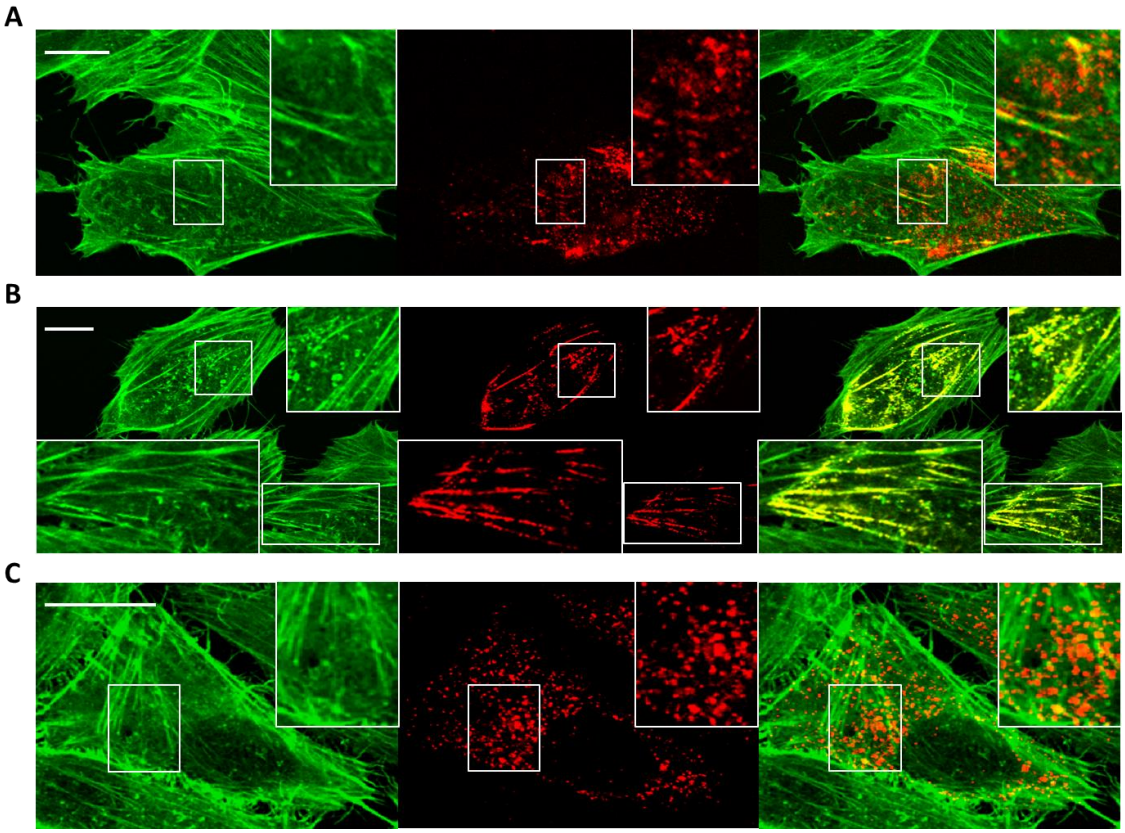

Figure II.7 Specific targeting of FNPs to actin-cytoskeleton. Confocal images of Hela cells stably expressing of Lifeact::mEGFP::HaloTag 1h after micro-injection of (A) ^{HTL}FNPs and (B) ^{clickHTL}FNPs (left: mEGFP channel; middle: FNP channel; right: overlay). (C) As control, micro injection of ^{DBCO}FNPs into the same cell line. The scale bar corresponds to 10 µm in all panels.

1h after microinjection low co-localization (<30%) of the ^{HTL}FNPs (DOF: 20) with actin was observed (Figure II.7 A), whereas the majority of the ^{HTL}FNPs remained unbound in the cytoplasm. On the other hand, high co-localization of ^{clickHTL}FNPs (DOF: 10) with actin filaments

was observed (Figure II.7 B). More than 90% of the ^{clickHTL}FNPs were co-localized with the mEGFP signal.

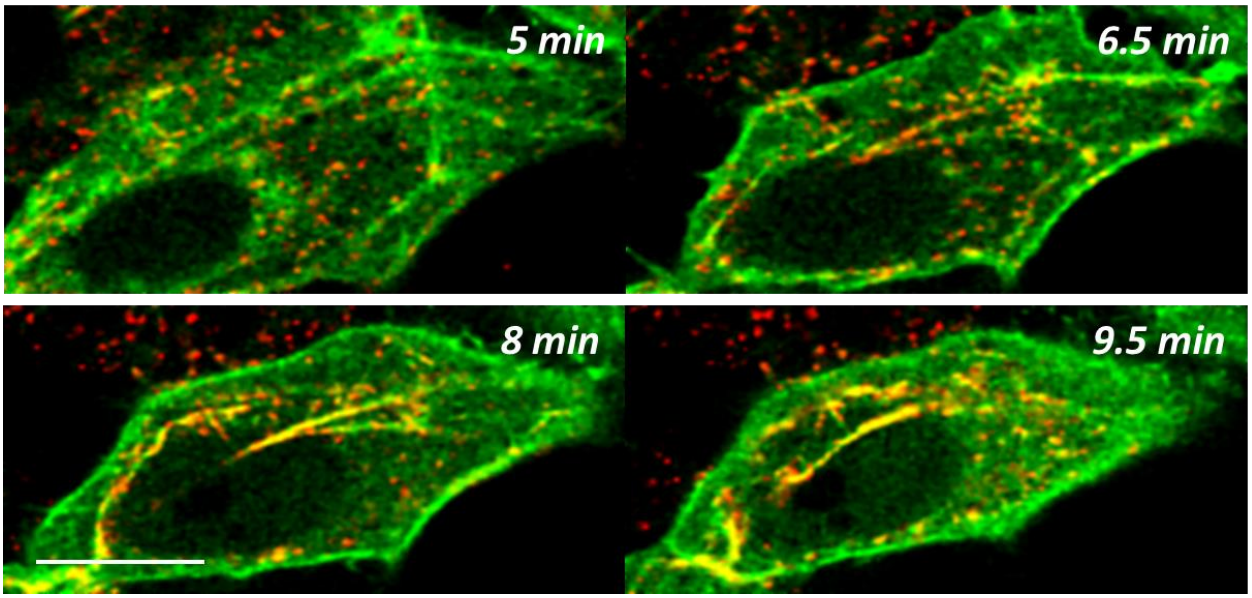

Figure II.8 Specific targeting of ^{clickHTL}FNPs to actin-cytoskeleton. Time-lapse imaging of ^{clickHTL}FNPs binding to the actin cytoskeleton. The scale bar corresponds to 10 µm.

Furthermore, time-lapse confocal imaging revealed rapid binding of ^{clickHTL}FNPs (Figure II.8 and Video 1) to the cytoskeleton; within 10 min almost no free FNPs could be observed anymore. In contrast, no co-localization, but random distribution and the formation of aggregates was observed after micro-injection of ^{DBCO}FNPs (Figure II.7 C). These results indicated that fast reaction is required for efficient and rapid FNP targeting *in cellulo*, probably because of competing non-specific interactions of the FNPs with intracellular components.

7.5 Tracking of individual membrane proteins *in cellulo*

With focus on employing this approach for tracking of single molecules using FNPs, we explored FNP targeting to membrane proteins inside living cells. For this purpose, HaloTag and mEGFP were fused to TOM_{20} (TOM_{20}::mEGFP::HaloTag), a protein import receptor subunit of the translocase of the outer mitochondrial membrane (TOM-complex).

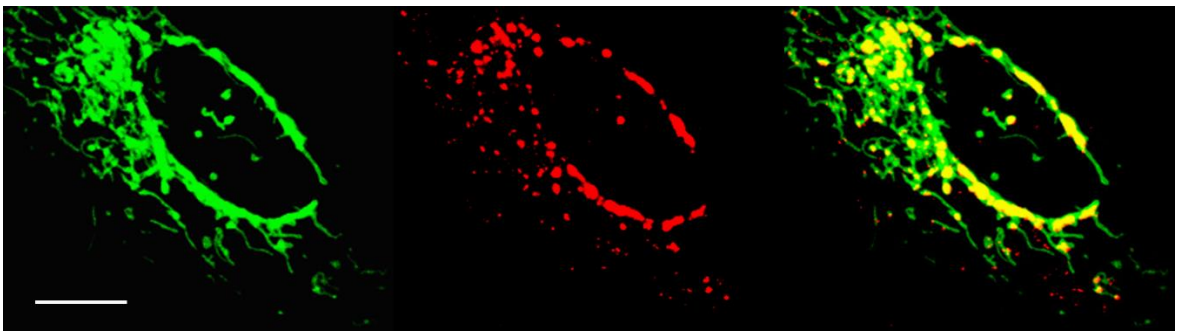

Figure II.9 Specific targeting of ^{clickHTL}FNPs to mitochondria. Confocal imaging of ^{clickHTL}FNPs bound to TOM_{20}. The scale bar corresponds to 5 µm.

After microinjection of ^{clickHTL}FNPs with a DOF of 5 into Hela cells stably expressing TOM_{20}::mEGFP::HaloTag, FNPs were specifically co-localized with mitochondria, confirming that specific FNP targeting to intracellular membrane proteins is possible by this approach (Figure II.9). However, strong cross-linking of mitochondria as indicated by the perturbed morphology as well as very low mobility of these FNPs diffusing along the mitochondria was observed (Video 2). This can be ascribed to the multivalent functionalization. In contrast, in a control experiment after micro- injection of ^{DBCO}FNPs into the same cell line no co-localization was observed (Video 2 and Video 3).

In order to utilize this method for tracking single molecules, we functionalized FNPs at a very low degree of functionalization (DOF: 0.7). This DOF aimed to obtain mono-, bis- and tris-functionalized FNPs. In this approach, the majority of the particles were estimated to exhibit a DOF of zero. After micro-injection of these ^{clickHTL}FNPs into Hela cells stably expressing TOM_{20}::mEGFP::HaloTag substantially higher mobility of these FNPs was observed compared to the higher functionalization degree used for the co-localization experiments (Figure II.10 A and Video 4). About one third of the FNPs were co-localized with mitochondria during the observation time which is in good agreement with the very low degree of functionalization. Thus, tracking of individual FNPs diffusing along the mitochondria was possible. Trajectories

obtained by this approach followed the shape of mitochondria. Single FNPs could be readily tracked up to 10,000 frames and with an average localization precision of 4 nm (data not shown). However, single trajectory analysis revealed inhomogeneous diffusion alternating between free and highly confined diffusion (Figure II.10 B and C I-III). For free diffusion an average diffusion constant of about 0.03 $\mu m^2 s^{-1}$ was obtained. This diffusion constant was 5 fold lower as observed by tracking of TOM_{20} labelled by TMR.[34]

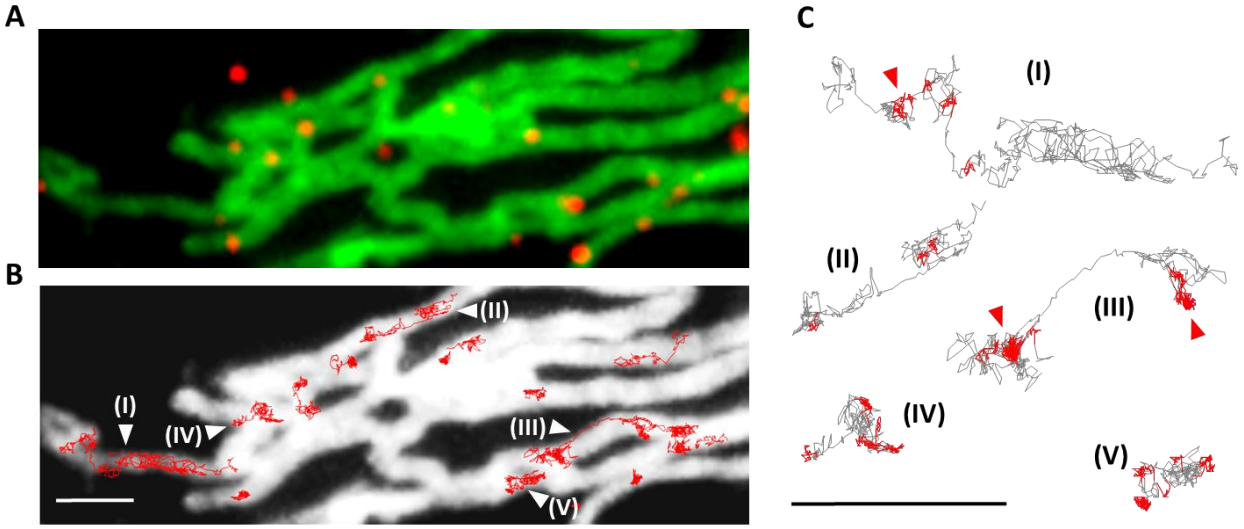

Figure II.10 Tracking single ^{clickHTL}FNPs (DOF: 0.7) bound to TOM_{20}. For comparison, single molecule experiments were performed at room temperature. (A) Single overlay image of individual ^{clickHTL}FNPs bound to TOM_{20}. (B) Evaluated trajectories for individual ^{clickHTL}FNPs diffusing along mitochondria from a stack of 500 images. Trajectories used for analysis are marked by a white arrowhead. (C) Selected trajectories analyzed for transient confinement zones, which are depicted in red. The scale bar corresponds to 500 nm in all panels.

In contrast to the dye-based tracking of TOM_{20}, highly spatial restricted diffusion was observed (Figure II.10 C IV and V). In combination with the confined diffusion, these results suggested that diffusion of FNPs bound to TOM_{20} was affected by non-specific interactions due to the highly negative surface charge, due to steric hindrance based on the size of FNPs, or due to preferential binding of multivalent FNPs, which require further investigation.

8 Summary & Conclusion

Site-specific targeting of nanoparticles to proteins is a key prerequisite for their biophysical application inside living cells. This was achieved by utilizing the HaloTag technology, which had been reported to be highly reactive towards TMR conjugated to HTL_{EG2}. Unmodified HTL was recognized by the HaloTag with low affinity *in cellulo* and *in vitro*. Analysis of the structure-reactivity relationship of different HTL-dye conjugates revealed that short range interactions are the main driving forces for enhanced reactivity. This observation could be confirmed by conjugation of hydrophobic moieties, i.e. DBCO and APP, to non-modified HTL. Enhanced reactivity of clickHTL led to efficient and rapid targeting of FNPs to proteins *in cellulo*. In contrast to conventional targeting strategies, which have extensively been employed for targeting cell surface proteins, the HaloTag technology provides a powerful tool for targeting nanoparticles inside living cells, since the reaction is orthogonal in eukaryotic systems and essentially irreversible. This method further allows to target nanoparticles to plenty of proteins by genetic fusion of HaloTag to the protein of interest. Further enhancement of the reactivity of HTL for NP surface functionalization could be accomplished by synthesis of a rhodamine-like cross-linker, e.g. based on rhodamine 110,[35] similar to $^{TMR}HTL_{EG2}$ conjugate. In combination with the SnapTag,[36] a labelling technology similar to the HaloTag technology, multiplexed targeting of FNPs for simultaneous imaging of two distinct proteins would be facilitated. This method is not restricted to fluorescent nanoparticles and can be extended to other types of nanoparticles exhibiting a variety of surface chemistries. However, rapid binding to target proteins was required for efficient protein labeling with FNPs in the cytosol of living cells. This observation suggested a competition between cellular components and the FNP most likely by non-specific (attractive or repulsive) interactions with structures or compounds of the cytosolic environment. In addition, the effect on protein mobility upon FNP labeling suggested further biases by the FNPs. Thus, the physicochemical properties, i.e. the size, the surface characteristics and the DOF, of the nanoparticles are suggested to be the key determinants for their successful and unbiased intracellular application.

9 References

1. De, M., Ghosh, P.S. & Rotello, V.M. Applications of Nanoparticles in Biology. *Advanced Materials* **20**, 4225-4241 (2008).
2. Biju, V., Itoh, T. & Ishikawa, M. Delivering quantum dots to cells: bioconjugated quantum dots for targeted and nonspecific extracellular and intracellular imaging. *Chem Soc Rev* **39**, 3031-56 (2010).
3. Chang, Y.P., Pinaud, F., Antelman, J. & Weiss, S. Tracking bio-molecules in live cells using quantum dots. *J Biophotonics* **1**, 287-98 (2008).
4. Michalet, X. et al. Quantum dots for live cells, in vivo imaging, and diagnostics. *Science* **307**, 538-44 (2005).
5. Roullier, V. et al. High-affinity labeling and tracking of individual histidine-tagged proteins in live cells using Ni2+ tris-nitrilotriacetic acid quantum dot conjugates. *Nano Lett* **9**, 1228-34 (2009).
6. Lidke, D.S. et al. Quantum dot ligands provide new insights into erbB/HER receptor-mediated signal transduction. *Nat Biotechnol* **22**, 198-203 (2004).
7. Bouzigues, C., Morel, M., Triller, A. & Dahan, M. Asymmetric redistribution of GABA receptors during GABA gradient sensing by nerve growth cones analyzed by single quantum dot imaging. *Proc Natl Acad Sci U S A* **104**, 11251-6 (2007).
8. Dahan, M. et al. Diffusion dynamics of glycine receptors revealed by single-quantum dot tracking. *Science* **302**, 442-5 (2003).
9. You, C. et al. Electrostatically controlled quantum dot monofunctionalization for interrogating the dynamics of protein complexes in living cells. *ACS Chem Biol* **8**, 320-6 (2013).
10. Kim, S. & Bawendi, M.G. Oligomeric ligands for luminescent and stable nanocrystal quantum dots. *J Am Chem Soc* **125**, 14652-3 (2003).
11. Liu, W. et al. Compact biocompatible quantum dots functionalized for cellular imaging. *J Am Chem Soc* **130**, 1274-84 (2008).
12. Alivisatos, A.P., Gu, W. & Larabell, C. Quantum dots as cellular probes. *Annu Rev Biomed Eng* **7**, 55-76 (2005).
13. Pierobon, P. et al. Velocity, processivity, and individual steps of single myosin V molecules in live cells. *Biophys J* **96**, 4268-75 (2009).
14. Lee, S., Lee, K.H., Ha, J.S., Lee, S.G. & Kim, T.K. Small-molecule-based nanoassemblies as inducible nanoprobes for monitoring dynamic molecular interactions inside live cells. *Angew Chem Int Ed Engl* **50**, 8709-13 (2011).
15. Xu, J. et al. Nanoblade delivery and incorporation of quantum dot conjugates into tubulin networks in live cells. *Nano Lett* **12**, 5669-72 (2012).
16. Muro, E. et al. Comparing intracellular stability and targeting of sulfobetaine quantum dots with other surface chemistries in live cells. *Small* **8**, 1029-37 (2012).

17. Delehanty, J.B., Mattoussi, H. & Medintz, I.L. Delivering quantum dots into cells: strategies, progress and remaining issues. *Anal Bioanal Chem* **393**, 1091-105 (2009).

18. Los, G.V. & Wood, K. The HaloTag: a novel technology for cell imaging and protein analysis. *Methods Mol Biol* **356**, 195-208 (2007).

19. So, M.K., Yao, H. & Rao, J. HaloTag protein-mediated specific labeling of living cells with quantum dots. *Biochem Biophys Res Commun* **374**, 419-23 (2008).

20. Gavutis, M., Lata, S., Lamken, P., Muller, P. & Piehler, J. Lateral ligand-receptor interactions on membranes probed by simultaneous fluorescence-interference detection. *Biophys J* **88**, 4289-302 (2005).

21. Muster, B. et al. Respiratory chain complexes in dynamic mitochondria display a patchy distribution in life cells. *PLoS One* **5**, e11910 (2010).

22. GE-Healthcare. Affinity Chromatography: Principles and Methods.

23. GE-Healthcare. Gel Filtration: Principles and Methods.

24. Schmitt, H.-M., Brecht, A., Piehler, J. & Gauglitz, G. An integrated system for optical biomolecular interaction analysis. *Biosensors and Bioelectronics* **12**, 809-816 (1997).

25. Piehler, J., Brecht, A., Valiokas, R., Liedberg, B. & Gauglitz, G. A high-density poly(ethylene glycol) polymer brush for immobilization on glass-type surfaces. *Biosens Bioelectron* **15**, 473-81 (2000).

26. Lata, S. & Piehler, J. Stable and functional immobilization of histidine-tagged proteins via multivalent chelator headgroups on a molecular poly(ethylene glycol) brush. *Anal Chem* **77**, 1096-105 (2005).

27. Gavutis, M., Lata, S. & Piehler, J. Probing 2-dimensional protein-protein interactions on model membranes. *Nat Protoc* **1**, 2091-103 (2006).

28. Dunn, K.W., Kamocka, M.M. & McDonald, J.H. A practical guide to evaluating colocalization in biological microscopy. *Am J Physiol Cell Physiol* **300**, C723-42 (2011).

29. Serge, A., Bertaux, N., Rigneault, H. & Marguet, D. Dynamic multiple-target tracing to probe spatiotemporal cartography of cell membranes. *Nat Methods* **5**, 687-94 (2008).

30. Los, G.V. et al. HaloTag: a novel protein labeling technology for cell imaging and protein analysis. *ACS Chem Biol* **3**, 373-82 (2008).

31. Camacho, C.J., Weng, Z., Vajda, S. & DeLisi, C. Free energy landscapes of encounter complexes in protein-protein association. *Biophys J* **76**, 1166-78 (1999).

32. Scanu, S., Foerster, J.M., Ullmann, G.M. & Ubbink, M. Role of hydrophobic interactions in the encounter complex formation of the plastocyanin and cytochrome f complex revealed by paramagnetic NMR spectroscopy. *J Am Chem Soc* **135**, 7681-92 (2013).

33. Riedl, J. et al. Lifeact: a versatile marker to visualize F-actin. *Nat Methods* **5**, 605-7 (2008).

34. Appelhans, T. et al. Nanoscale organization of mitochondrial microcompartments revealed by combining tracking and localization microscopy. *Nano Lett* **12**, 610-6 (2012).

35. Cai, S.X. et al. Design and synthesis of rhodamine 110 derivative and caspase-3 substrate for enzyme and cell-based fluorescent assay. *Bioorg Med Chem Lett* **11**, 39-42 (2001).

36. Gautier, A. et al. An engineered protein tag for multiprotein labeling in living cells. *Chem Biol* **15**, 128-36 (2008).

III Mono-functional intracellular stealth NPs

10 Introduction

The previous chapter described the development of a generic approach for site-specific and efficient targeting of FNPs to HaloTag fusion proteins in the cytoplasm of living cells. By applying this approach for tracking single molecules in the outer mitochondrial membrane we observed highly confined and slow diffusion of individual FNP-labeled proteins. This was not observed when labeling was performed with organic dyes.[1]

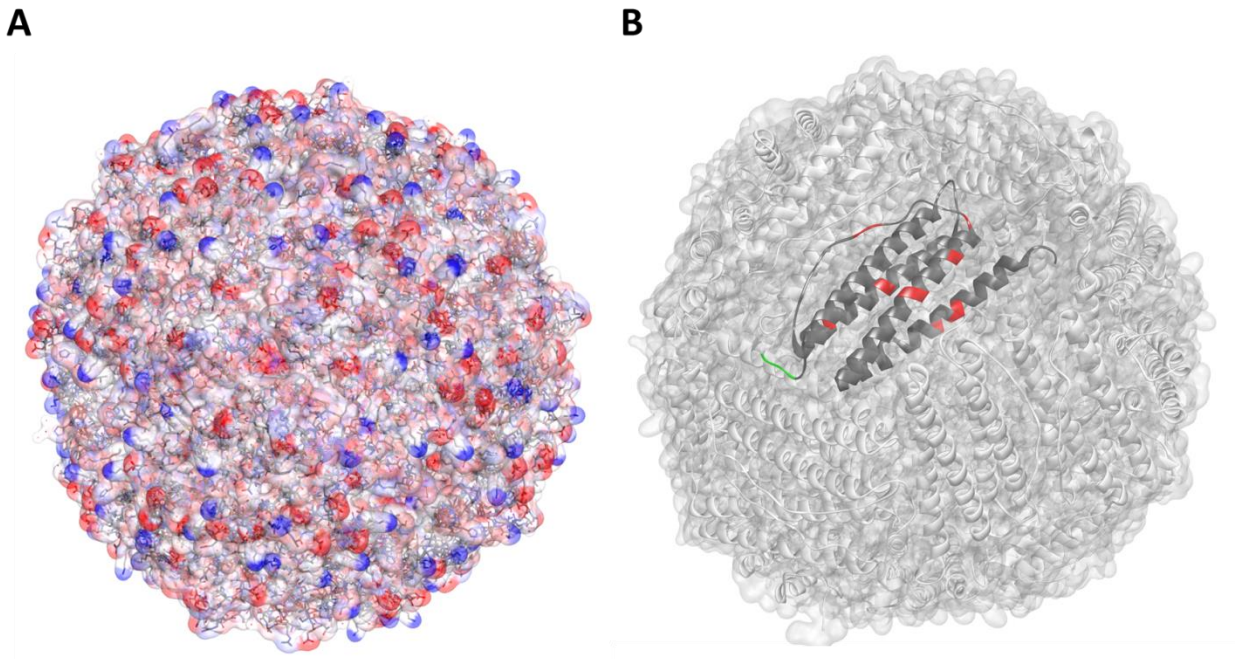

Figure III.1 Surface properties and structure of light chain ferritin (LCF). LCF is composed of 24 subunits of the same type with 12 nm in diameter. (A) Surface charges of LCF. Acidic amino acid residues are highlighted in red, alkaline amino acids residues are highlighted in blue. (B) Protein structure of LCF. A single subunit is highlighted in dark grey. Lysine residues are highlighted in red and the N-terminus is highlighted in green.

For these reasons mono-functional nanoparticles were required, which exhibit intracellular "stealth" properties, i.e they do not interact with cytosolic components and are able to freely diffuse in the cytoplasm. Mono-functionalization of NPs has been developed for labeling of cell surface proteins. This was achieved by means of purification strategies,[2-4] as well

as based on electrostatic steering.[5,6] Extracellular stealth properties have been demonstrated for NPs coated with indifferent polymers *in vitro* and *in vivo.*[7,8] However, combinatorial development of mono-functional stealth nanoparticles accompanied by its efficient and site specific targeting to proteins inside living cells remains unresolved.

In this part of the project, we aimed to systematically engineer FNPs in order to identify physicochemical properties of nanoparticles, which are important for tracking of intracellular membrane proteins without affecting their diffusion dynamics. As a model nanoparticle, the natural protein cage formed by the ferritin light chain was chosen,[9] which offers versatile means for well-defined chemical[10] and genetic[11] modification of surface properties. The stability of LCF was investigated inside HeLa cells. Based on these results, we implemented surface modification of LCF to obtain "stealth" nanoparticles. Subsequently, mono-functionalization of LCF with the clickHTL was developed in order to ensure labeling in a 1:1 stoichiometry. After successful targeting of mono-functionalized LCF to Lifeact and TOM_{20} the dynamics of molecules individual TOM_{20} labeled by LCF was studied.

11 Material and Methods

11.1 Materials

Methoxy-(polyethylene glycol)-N-hydroxysuccimid MW 750 and MW 2000, as well as maleinmidohexanoic-(polyethylene glycol)-N-hydroxysuccimid MW 3000 were purchased from Rapp Polymere (Tübingen/Germany). Dibenzylcyclooctyne- (ethylen glycol)$_4$-maleimide (DBCO-EG_4-mal) was purchased from Click Chemistry Tools (Scottsdale/USA). Cy3-maleimide and Cy5-maleimide were purchased from GE Healthcare (Freiburg/Germany). Atto647N-maleimide was purchased from AttoTec (Siegen/Germany). $(EEG)_3$-C peptide was purchased from Panatecs (Heilbronn/Germany). Other chemicals were purchased from Sigma Aldrich.

11.2 Molecular biology

Cloning of Cys-light chain Ferritin (pSet7-Cys-LCF) for prokaryotic expression: The cDNA of light chain ferritin (LCF) was amplified from HeLa cell lysate using SuperScript® III cDNA synthesis kit (Invitrogen). For site specific maleimide chemistry, a short amino acid sequence of

CSGG was introduced at the N-terminus (Cys-LCF). For bacterial expression of Cys-LCF, the SnapTag gene in the vector pSet7-Snap-H_{12} (Covalys Bioscience) was substituted for Cys-LCF after restriction with the restriction enzymes *EcoR*I and *Xhol*I.

11.3 Protein biochemistry

For preparative overexpression, *E. coli* BL21 (DE3) (Novagen) were transformed with pSet7-Cys-LCF. Expression was induced with 0.5 mM IPTG at OD_{600}: 0.6-0.8. Expressing cells were grown for 4h at 37 °C. Harvested cells were resuspended in 50 mM HEPES, 100 mM NaCl, pH 8.0 supplemented with 5 mM DTT and 0.1 mM EDTA. From the cell lysate, Cys-LCF was purified by heat treatment (70°C, 10 min) twice. The resulting sample was loaded onto an anion exchange column (HiTrap HP-Q; equilibrated with 20 mM HEPES, 100 mM NaCl, pH 8.0 supplemented with 1 mM DTT and 0.1 mM EDTA) and eluted using a linear 0.1-1 M NaCl gradient. Finally, Cys-LCF was purified to homogeneity by size exclusion chromatography (Superdex200 16/60; equilibrated with 20 mM HEPES, 150 mM NaCl pH 8.0 supplemented with 0.1 mM EDTA). Purity was confirmed by SDS-PAGE MW(Cys-LCF): ~21 kDa. All chromatography steps were performed in a FPLC system (Äkta Explorer, GE Healthcare).

11.4 Bio-conjugation chemistry

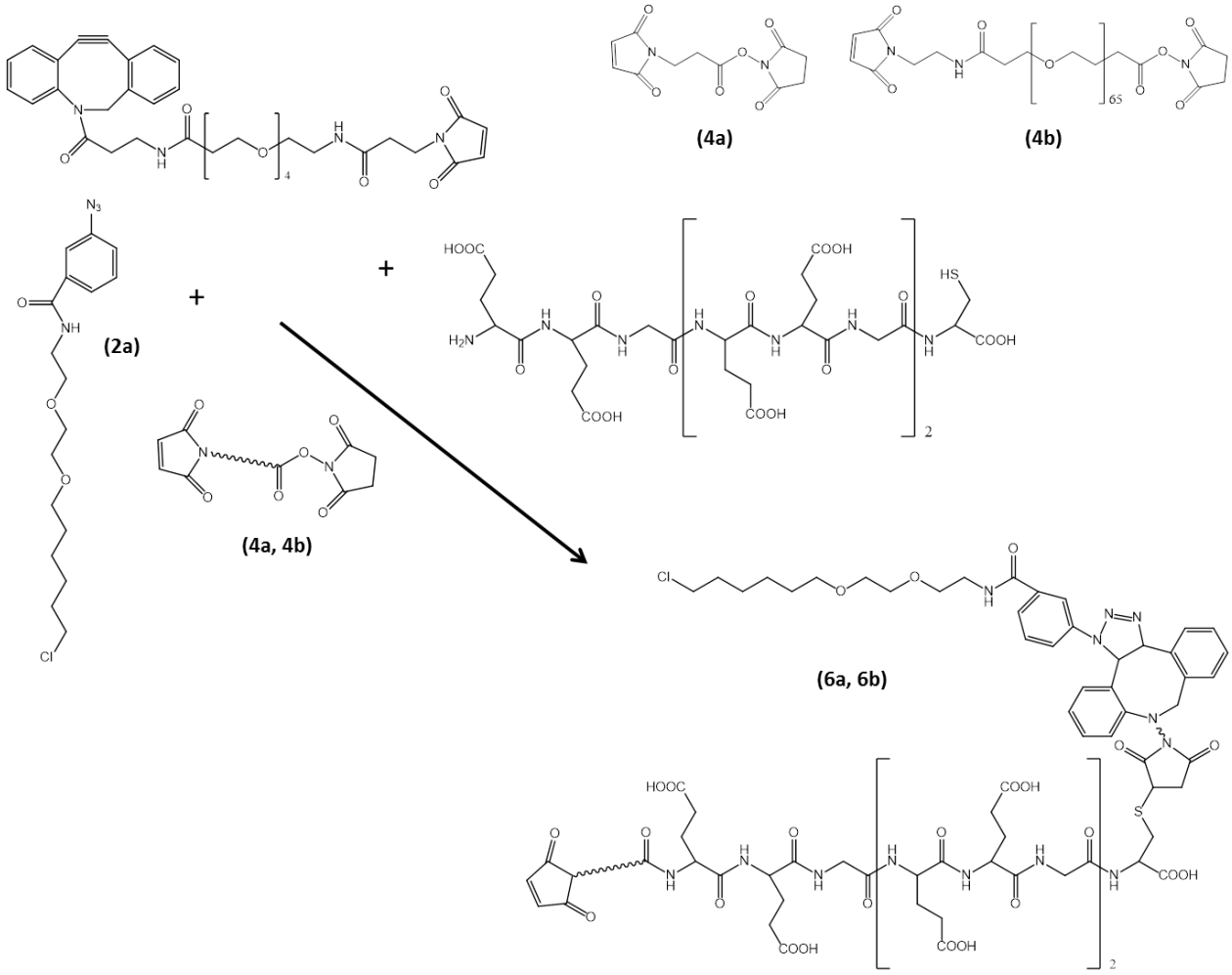

*Scheme III.1 Synthesis of Maleimide-$(EEG)_3$-C-clickHTL derivatives for mono-functionalization of LCF. $(EEG)_3$-C-clickHTL activated by **(6a)** Maleimidopropionic acid N-hydroxysuccinimide ester and **(6b)** Maleimide-PEG_{3k}- N-hydroxysuccinimide ester.*

Maleimide-$(EEG)_3$-C-clickHTL (6a) and Maleimide$_{PEG3k}$-$(EEG)_3$-C-clickHTL (6b): 6.6 µL dibenzylcyclooctyne-EG_4-maleimide (100 mM) in DMSO and 36.6 µl 20 mM HEPES, 500 mM NaCl, pH 7.5 supplemented with 0.1 mM EDTA were added to a solution of 30 µl $(EEG)_3$-C (20 mM) in DMSO. The reaction mixture was incubated for 30 min at room temperature. Subsequently, 4.5 µl **(3c)** (200 mM) in DMSO were added and incubated overnight at room temperature. After removal of the solvent in vacuo, 25 µl **(4a)** (120 mM) or 50 µl **(4b)** (60 mM) in DMSO containing 48 and 24 mM DIPEA, respectively, were added and incubated for 2 h at room temperature. Finally, the reaction mixtures were solved in 8 ml H_2O containing 5%

acetonitrile (ACN) **(5a)** and 30 % ACN **(5b)**, respectively, supplemented with 0.2 % TFA. Precipitates were removed by centrifugation and the solutions were loaded onto a C18 RP column (Grace Vydac 218TP5). The compounds were eluted using a linear 5-50 % ACN **(6a)** and 30-100 % ACN **(6b)** gradient, respectively. MALDI-TOF **(6a)**: *m/z* 2260.8 [M^{-1}]; calc. 2262.1. **(6b)** was used without further analysis.

11.5 Nanoparticle functionalization and characterization

Coupling of succinic anhydrid: 10 µl of succinic anhydride (250 mM) in dry DMSO were added to a solution of 100 µl Cys-LCF (10 µM) in 100 mM HEPES, 150 mM NaCl, pH 8.0 supplemented with 0.1 mM EDTA. The reaction mixture was incubated for 30 min on ice. The excess of succinate was removed by SEC (NAP-5, GE Healthcare). The integrity and physicochemical properties of carboxylated LCF were investigated by analytical SEC, DLS and ζ-potential measurements.

Coupling of methoxy-PEG-NHS derivatives: 15 µl of either methoxy-PEG_{750}-NHS or methoxy-PEG_{2k}-NHS (100 mM) in dry DMSO were added to 100 µl Cys-LCF (10 µM) in 20 mM HEPES, 150 mM NaCl 0.1 mM EDTA, 10% acetone, pH 8.0. The reaction mixture was incubated for 60 min on ice. The excess of poly(ethylenglycol) was removed by SEC on Superdex200 5/150 (GE Healthcare) in a HPLC system (Jasco). The integrity and physicochemical properties of pegylated LCF were investigated by analytical SEC, DLS and ζ-potential measurements.

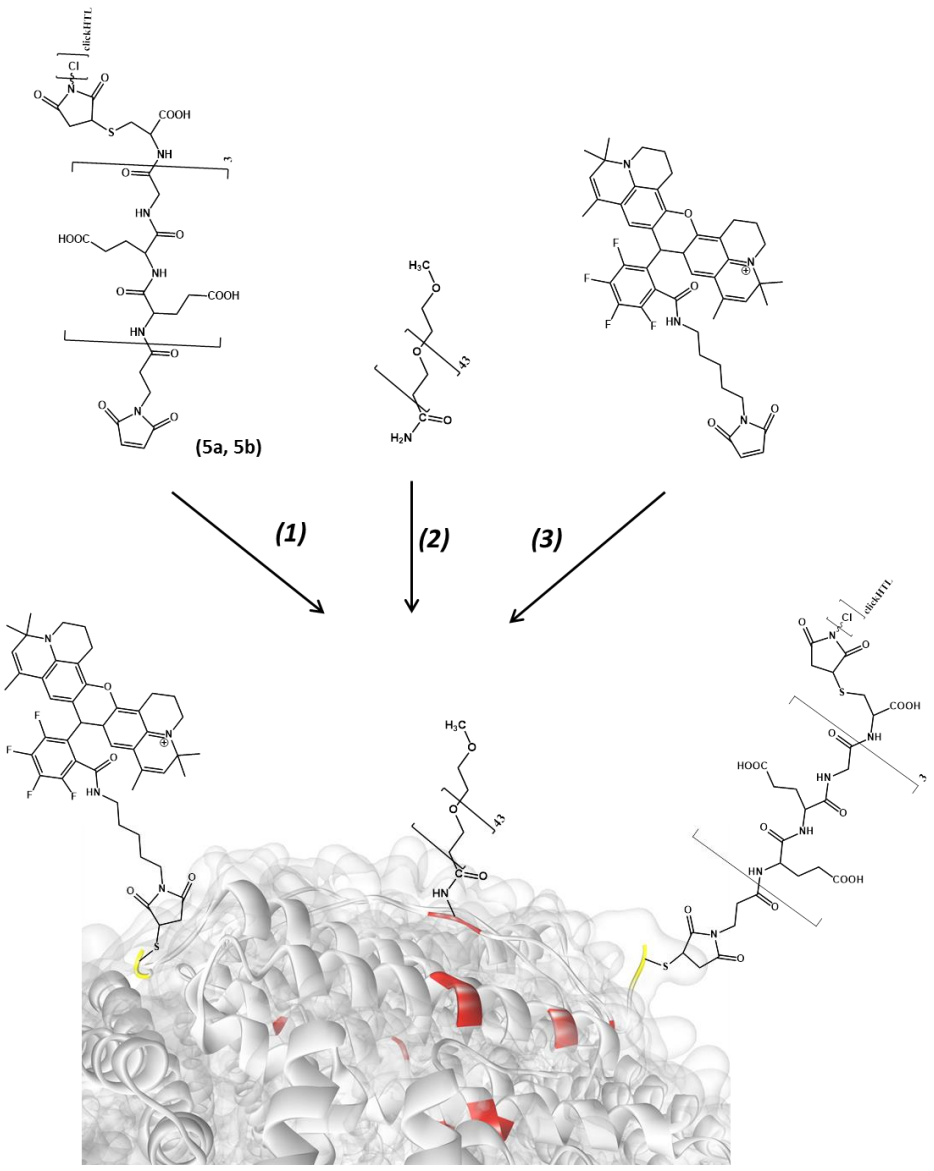

Scheme III.2 LCF surface modifications for the application inside living cells. Coupling of (1) Maleimide-$(EEG)_3$-C-clickHTL, (2) methoxy-PEG_{2k}-NHS and (3) ATTO 647N-Maleimide. Lysine is highlighted in red and the N-terminal cysteine in yellow.

Coupling of Maleimide-$(EEG)_3$-C-clickHTL derivates (6a, 6b): 14 µl of either **(5a)** or **(5b)** (both 2.5 mM) in dry DMSO were added to 1 ml Cys-LCF (10 µM) in 20 mM HEPES, 150 mM NaCl, 0.1 mM EDTA, pH 8.0. The reaction mixture was incubated for 90 min at room temperature and quenched by adding 10 µl reduced cysteine (50 mM) in 20 mM HEPES, 150 mM NaCl, 0.1 mM EDTA, pH 8.0. Subsequently, the reaction mixture was diluted to 100 mM NaCl using 20 mM HEPES, pH 8.0 and loaded onto an anion exchange column (monoQ HR (GE Healthcare); equilibrated with 20 mM HEPES, 100 mM NaCl, 0.1 mM EDTA, pH8.0). The bound

particles were eluted using a linear salt 0.1-0.5 M gradient over 40 column volumes. Mono-functionalized LCF (mLCF) was stored at -80°C until use.

Chromatographical resolution (R)[12] was calculated according to:

$$R = 1.18 * \left(\frac{t_{R2} - t_{R1}}{FWHM_1 + FWHM_2}\right) \qquad \text{(Eqn. III.1)}$$

where t_R is the retention time and *FWHM* describe the half maximum peak width.

Coupling of hydrophilic negatively charged dyes: Prior to pegylation, 0.5-2.5 µl Cy3-maleimide (5 mM) in dry DMSO were added to 50 µL Cys-LCF (10 µM) in 20 mM HEPES, 150 mM NaCl, 0.1 mM EDTA, pH8.0, incubated for 90 min at room temperature and subsequently quenched by adding 2 µl reduced cysteine (50 mM) in 20 mM HEPES, 150 mM NaCl, 0.1 mM EDTA, pH 8.0. Excess of free Cy3 was removed by SEC (NAP-5) and the degree of labeling was estimated by UV/VIS spectrometry.

Coupling of hydrophobic positively charged dyes: After pegylation, 2.5-5 µl ATTO 647N-maleimide (5 mM) in dry DMSO were added to 50 µL Cys-LCF_{PEG2k} (10 µM) in 20 mM HEPES, 150 mM NaCl, 0.1 mM EDTA, pH 8.0, incubated for 90 min at room temperature and quenched by adding 2 µl reduced cysteine (50 mM) in 20 mM HEPES, 150 mM NaCl, 0.1 mM EDTA, pH8.0. The excess of free ATTO 647N was removed by SEC (NAP5) and the degree of labeling was estimated by UV/VIS spectrometry.

Analytical size-exclusion chromatography (aSEC): To determine the stability of FNPs after surface modification, 20 µl of the respective sample were loaded onto a SEC column (Superdex 200 PC 3.2, GE Healthcare) in an HPLC system (Jasco) and elution was monitored using a spectral diode array detector (MD-2015 plus, Jasco).

Colloidal properties of FNP: FNP diameter and ζ-potential were measured by Malvern Zetasizer Nano ZS (Malvern Instruments Ltd, Worcestershire, UK.). FNP size was determined by NIBS (Non-Invasive Back-scatter) and DLS (Dynamic Light Scattering).

The radius of gyration (R_G) for a spherical shell was calculated according to:

$$R_G = \sqrt{\frac{3(R_2^5 - R_1^5)}{5(R_2^3 - R_1^3)}} \qquad \text{(Eqn. III.2)}$$

where R_1 is the inner diameter and R_2 is the outer diameter.

The hydrodynamic diameter was calculated according to:

$$D = \frac{k_B * T}{6 * \pi * \eta * \frac{1}{2} * d_H} \qquad \text{(Eqn. III.3)}$$

where k_B is the Bolzmann-constant, T is the absolute temperature, η is called the viscosity and d_H is the hydrodynamic diameter.

Since the diffusion of indifferent macromolecules (R_G < 30 nm) is 4 – 5 fold slower in the cytosol compared to water,[13] the diffusion of stealth nanoparticle in the cytoplasm was estimated according to:

$$D_{cyto} = \frac{k_B * T}{30 * \pi * \eta * \frac{1}{2} * d_H} \qquad \text{(Eqn. III.4)}$$

Binomial distribution was calculated according to:

$$P = \sum_{i=1}^{k} \binom{n}{k} * p^k * (1-p)^{n-k} \qquad \text{(Eqn. III.5)}$$

where p is the probability for an event to occur, n is the maximal number of events that can occur and k is the number of events that actually occur.

Functionalized LCF for cell experiments was stored in phosphate buffered saline (PBS, pH 7.2) without Mg^{2+} and Ca^{2+} containing 20% glycerol either at 4°C or at -80°C. At 4°C, no significant loss of activity could be observed over several weeks.

11.6 Solid surface-based binding assays

Probing the binding kinetics of mono-functionalized LCF (mLCF) to immobilized HaloTag-H12 was carried out as described in Chapter II (Section 2.6).

11.7 Cell biology

Cultivation and transfection of HeLa cells were carried out as described in Chapter II (Section 6.7). 3T3 fibroblasts were cultivated at 37°C, 5% CO_2 in MEM supplemented with 10% fetal calf serum (MEM/FCS) and 1% NEAA without addition of antibiotics.

11.8 Fluorescence Imaging and Spectroscopy

All cell experiments were performed at 37 °C if not otherwise described.

Fluorescence correlation spectroscopy: Fluorescence correlation spectroscopy (FCS) was carried out in a confocal laser-scanning microscope (Olympus FluoView 1000) with a UPLSAPO 60x/1.2 water immersion objective and a Lifetime/FCS Upgrade Kit (Picoquant) including a 6xx nm pulsed laser diode and a single photon avalanche diode. An emission filter 690/70 was used for detection. Photon traces were recorded with time-correlated single photon counting, which allowed for the application of lifetime filters for background reduction. For calibration of the confocal volume ATTO 655 was employed as reference dye according to the published diffusion constant of 541.1 µm^2/s.[14] *In* vitro as well as inside living cells, ATTO 655, ATTO 647N and Cy5 were excited with a laser output of 50 µW. The recorded data were analysed regarding diffusion with the Sympho Time Software (PicoQuant) and fitted using a model including the contribution of triplet states (eqn. 6).

$$G(\tau) = \left[1 - T + T * e^{\frac{-\tau}{\tau_T}}\right] \sum_{i=1}^{n} \rho_i \left(1 + \frac{\tau}{\tau_i}\right)^{-1} \left(1 + \frac{\tau}{\tau_i K^2}\right)^{-1/2} \qquad \text{(Eqn. III.6)}$$

where ρ is the amplitude of the correlation function, τ_i denotes the diffusion time, τ is the correlation time, T describes the fraction of triplet state and τ_T is the average diffusion time of particles in a triplet state.

Epi-imaging: Ensemble fluorescence imaging was performed in a fluorescence microscope (Zeiss Axiovert 200m) equipped with a X-Cite Series 120 light (Lot-Oiel, France) source and a AxioCam MRn camara (Zeiss).

Estimating the degree of degradation (DOD): In order to estimate the degree of degradation by the amount of aggregated LCF inside living cells, morphological top-hat filtering

of fluorescent-based grayscale images was performed. For this purpose, LCF aggregate signals were specifically isolated by applying a “rolling cylinder” filter, a specializing derivative of the “rolling ball” filter. Finally, the degree of degradation (DOD) was estimated by the fluorescence intensity of aggregated LCF normalized by the total fluorescence intensity of the whole cell.

Binding kinetics of mono-functionalized LCF (mLCF) to mitochondria. The amount of bound mLCF to mitochondria was estimated using the “Rolling Cylinder”-filter as described above. The fluorescence intensity of mLCF bound to mitochondria was normalized by the fluorescence intensity of the whole cell.

Single particle imaging and tracking. Single particle tracking was performed as described in Chapter II (Section 6.8). For comparison with published data, cells were imaged at room temparture.

12 Results and discussion

12.1 Stability of recombinant LCF *in cellulo*

The identity and fate of nanoparticles in biological fluids depends on their physicochemical properties which play a critical role for the composition and the dynamics of the protein corona.[16] Furthermore, clustering of micro-injected FNPs exhibiting different surface modifications has previously been observed in the cytosol.[17-21] Therefore, the stability and fate of LCF inside living cells was investigated first. For this purpose, recombinant LCF was purified to homogeneity and labeled with Cy3 maleimide via N-terminally introduced cysteine residues (^{Cy3}LCF; degree of labeling (DOL): 3). ^{Cy3}LCF in PBS was stable and monodisperse as confirmed by analytical SEC (aSEC) and DLS.

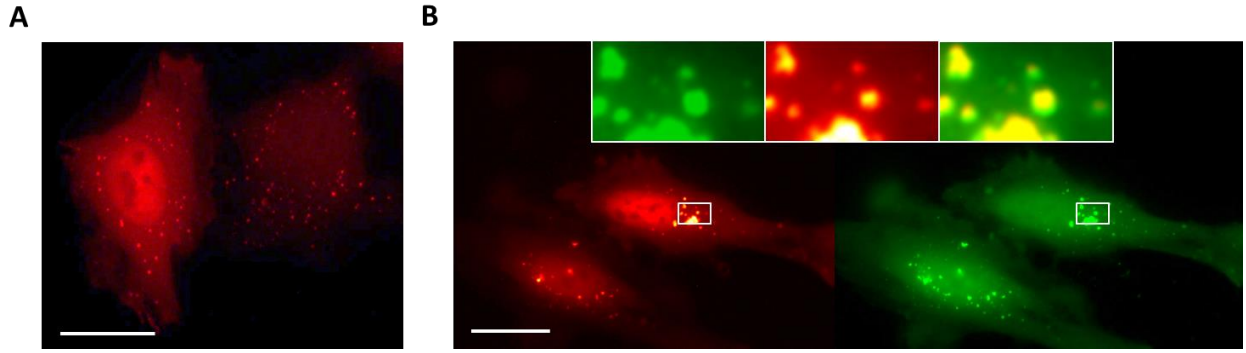

Figure III.2 Stability of LCF inside living cells. EPI images of HeLa cells (A) after microinjection of ^{Cy3}LCF and (B) HeLa cells transiently expressing mEGFP::LC3 after microinjection of ^{Cy3}LCF (green: mEGFP::LC3; red: ^{Cy3}LCF; yellow: overlay). The scale bar corresponds to 10 µm in all images.

After micro-injection into HeLa cells, ^{Cy3}LCF aggregated immediately on a time scale of seconds, as indicated by the formation of bright dots (Figure III.2 A). The fast aggregation of LCF pointed towards recognition by an active metabolic machinery. Therefore, mEGFP tagged LC3 was employed as specific marker for autophagy. In autophagosome formation, LC3 is conjugated to phosphatidylethanolamine (PE) on the autophagosomal membrane to form LC3-II, which remains associated until fusion with lysosomes.[22] Furthermore, LC3 also interacts with p62/SQSTM1, a common constitute of ubiquitinated protein aggregates that act as adapter to facilitate the degradation by autophagy.[23] Strikingly, upon micro-injection of ^{Cy3}LCF into HeLa cells expressing mEGFP::LC3, ^{Cy3}LCF was specifically co-localized with mEGFP::LC3 (Figure III.2 B).

Interestingly, the same behavior was observed also for the protein cage Dps (DNA protection protein during starvation from *Listeria innocua)* which is completely unrelated to LCF. Together, these results suggested a generic recognition of these nanoparticles by the autophagy machinery, most likely caused by the physicochemical nature of the nanoparticle surface.

12.2 Surface modification and physicochemical properties of engineered LCF

In order to minimize LCF recognition by the autophagy machinery, we tested different surface modifications. Since electrostatics have been implicated in FNP stability,[24,25] the slightly negative ζ-potential of -2.2 ± 0.2 mV for the unmodified LCF was decreased by converting surface-exposed amines into carboxyl groups (LCF_{COOH}) by reaction with succinic anhydride (Scheme III.3 A). Furthermore, in order to minimize protein-NP interactions LCF was modified by attaching poly(ethylene glycol) (PEG) via lysine residues using NHS chemistry (Scheme III.3 B). PEG_{750} (LCF_{PEG750}) and PEG_{2k} (LCF_{PEG2k}) with an average of 13 or 42 ethylene glycol units were employed, since the area covered by PEG also depends on their chain length.[7,26]

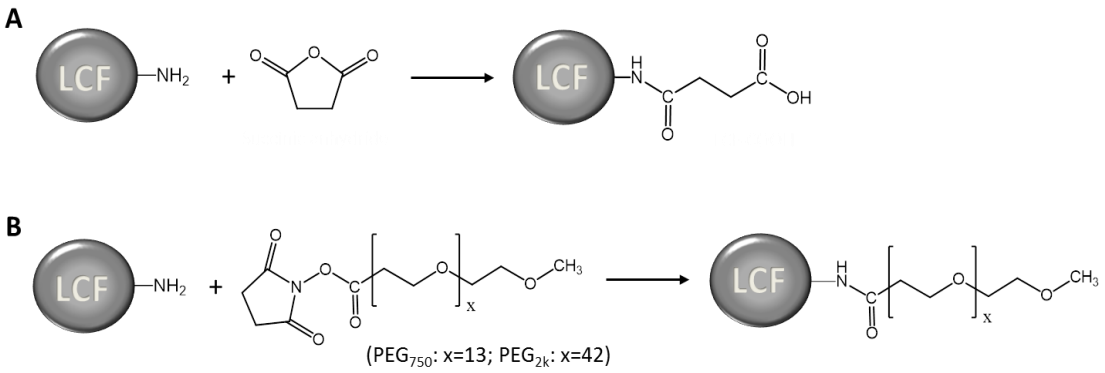

Scheme III.3 Surface modification of LCF. (A) Conversion of ε-amines into carboxyl groups by succinic anhydride. (B) LCF surface PEGylation by using PEG_{750} and PEG_{2k}.

Measurements of the ζ-potential of surface modified LCF revealed an enhanced negative ζ-potential for both the carboxylated (-7.5 ± 0.1 mV) and the PEGylated (LCF_{PEG750}: -6.1 ± 0.3 mV; LCF_{PEG2k}: -6.5 ± 0.4 mV) LCF (Figure III.3 A). The structural integrity of modified LCF before and after the chemical modification was confirmed by aSEC and DLS (Figure III.3 B and C). The modification-dependent size increase of the LCF ranged from 12.3 ± 0.2 nm (LCF) to 16.4 ± 0.4 nm (LCF_{PEG2k}) nm. Mass spectrometry of LCF functionalized with PEG_{2k} revealed 8 PEG chains per subunit (192 chains / LCF particle; 1 chain / 2.3 nm^2). This result is in agreement with the

theoretical number of accessible ε-amine groups (12 Lys / LCF subunit) obtained from the crystal structure (PDB: 3HX7).

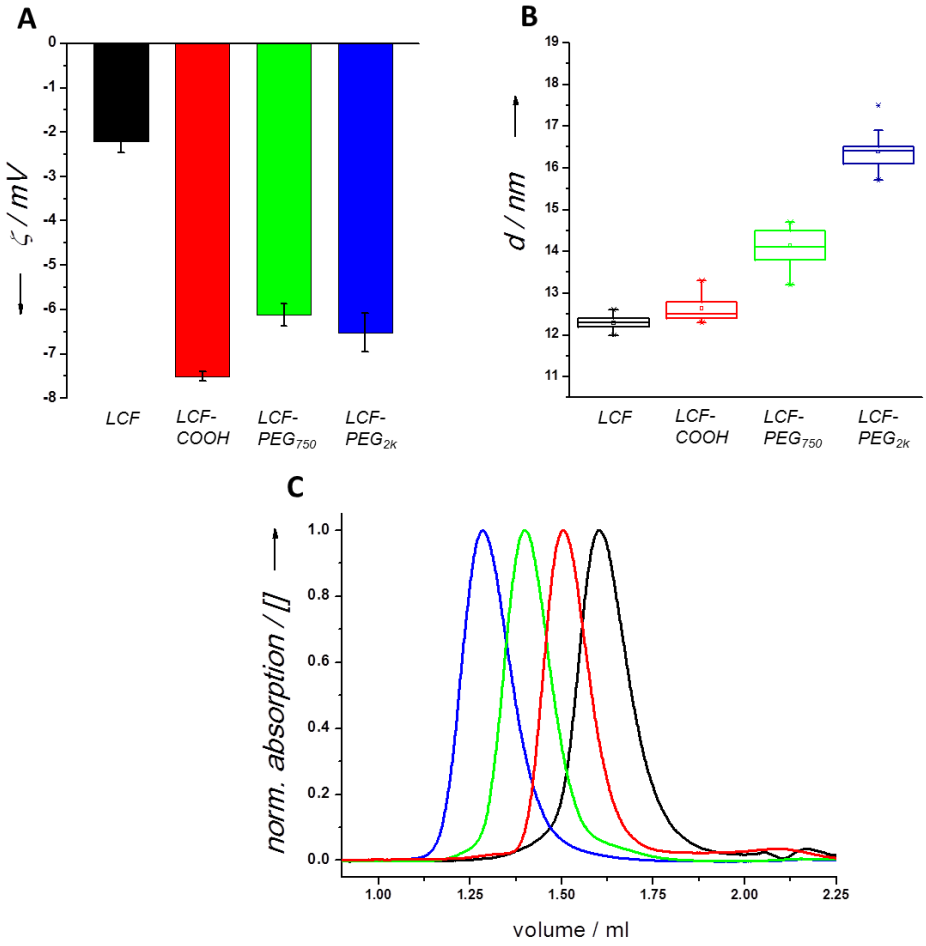

Figure III.3 Physicochemical characterization and integrity of LCF and modified LCF. (A) ζ-potentials (LCF: -2.2 ± 0.3 mV; LCF-COOH: -7.5 ± 0.1 mV; LCF-PEG750: -6.1 ± 0.3 mV; LCF-PEG2k: -6.5 ± 0.4 mV). The data are based on three measurements. (B) Size of LCF and modified LCF as measured by dynamic light scattering (LCF: 12.2 ± 0.1 nm; LCF-COOH: 12.6 ± 0.3 nm; LCF-PEG750: 14.1 ± 0.4 nm; LCF-PEG2k: 16.4 ± 0.4 nm). Data are based on ten measurements. (C) Integrity of LCF and modified LCF (black: LCF; red: LCFCOOH; green: LCFPEG750; blue: LCFPEG2k) measured by analytical SEC.

12.3 Stability and diffusion of engineered LCF *in cellulo*

The stability and aggregation behavior of fluorescently labeled native ^{Cy3}LCF and the chemically modified LCF ($^{Cy3}LCF_{COOH}$; $^{Cy3}LCF_{PEG750}$; $^{Cy3}LCF_{PEG2k}$) were compared after microinjection into the cytoplasm of HeLa cells over a time period of 16h (Figure III.4 A and B).

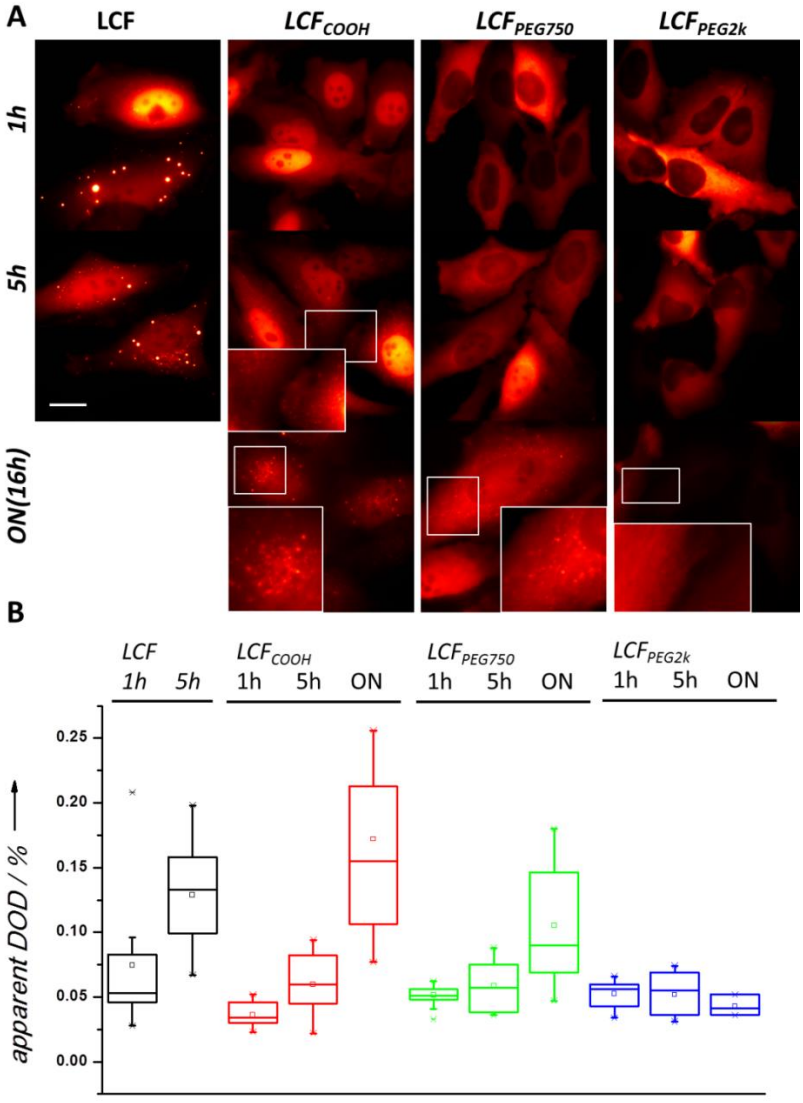

Figure III.4 Aggregation of LCF and engineered LCF inside living cells. (A) HeLa cells after micro-injection of non-modified and modified LCF. The scale bar corresponds to 10 µm. (B) Apparent degree of degradation (DOD) after 1h, 5h and 16h (ON).

While the majority of non-modified ^{Cy3}LCF was aggregated after 5h and completely degraded after 16h, slightly increased persistence of carboxylated ^{Cy3}LCF was observed, most likely by decreasing the metabolisation rate based on electrostatic repulsion. Still, carboxylated

^{Cy3}LCF clearly aggregated within 1 h to 5 h and was almost fully degraded 16 h after microinjection. By contrast, surface PEGylation substantially increased the stability of ^{Cy3}LCF and the majority of particles remained stable for at least 5h. However, 16 h after microinjection some small and isolated aggregates could be observed for ^{Cy3}LCF grafted with PEG_{750}, indicating that the short PEG is still not sufficient to fully protect the particle surface. Further stabilization was achieved by grafting PEG_{2k}, as no significant particle aggregation could be observed within 16 h. These results provide clear evidence that PEGylation of NP surfaces at high densities is beneficial to protect NPs against autophagy. Remarkably, PEGylated LCF remained stable and non-aggregated even at moderate surface charges.

Systematic studies on mobility of indifferent macromolecules (radius of gyration (R_G) <30 nm) have shown that the diffusion of GFP, dextrans and ficolls in the cytoplasm of 3T3 fibroblasts is 4-5 fold slower compared to diffusion in water (D_{cyto} / D_{water}: ~0.25 – 0.20).[13,27,28] In order to detect potential interaction of LCF with intracellular compounds, we compared diffusion of LCF and LCF_{PEG2k} in the cytoplasm of living cells and phosphate buffered saline (PBS). To this end, LCF and LCF_{PEG2k} were labeled with Cy5 (^{Cy5}LCF and $^{Cy5}LCF_{PEG2k}$) and micro-injected into 3T3 fibroblast. Diffusion of PEGylated and non-PEGylated LCF was then probed by FCS. For $^{Cy5}LCF_{PEG2K}$, diffusion in the cytoplasm (D_{cyto}: 13.9 ± 1.2 $\mu m^2\ s^{-1}$) was approximately 5 fold slower than diffusion in PBS (D_{PBS}: 63.6 ± 1.5 $\mu m^2\ s^{-1}$) (Figure III.5 A–C). By contrast, approximately 10-fold slower diffusion was observed for non-modified ^{Cy5}LCF (D_{cyto}: 12.1 ± 0.8 $\mu m^2\ s^{-1}$; D_{PBS}: 104.6 ± 5.6 $\mu m^2\ s^{-1}$), confirming unbiased diffusion of $^{Cy5}LCF_{PEG2k}$ in the cytoplasm of living cells. This result was in line with unbiased diffusion of indifferent macromolecules as described above. Thus, cytosolic stealth properties with respect to metabolic degradation and diffusion were achieved by densely coating LCF with PEG_{2k}.

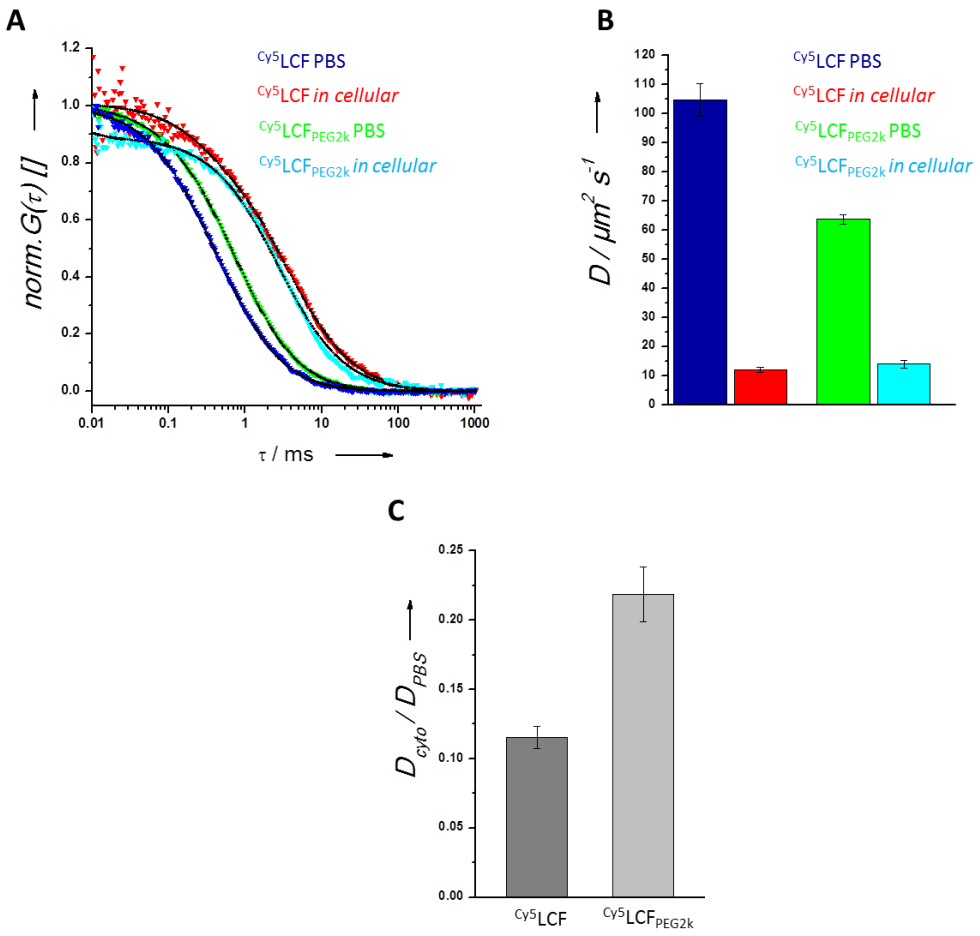

Figure III.5 Intracellular LCF diffusion probed by FCS. (A) Typical autocorrelation curves of ^{Cy5}LCF and modified $^{Cy5}LCF_{PEG2k}$ in PBS or in cellulo. (B) Diffusion constants of LCF and modified LCF. Data are based on five independent measurements. (C) D_{cyto}/D_{PBS} values as criteria for unbiased diffusion inside living cells.

Based on the decelerated diffusion of non-modified LCF in the cytoplasm, the hydrodynamic diameter (d_H) was calculated to be 18.4 ± 0.4 nm, whereas $d_{H,LCF}$ in PBS obtained by dynamic light scattering was 12.2 ± 0.1 nm. The increased hydrodynamic diameter can be explained by formation of a protein-corona around the particles, which are thought to contain or recruit marker for autophagy. The fast degradation of LCF may be connected to xenophagy, where autophagy proteins function in targeting viral particles for lysosomal degradation.[29] Similar to the intracellular antiviral defense, LCF can be recognized as foreign particle and finally degraded by recruitment of specific proteins into the protein corona, which mediate targeting to autophagosomes. This corona either results in the direct labeling of LCF for autophagy or

leads to the aggregation of the particles. Ubiquitinated and p62/SQSTM1 labeled protein aggregates are subsequently recruited into autophagosomes via LC3.[23] However, whether this process is selective based on the physicochemical properties of LCF or simple a random stochastic process is unclear and requires further investigation.

12.4 Mono-functionalization of LCF

With the stealth particles at hand, we aimed to establish mono-functionalization of LCF via the HaloTag for specific labeling of proteins within the cell in a 1:1 ratio. For fast binding kinetics, the optimized clickHTL was employed (Chapter II, section 7.2).

Mono-functionalization of LCF with this clickHTL **(5c)** was implemented following a strategy established for the fractionation of gold nanoparticles functionalized with oligonucleotides.[2] We employed a negatively charged carrier peptide for coupling clickHTL, thus providing a tool for separating LCF with different numbers of functional groups by Anion exchange chromatography (AEX). For this purpose, a peptide comprising three repeats of EEG was functionalized with clickHTL via a C-terminal cysteine residue (Scheme III.1). Finally, maleimide-activated clickHTL-peptide (Scheme III.2) was coupled to cysteine residues introduced on the surface of LCF and subsequently fractionated by AEX (Figure III.6 A).

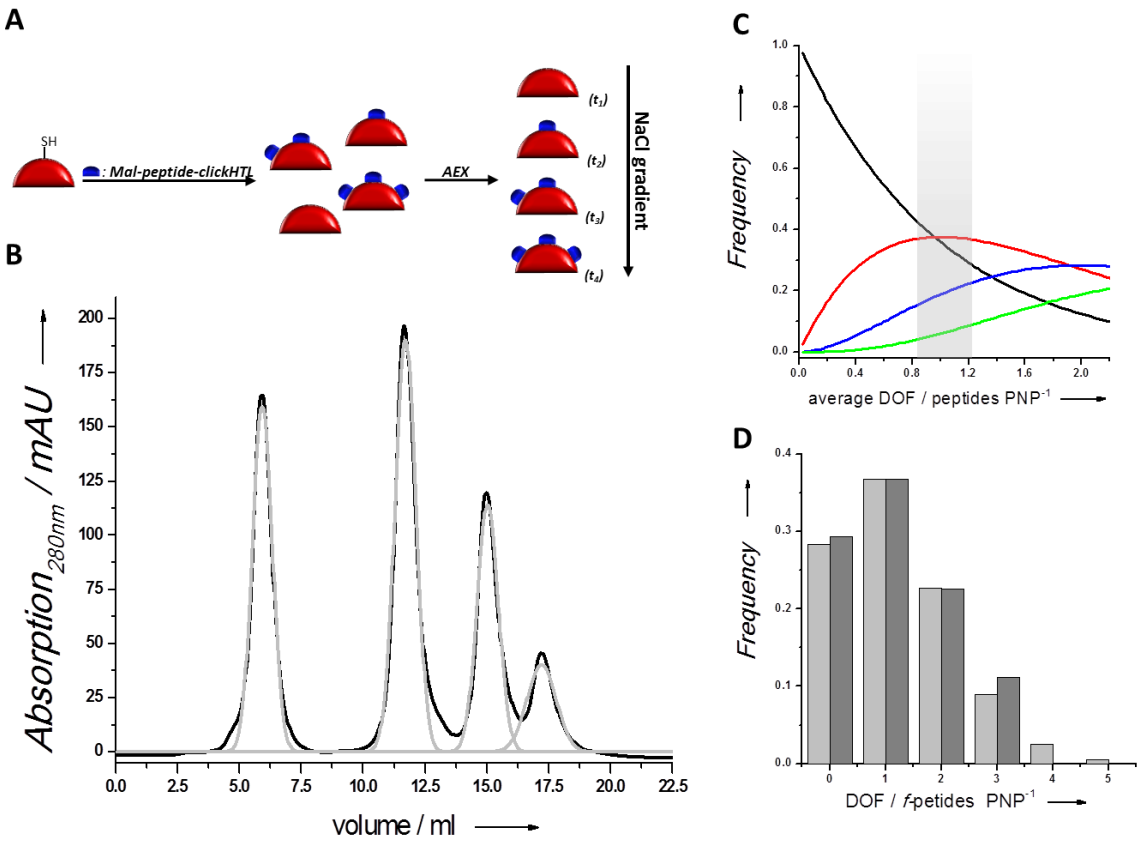

Figure III.6 Purification and characterization of clickHTL peptide-functionalized LCF. (A) Strategy for mono-functionalization of LCF based on the coupling of a maleimide activated clickHTL functionalized peptide as negative charged carrier molecule. (B) Chromatogram obtained by anion exchange chromatography (black: eluted protein fractions monitored at λ= 280nm; light gray: Gaussian fit for quantification of fraction frequencies). (C) Theoretical frequencies of LCF (black), mono-LCF (red), bis-LCF (blue) and tris-LCF (green) as a function of the average degree of functionalization (DOF). The grey bar marks the range with a maximal yield of mono-LCF. (D) Comparison of the functionality distribution of clickHTL-LCF fractionated by AEX (gray) with the calculated distribution (light gray).

Elution of bound LCFs by applying a linear salt gradient yielded a separation of 4 differently charged species (Figure III.6 B), showing the ability to purify LCF carrying a single clickHTL moiety (mLCF) with high resolution (Resolution (R) = 3.9). The experimental data, i.e. the frequency of the eluted fractions from AEX, was modeled using a binomial distribution. In a completely random process, a binomial distribution describes the probability of the formation of an assembly in which two reactants are involved.[30] Quantifying the frequency of each peak eluted from AEX revealed an average degree of functionalization of 1.2, which is located within the

calculated maximum yield of mono-functionalized particles (Figure III.6 C). The corresponding theoretical binomial distribution for an average DOF of 1.2 was similar to the distribution obtained by AEX (Figure III.6 D) except in the formation of tetrakis- and pentakis-functionalized particles, which were not observed experimentally. This can be explained by the finite resolution of the used monoQ beads

12.5 Characterization of mLCF binding to immobilized HaloTag *in vitro*

The kinetics of mono-functionalized particles reacting with purified HaloTag was characterized *in vitro* by TIRFS-RIf detection. For this purpose, mLCF was coated with PEG_{750} ($mLCF_{PEG750}$) or PEG_{2k} ($mLCF_{PEG2k}$) (Figure III.7 A). Additionally, a mLCF was synthesized in a way that the clickHTL was reacted at the terminus of PEG_{3k} as spacer instead of the protein surface directly ($m_{PEG3k}LCF_{PEG2k}$). All mLCF constructs were labeled with Cy5 (DOL: 3). The effect of an increased negative charge on the binding kinetics was furthermore investigated by labeling mLCF with negatively charged Cy5 at different degrees of labeling (DOL: 6, 12 and 18). For non-modified mLCF specific binding to immobilized HaloTag-H12 was observed (Figure III.7 B). From the binding curve a reaction rate constant of $4*10^4$ M^{-1} s^{-1} was obtained for mLCF, which is 50% reduced compared to clickHTL alone. This result indicated that the reactivity of clickHTL was still affected when bound to moderately charged LCF, probably due to localized negative charges of the $(EEG)_3$-C peptide used as carrier molecule. Interestingly, mLCFs coated with PEG_{750} (I), PEG_{2k} (II) and with a PEG3K spacer of the clickHTL (III) yielded similar reaction rate constants (Figure III.7 C). Moreover, no repulsive charge effects were observed for mLCF labeled with an increasing number of Cy5 (Figure III.7 D). These results confirmed robust reactivity of clickHTL independent of the coating and localization of the clickHTL on the LCF surface, as well as of the number of introduced charges. These results confirmed robust reactivity of clickHTL independent of the coating and localization of the clickHTL on the LCF surface, as well as of the number of introduced charges.

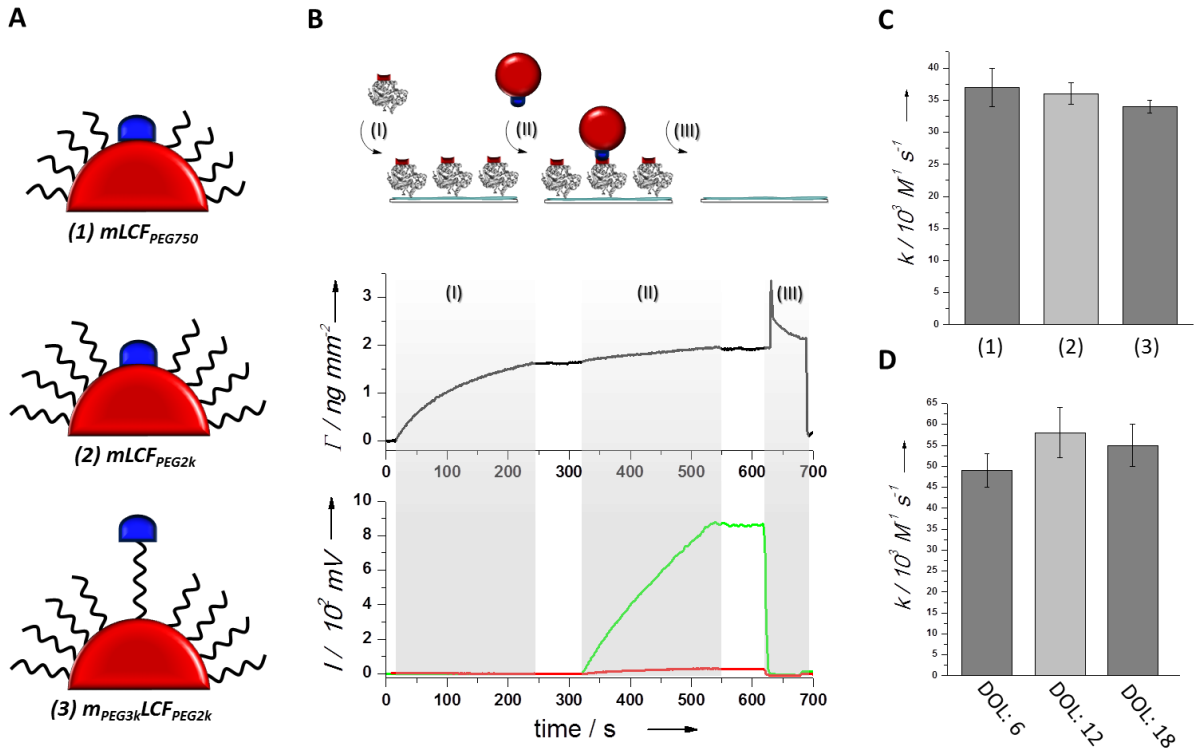

Figure III.7 Probing the reaction rate constants of different modified mLCF with immobilized HaloTag by TIRFS/RIf detection. (A) Distinct ^{Cy5}mLCF surface modifications used for the binding experiments. ^{Cy5}mLCF modified with PEG750 (1), PEG2k (2) and PEG2k where the clickHTL was reacted at the terminus of a PEG3k spacer (3). (B) Typical solid support-based binding experiment: Immobilization of His tagged HaloTag to the Ni^{2+}-loaded tris-NTA surface (I) binding 100nM of ^{Cy5}LCF (red) or ^{Cy5}mLCF (green) (II), followed by surface regeneration with imidazole (III). (C) Reaction rate constants k of ^{Cy5}mLCF modified with PEG750 (1), PEG2k (2) and PEG2k where the clickHTL was reacted at the terminus of a PEG3k spacer (3). (D) Reaction rate constants k of ^{Cy5}mLCF labeled at different degree of labeling.

12.6 Characterization of $mLCF_{PEG2k}$ targeting *in cellulo*

With the mono-functionalized stealth LCF at hand, we next established specific and efficient protein labeling with $mLCF_{PEG2k}$ within the cytosol. Lifeact and Tom_{20} fused to mEGFP and the HaloTag (Lifeact::mEGFP::HaloTag and Tom_{20}::mEGFP::HaloTag, respectively) were employed as model proteins. In a first experiment, $mLCF_{PEG2k}$ labeled with ATTO 647N ($^{AT647N}mLCF_{PEG2k}$, DOL: 12) was injected into HeLa cells stably expressing Lifeact::mEGFP::HaloTag. ATTO 647N was chosen instead of Cy5, since ATTO 647N exhibited higher photo stability and brightness (data not shown).

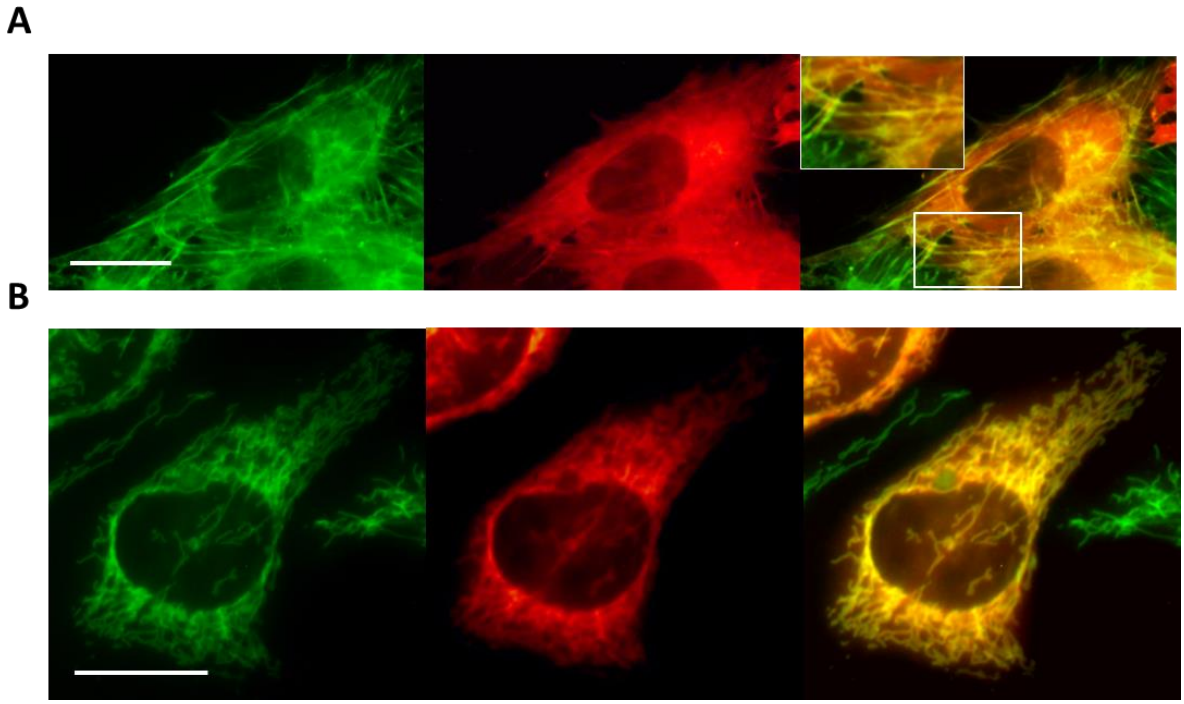

Figure III.8 Specific targeting of $^{AT647N}mLCF_{PEG2k}$ to the actin-cytoskeleton and to mitochondria. EPI images of (A) HeLa cells stably expressing Lifeact::mEGFP::HaloTag 1h after micro injection of $^{AT647N}mLCF_{PEG2k}$ (green: Lifeact::mEGFP::HaloTag; red: $^{AT647N}mLCF_{PEG2k}$; yellow: overlay) and (B) HeLa cells stably expressing Tom20::mEGFP::HaloTag 1h after micro injection of $^{AT647N}mLCF_{PEG2k}$ (green: Tom20::mEGFP::HaloTag; red: $^{AT647N}mLCF_{PEG2k}$; yellow: overlay). The scale bar corresponds to 10 µm in all images.

High co-localization of $^{AT647N}mLCF_{PEG2k}$ with the actin skeleton was observed (Figure III.8 A). After micro-injection into Hela cells stably expressing Tom_{20}::mEGFP::HaloTag, $^{AT647N}mLCF_{PEG2k}$ was also efficiently targeted to the outer membrane of mitochondria (Figure III.8 B).

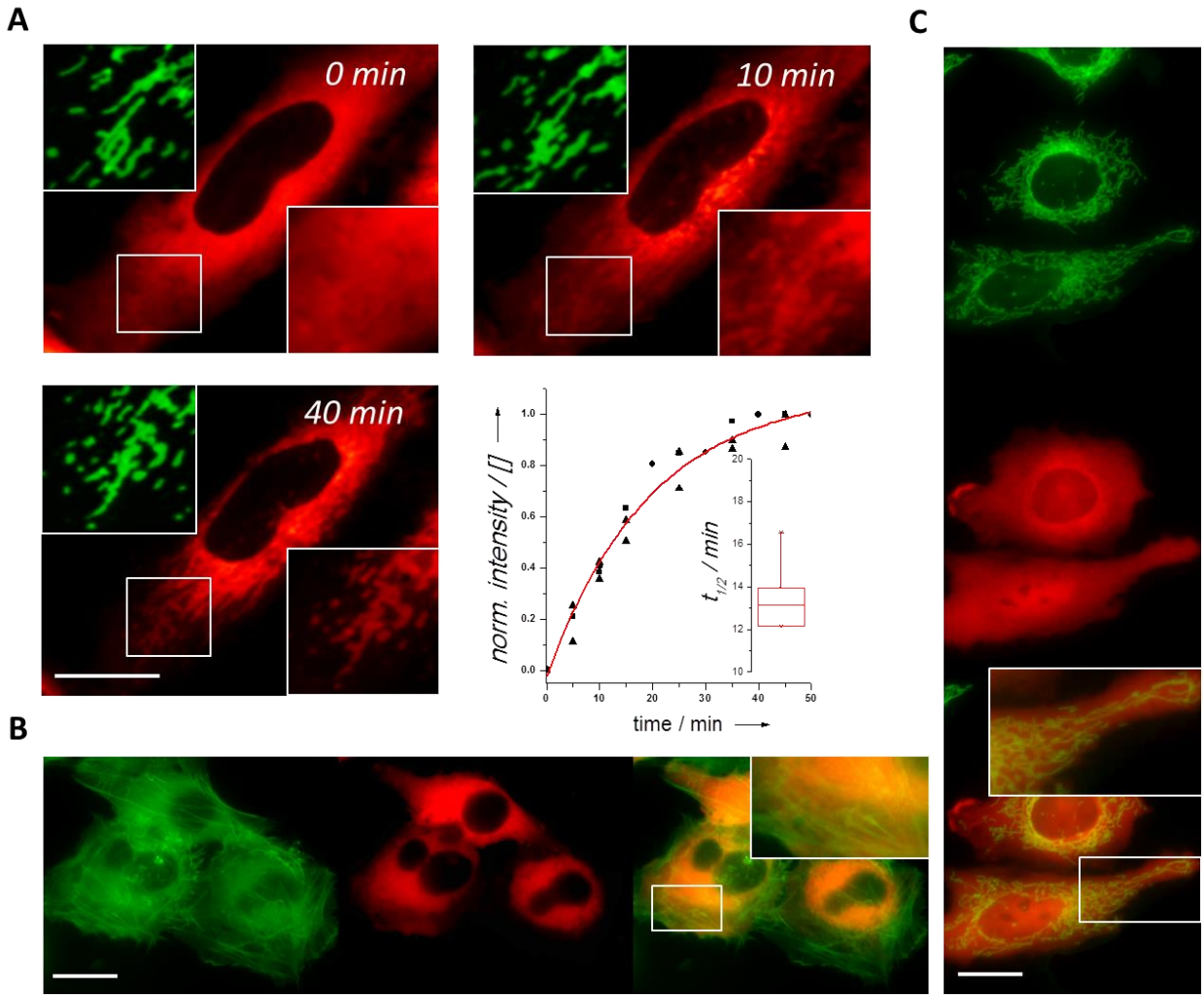

Figure III.9 Quantification of mono-clickHTL LCF targeting to mitochondria. (A) Time-lapse imaging of $^{AT647N}mLCF_{PEG2k}$ (750 nM) binding to mitochondria (green: Tom20::mEGFP::HaloTag; red: $^{AT647N}mLCF_{PEG2k}$) and kinetic of $^{AT647N}mLCF_{PEG2k}$ binding to Tom20::mEGFP::HaloTag (data points of 4 independent measurements were fitted using a mono-exponential). EPI images 1h after micro-injection of $^{AT647N}LCF_{PEG2k}$ without clickHTL into Hela cells stably expressing (B) Lifeact::mEGFP::HaloTag and (C) Tom20::mEGFP::HaloTag. The scale bar corresponds to 10 µm in all images.

Time lapse imaging revealed rapid binding of $^{AT647N}mLCF_{PEG2k}$ to mitochondria. By quantifying the fluorescence increase specifically on mitochondria (Figure III.9 A and Video 5) a functionalization time $\tau_{1/2} \approx 13$ minutes was obtained. Control experiments (Figure III.9 B and C) using particles without clickHTL showed no co-localization. These results suggested that efficient targeting of $^{AT647N}mLCF_{PEG2k}$ to intracellular HaloTag fusion proteins was possible using mono-functionalized particles.

12.7 Tracking of individual membrane proteins *in cellulo*

Finally, the effect on the diffusion of labeling HaloTag::mEGFP::Tom_{20} with $^{AT647N}mLCF_{PEG2k}$ was explored by single particle tracking with $^{AT647N}mLCF_{PEG2k}$ micro-injected at low concentrations.

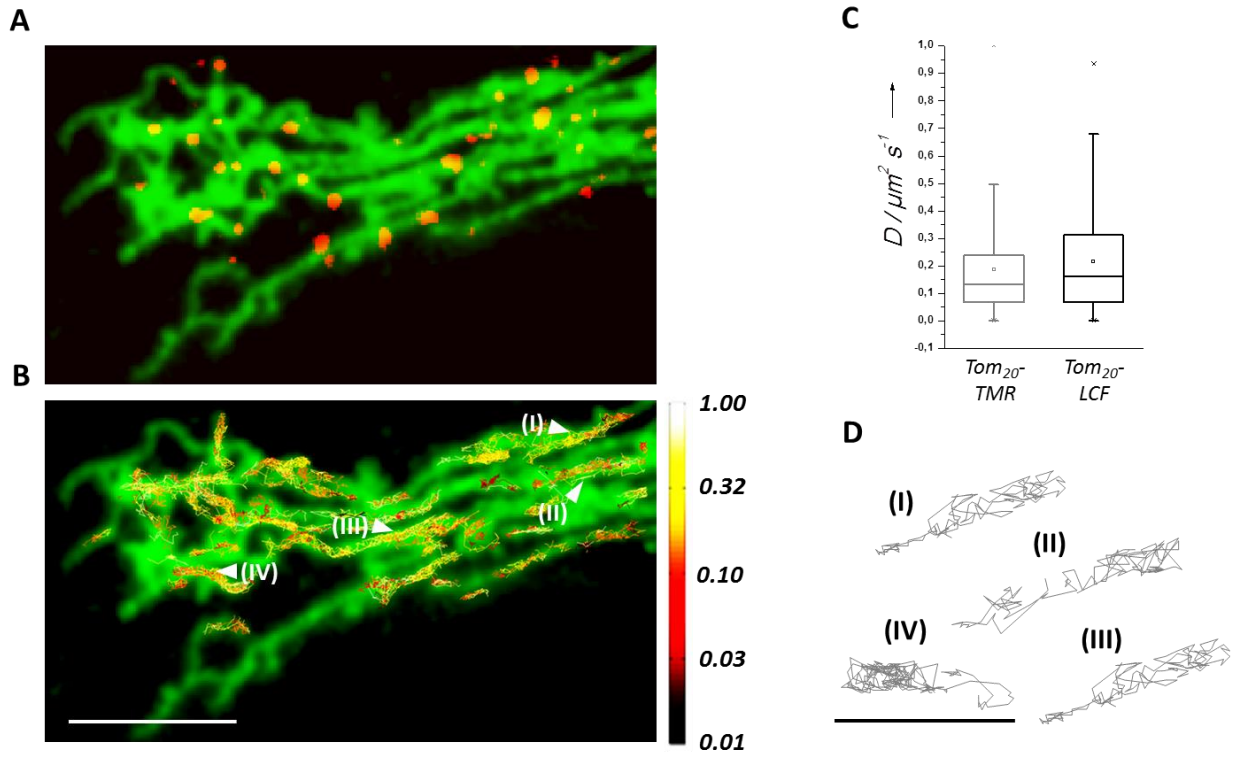

Figure III.10 Tracking of single $^{AT647N}mLCF_{PEG2k}$ bound to Tom20. (A) Overlay image of single $^{AT647N}mLCF_{PEG2k}$ molecules bound to Tom20. (B) Corresponding TALM image of 500 frames overlaid with Tom20 fluorescence. Color bar represent the diffusion velocity / µm² s⁻¹. The scale bar corresponds to 5 µm. (C) Average diffusion constants obtained for Tom20 labeled by TMR (left) or $^{AT647N}mLCF_{PEG2k}$ (right). (D) Representative trajectories were analyzed for transient confinement zones. The scale bar corresponds to 2 µm.

Individual particles were discerned which specifically co-localized with mitochondria over extended time periods without significant photo bleaching (Figure III.10 A and Video 6). Single particles could be tracked over several hundred frames and yielded trajectories which followed the shape of mitochondria (Figure III.10 B). Resulting trajectories yielded an average diffusion constant of 0.16 µm^2 s^{-1} (Figure III.10 C), which is in excellent agreement with the average diffusion constant of 0.14 µm^2 s^{-1} obtained for Tom_{20}::mEGFP::HaloTag labeled by ^{TMR}HTL.[1]

Moreover, single trajectory analysis revealed homogeneous diffusion over longer time periods up to 300 frames (Figure III.9 D). Thus, unbiased tracking of individual proteins in intracellular membranes could be successfully achieved by labeling with $^{AT647N}mLCF_{PEG2k}$.

13 Summary & Conclusion

Mono-functional nanoparticles exhibiting intracellular stealth properties are essential for long term and quantitative single molecule studies inside living cells. The major aspect of this chapter was to engineer indifferent nanoparticles exhibiting stealth properties in the cytoplasm of living cells. Based on the protein light chain ferritin, we engineered a highly biocompatible model nanoparticle for specific and quantitative application inside living cells. However, LCF tended to aggregate inside HeLa cells on a time scale of seconds. Co-localization of these aggregates with mEGFP::LC3 indicated that the specific recognition by the autophagy machinery was responsible for rapid clustering of LCF. Nanoparticle aggregation in the cytosol has been reported previously.[17-21] Rather than non-specific FNP aggregation, nanoparticle recognition by an active machinery could be the key mechanism for clustering of NPs inside living cells. This could be caused by the formation of a specific protein corona around the NPs. To address this questions and since the identity of NPs is determined by their size, shape, as well as their surface charge and hydrophobicity,[31,32] different LCF surface modifications were investigated in order to minimize LCF degradation. Similar to preventing macrophage-uptake of synthetic nanoparticles in organisms,[33] dense surface PEGylation substantially reduced nanoparticle recognition by the autophagy machinery. In comparison with the cytosolic clustering of PEGylated quantum dots[17,18] , our results indicated that high PEGylation densities are necessary (1 chain / 2.3 nm^2) in order to prevent unspecific interaction of nanoparticles in the cytosol of living cells. In combination with the unbiased intracellular diffusion of LCF_{PEG2k}, cytosolic stealth properties with respect to metabolic degradation and diffusion were achieved. Stealth FNPs are a key prerequisites for unbiased single molecule studies by minimizing repulsive or attractive interactions of the FNPs with the cellular environment. In combination with mono-functionalization of LCF with an improved clickHTL based on an efficient purification strategy, selective and robust labeling of proteins within the cytoplasm was possible, which is particularly

important in intracellular applications. Even mono-functionalized FNPs could rapidly and efficiently targeted to intracellular proteins. Upon fulfilling all these requirements, unbiased diffusion dynamics of a membrane protein within the outer mitochondrial membrane were observed despite of attaching a ~16 nm sized particle. As shown in Chapter II, the physicochemical properties of the NPs were thought to be the key determinants for their unbiased intracellular application. The successful reduction of unspecific intermolecular interactions demonstrated that the surface properties of the nanoparticles rather than the size are the critical determinants for their cytosolic applications. Extension of these approaches to other types of FNPs can be envisaged, including those containing electron-dense cores suitable for correlative light and electron microscopy.

14 References

1. Appelhans, T. et al. Nanoscale organization of mitochondrial microcompartments revealed by combining tracking and localization microscopy. *Nano Lett* **12**, 610-6 (2012).
2. Claridge, S.A., Liang, H.W., Basu, S.R., Frechet, J.M. & Alivisatos, A.P. Isolation of discrete nanoparticle-DNA conjugates for plasmonic applications. *Nano Lett* **8**, 1202-6 (2008).
3. Clarke, S., Tamang, S., Reiss, P. & Dahan, M. A simple and general route for monofunctionalization of fluorescent and magnetic nanoparticles using peptides. *Nanotechnology* **22**, 175103 (2011).
4. Li, F. et al. Monofunctionalization of protein nanocages. *J Am Chem Soc* **133**, 20040-3 (2011).
5. You, C. et al. Self-controlled monofunctionalization of quantum dots for multiplexed protein tracking in live cells. *Angew Chem Int Ed Engl* **49**, 4108-12 (2010).
6. You, C. et al. Electrostatically controlled quantum dot monofunctionalization for interrogating the dynamics of protein complexes in living cells. *ACS Chem Biol* **8**, 320-6 (2013).
7. Gref, R. et al. 'Stealth' corona-core nanoparticles surface modified by polyethylene glycol (PEG): influences of the corona (PEG chain length and surface density) and of the core composition on phagocytic uptake and plasma protein adsorption. *Colloids Surf B Biointerfaces* **18**, 301-313 (2000).
8. Amoozgar, Z. & Yeo, Y. Recent advances in stealth coating of nanoparticle drug delivery systems. *Wiley Interdiscip Rev Nanomed Nanobiotechnol* **4**, 219-33 (2012).
9. Crichton, R.R. & Declercq, J.P. X-ray structures of ferritins and related proteins. *Biochim Biophys Acta* **1800**, 706-18 (2010).
10. Lin, X. et al. Chimeric ferritin nanocages for multiple function loading and multimodal imaging. *Nano Lett* **11**, 814-9 (2011).
11. Lee, S., Lee, K.H., Ha, J.S., Lee, S.G. & Kim, T.K. Small-molecule-based nanoassemblies as inducible nanoprobes for monitoring dynamic molecular interactions inside live cells. *Angew Chem Int Ed Engl* **50**, 8709-13 (2011).
12. GE-Healthcare. Ion Exchange Chromatography & Chromatofocusing. *Handbooks from GE Healthcare*.
13. Verkman, A.S. Solute and macromolecule diffusion in cellular aqueous compartments. *Trends Biochem Sci* **27**, 27-33 (2002).
14. Müller, C.B. et al. Precise measurement of diffusion by multi-color dual-focus fluorescence correlation spectroscopy. *EPL (Europhysics Letters)* **83**
15. Sternberg, S.R. Biomedical Image Processing. Vol. 16 22-34 (1983).
16. Nel, A.E. et al. Understanding biophysicochemical interactions at the nano-bio interface. *Nat Mater* **8**, 543-57 (2009).
17. Muro, E. et al. Comparing intracellular stability and targeting of sulfobetaine quantum dots with other surface chemistries in live cells. *Small* **8**, 1029-37 (2012).
18. Xu, J. et al. Nanoblade delivery and incorporation of quantum dot conjugates into tubulin networks in live cells. *Nano Lett* **12**, 5669-72 (2012).

19. Biju, V., Itoh, T. & Ishikawa, M. Delivering quantum dots to cells: bioconjugated quantum dots for targeted and nonspecific extracellular and intracellular imaging. *Chem Soc Rev* **39**, 3031-56 (2010).

20. Delehanty, J.B., Mattoussi, H. & Medintz, I.L. Delivering quantum dots into cells: strategies, progress and remaining issues. *Anal Bioanal Chem* **393**, 1091-105 (2009).

21. Smith, A.M. & Nie, S. Next-generation quantum dots. *nature biotechnology* **27**(2009).

22. Kabeya, Y. et al. LC3, GABARAP and GATE16 localize to autophagosomal membrane depending on form-II formation. *J Cell Sci* **117**, 2805-12 (2004).

23. Pankiv, S. et al. p62/SQSTM1 binds directly to Atg8/LC3 to facilitate degradation of ubiquitinated protein aggregates by autophagy. *J Biol Chem* **282**, 24131-45 (2007).

24. Verwey, E.J.W. & Overbeek, J.T.G. Theory of the Stability of Lyophobic Colloids. *Elsevier, Amsterdam* (1948).

25. Deryaguin, B.V. & Landau, L.D. A theory of the stability of strongly charged lyophobic sols and of the adhesion of strongly charged particles in solutions of electrolytes. *Acta Physicochim. USSR* **14**(1941).

26. Benhabbour, S.R., Sheardown, H. & Adronov, A. Cell adhesion and proliferation on hydrophilic dendritically modified surfaces. *Biomaterials* **29**, 4177-86 (2008).

27. Seksek, O., Biwersi, J. & Verkman, A.S. Translational diffusion of macromolecule-sized solutes in cytoplasm and nucleus. *J Cell Biol* **138**, 131-42 (1997).

28. Wachsmuth, M., Waldeck, W. & Langowski, J. Anomalous diffusion of fluorescent probes inside living cell nuclei investigated by spatially-resolved fluorescence correlation spectroscopy. *J Mol Biol* **298**, 677-89 (2000).

29. Kudchodkar, S.B. & Levine, B. Viruses and autophagy. *Rev Med Virol* **19**, 359-78 (2009).

30. Kang, S. et al. Controlled assembly of bifunctional chimeric protein cages and composition analysis using noncovalent mass spectrometry. *J Am Chem Soc* **130**, 16527-9 (2008).

31. Monopoli, M.P., Aberg, C., Salvati, A. & Dawson, K.A. Biomolecular coronas provide the biological identity of nanosized materials. *Nat Nanotechnol* **7**, 779-86 (2012).

32. Monopoli, M.P. et al. Physical-chemical aspects of protein corona: relevance to in vitro and in vivo biological impacts of nanoparticles. *J Am Chem Soc* **133**, 2525-34 (2011).

33. Perry, J.L. et al. PEGylated PRINT nanoparticles: the impact of PEG density on protein binding, macrophage association, biodistribution, and pharmacokinetics. *Nano Lett* **12**, 5304-10 (2012).

IV Manipulation and probing of protein activities

This work was done in close cooperation with Fred Etoc and Mathieu Coppey in the lab of Maxime Dahan (CNRS Paris/France).

15 Introduction

The spatiotemporal regulation of protein activity, as well as their heterogenous distribution play a key role in the control and the maintainance of cellular functions.[1,2] The previous chapters introduced advanced methods for the observation of proteins. As demonstrated, mono-functional stealth FNPs allowed unbiased tracking of individual membrane proteins inside living cells. Besides the exploration of protein dynamics, generic approaches for intracellular manipulation and probing of protein activities are desired.

Several approaches have been developed for exploring protein function by directed manipulation of their activity pattern at a subcellular scale. Photoactivatable reagents[3,4] and optogenetic approaches[5,6] have been shown to be powerful tools for the local control of protein activity inside living cells. Maintaining a spatial activation pattern over extended time periods, however, remains challenging due to diffusional spreading of photoactivated proteins. Furthermore, several methods for quantification of protein activities in the cytoplasm of living cells by determining the rate constants of their interaction have been described. Yet these appoaches, mainly based on Förster resonance energy transfer (FRET)[7,8] and fluorescence recovery after photo bleaching (FRAP),[9,10] are often highly specialized or complicated to evaluate. In addition, these methods fail to probe protein-protein interaction with high spatial resolution.

On these grounds, nanoparticles applicable as well-defined and controllable platforms that can be spatially and accurately positioned inside living cells are desired. Magnetic nanoparticles (MNPs) have long been used to investigate the cell response to mechanical perturbations.[11-14] They have emerged as efficient actuators to remotely trigger cellular signaling, either by inducing membrane receptor clustering[15] or by activating temperature-sensitive channels.[16] Only recently, bioactive MNPs have been used to engineer signaling networks and spatial self-organization inside living cells.[17]

In this chapter, we extended the application of MNPs towards magnetogenetic manipulation, i.e. by bio-functionalized MNPs (bfMNPs) self-assembled into active intracellular signaling platforms. The nanoparticles act as nanoscopic hot spots, which allow either to trigger signal transduction that leads to a cell response after displacement of MNPs by magnetic forces or to probe protein-protein interactions on the MNP surface. To this end, small GTPases of the Rho family were employed as model proteins.[18,19] A procedure was established to spatially manipulate MNPs in the cytoplasm of living cells. Remodeling of the actin cytoskeleton at sub-cellular scale was studied by manipulation of endogenous Rac1 activity mediated by MNPs functionalized with a guanine-nucleotide exchange factor (GEF). In this approach, the HaloTag technology was utilized in order to bio-functionalize clickHTL functionalized MNPs (^{clickHTL}MNPs) in the cytoplasm of living cells. As add on, MNPs were utilized as defined nano-platform in order to quantify the interaction of Cdc42 functionalized MNPs with overexpressed N-WASP *in cellulo*.

16 Materials and Methods

16.1 Materials

Streptavidin coated magnetic-nanoparticles (MasterBeads, ~500 nm in diameter) were purchased from Ademtech, (Pessac/France). Dibenzylcyclooctyne-(ethylen glycole)$_4$-biotin (DBCO-EG$_4$-biotin) was purchased from Click Chemistry Tools (Scottsdale/USA). UHU^{EXTRA} Alleskleber glue was purchased from EDEKA (Osnabrück/Germany). pmEGFP-Rac1 and pTIAM^{DHPH} were obtained from Christian Hermann. Other chemicals were purchased from Sigma Aldrich.

16.2 Molecular biology

GST::Cdc42^{Q61L} (pGEX-TEV::AP::Cdc42Q61L), GST::cdc42^{T17N} (pGEX-TEV::AP::Cdc42T17N) and GST::GBD-NWASP (pGEX-2T-GBD(NWASP)) for prokaryotic expression: Full-length Cdc42 wild-type and mutants were produced as GST fusion proteins as describe elsewhere.[20] pGEX-2T-GBD-NWASP was produced by Moritz Warntjen.

Cloning of TIAM^{DHPH} (aa 1033-1406) fused to mCherry and the HaloTag (pSems-TIAM::mCherry::HaloTag) for eukaryotic expression: pSems-TIAM::mCherry::HaloTag was

generated by cassette cloning as described in Chaper II (Section 2.2). The SNAP-Tag of pSems-Snap-1-26m was substituted for mCherry after restriction with *Nhe*I and *Xho*I. HaloTag7 was amplified by PCR from pFC17A-HaloTag and inserted into pSems-mEGFP restricted by *Xho*I and *Not*I, resulting into a 42 base pair spacer between mCherry and HaloTag. TIAM^{DHPH} was amplified by PCR from pTiam^{DHPH} and inserted in pSems-mCherry::HaloTag restricted by *EcoR*V and *EcoR*I.

All cloning steps were performed according to manufacturer's instructions.

16.3 Protein biochemistry

Expression, purification and biotinylation of ^{BT}Cdc42^{Q61L} and ^{BT}Cdc42^{T17N}: For preparative protein expression *E. coli* Rossetta (Novagen) were transformed with pGEX-TEV::AP::Cdc42^{Q61L} or pGEX-TEV::AP::Cdc42^{T17N}. Expression was induced with 0.5 mM IPTG at OD_{600}: 0.6-0.8. Expressing cells were grown for 4 h at 37 °C. Harvested cells were resuspended in PBS, pH 7.4 supplemented with lysozyme and protease inhibitors. Cell lysate obtained from 1 L *E. coli* culture was loaded onto 1.5 ml glutathione agarose beads (GE Healthcare), washed with PBS, pH 7.4 and biotinylated for 2 h at room temperature in PBS, pH 7.4 containing 5 mM $MgCl_2$, 1 mM biotin, 1 mM ATP and 500 nM biotin ligase (BirA). After washing the beads with PBS pH 7.4 twice, Cdc42 was cleaved from the beads in 20 mM HEPES, 150 mM NaCl, pH 7.4 containing 0.5 mM EDTA, 1 mM DTT and 50 nM TEV-protease. Finally, the proteins were purified to homogeneity by size exclusion chromatography (Superdex 75 10/300, GE Healthcare). Purity was confirmed by SDS-PAGE MW (^{BT}Cdc42^{Q61L} and ^{BT}Cdc42^{T17N}): ~22 kDa;.

Expression, purification and labeling of GST::GBD-NWASP: Expression of this protein was carried out as described above. Cell lysate obtained from 1 L *E. coli* culture was loaded onto 1.5 ml glutathione agarose beads (GE Healthcare). After washing with PBS, pH 7.4 thrice, GST-GBD was eluted with 10 mM gluthatione and purified to homogeneity by SEC in HBS, pH 7.4 (Superdex 75 10/300). Subsequently, 500 µl (20 µM) of the resulting protein solution was incubated with 1.5 fold excess of Alexa Fluor 488 maleimide for 1.5 h at room temperature. The excess of unbound dye was removed by SEC (Superdex 75 10/300) and the degree of labeling was estimated by UV/VIS spectrometry. Purity was confirmed by SDS-PAGE MW(GST::GBD-NWASP): ~36 kDa.

All chromatography steps were performed using a FPLC system (Äkta Explorer, GE Healthcare) according to standard protocols.

Analytical size-exclusion chromatography (aSEC): In order to confirm $^{BT}Cdc42^{Q61L}$ biotinylation, 2 µM $^{BT}Cdc42^{Q61L}$ was incubated with increasing concentration of streptavidin in 20 µl HBS, pH 7.4. The mixture was loaded onto a SEC column (Superdex 200 5/150) equilibrated with HBS, pH 7.4. Chromatography steps were performed using a HPLC system (Jasco) and elution was monitored by a spectral diode array detector (MD-2015 plus, Jasco)

16.4 Bio-conjugation chemistry

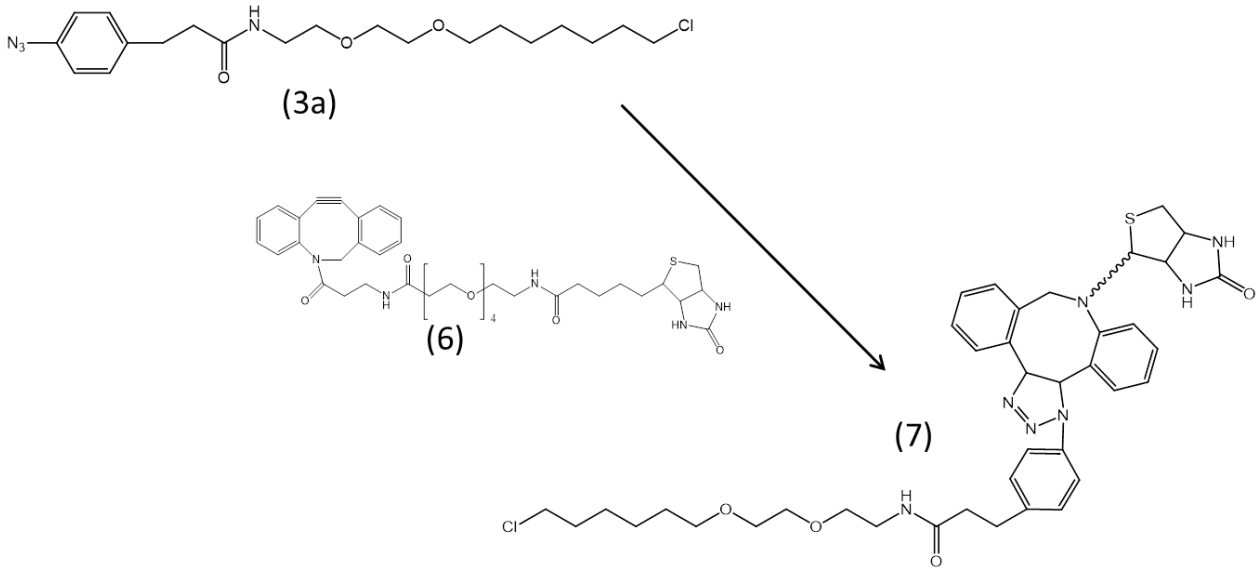

Scheme IV.1 Synthesis of ^{biotin}clickHTL.

Synthesis of ^{biotin}clickHTL (7): 20 µl **(3a)** (200 mM) and 20 µl Dibenzylcyclooctyne-EG$_4$-biotin **(4)** (200 mM) in 20 mM HEPES, pH 8.0 containing 66% DMF were incubated at room temperature for 2 h. After removal of the solvent *in vacuo*, the residue was dissolved in 30% acetonitrile, 0.1% TFA. The product was purified by reversed-phase chromatography on a Vydac TP C18 column (Grace) using isocratic elution. Chromatography was performed using a HPLC system (Jasco). ESI-MS *m/z* 1121.4 [M^{+1}]; calc. 1120.5

16.5 Nanoparticle functionalization

Coupling of $^{BT}Cdc42^{Q61L}$ and $^{BT}Cdc42^{T17N}$: 10 µl streptavidin coated magnetic-nanoparticles (^{SAV}MNPs, 500 pM) in PBS, pH 7.4 and 10 µl $^{BT}Cdc42^{Q61L}$ or $^{BT}Cdc42^{T17N}$ (both 1 µM) in PBS, pH 7.4 were mixed and incubated at room temperature for 30 min. Subsequently, 100 nM ATTO

647N-biotin in PBS, pH 7.4 was added to the mixture and allowed to react at room temperature for additional 30 min. ^{AT647N}MNPs^{Cdc42Q61L} and ^{AT647N}MNPs^{Cdc42T17N} were purified by washing with PBS, pH 7.4 thrice after pelletization using a permanent magnet. Finally, these MNPs were resuspended in 40 µl PBS, pH 7.4 and briefly sonicated.

Coupling of ^{biotin}clickHTL (7): 10 µl ^{SAV}MNPs (500 pM) in PBS, pH 7.4 and 10 µl ^{biotin}clickHTL (10 µM) in PBS, pH 7.4 were mixed and incubated at room temperature for 30 min. Purification of ^{clickHTL}MNPs was carried out as described above.

16.6 Solid surface based binding assay

Surface modification for interaction assays *in vitro:* Surface chemistry was carried as described in Chapter II (Section 5.6). After surface cleaning in fresh Piranha solution (one part H_2O_2 30 % and two parts concentrated H_2SO_4) the surface was activated with pure (3-Glycidyloxypropyl)trimethoxysilane for 1 h at 75 °C. Subsequently, the surface was incubated with diamino-PEG MW: 2000 Da for 4 h at 75 °C. For immobilization of GST::GBD-NWASP via cysteine residues, these surfaces were activated with 3-(Maleimido)propionic acid N-Hydroxy-succinimide ester (MPA-NHS), as described elsewhere.[21]

Interaction assays by real-time solid phase detection: Real-time surface binding assays were carried out by reflectance interference (RIf) using a home-built set-up, which has been described in Chapter II (Section 5.6). For probing the reaction of Cdc42 with its effector, GST::GBD-NWASP was covalently immobilized via cysteine residues on a PEG polymer brush activated with MPA-NHS. Subsequently, increasing concentrations of ^{BT}Cdc42^{Q61L} were injected and binding was monitored in real-time by RIf. The resulting binding curves were fitted using a model for pseudo first-order reactions using Bia-evaluation software. Binding experiments were performed at room temperature, as well as at 37 °C.

16.7 Fluorescence microscopy

All cell experiments were performed at 37 °C.

Epi-imaging: Ensemble fluorescence imaging was performed in a EPI fluorescence microscope (Olympus IX71) equipped with a X-Cite Series 120 light (Lot-Oiel, France) source and a EMCCD Evolve 512 (Photometrics, USA).

Fluorecence recovery after photobleaching (FRAP): Protein-protein interactions on the surface of MNPs were probed by FRAP. In these experiments, a 405 nm laser line at full power was used, which was controlled by a FRAP head (Roper Scientifics, France) and allowed to bleach an area of 5 μm^2 pixel around the 500 nm MNP. After photo bleaching, fluorescence recovery was monitored.

Förster resonance energy transfer (FRET): Activation of Rac1 at the plasma membrane was probed using a FRET based biosensor (RaichRac1) as described in detail previously.[22] For this experiment, a dual view beamsplitter was used, which allowed to separate the emitted light of CFP (donor) and YFP (acceptor). The resulting fluorescent images were evaluated using the Biosensor Processing Software 2.1 to obtain fluorescence ratio images.[18]

16.8 Cell biology

3T3 Fibroblasts and COS7 cells were cultivated at 37°C, 5% CO_2 in MEM supplemented with 10% fetal calf serum (MEM/FCS) and 1% NEAA without addition of antibiotics. Transfection was carried out using Fugene 6 (Roche) according to the manufactures instructions.

16.9 Magnetic tweezer fabrication

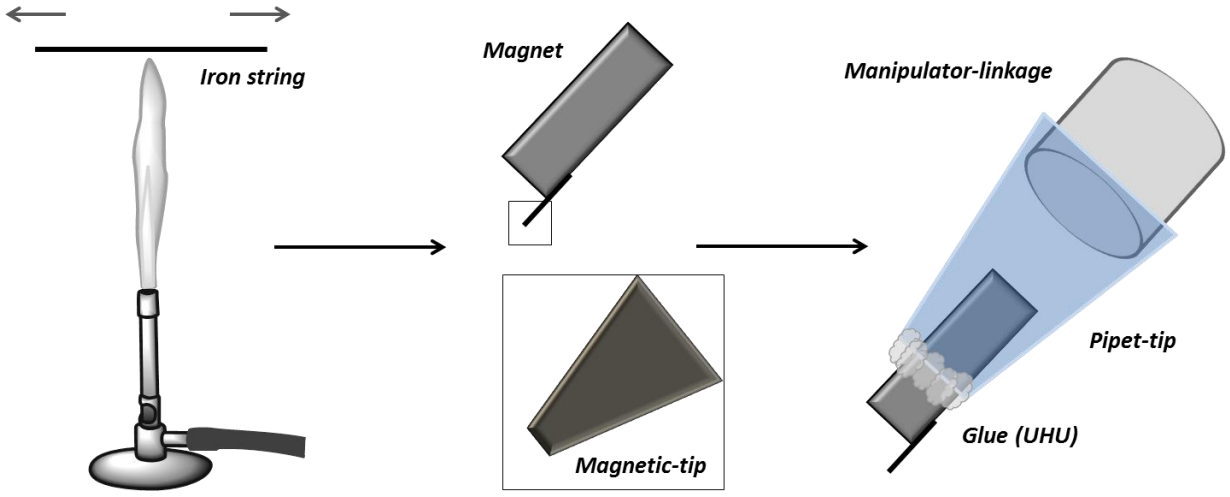

Scheme IV.2 Magnetic tweezers fabrication.

Magnetic tweezers fabrication was carried out as described in detail elsewhere.[23] Home-built magnetic tweezer were made by gently pulling an iron string (150 µm in diameter) at the top of a flame. The resulting tip (~20 µm in diameter) was placed on top of a parallelepiped permanent magnet (4 x 1 x 0.5 mm) made of NdFeB. For accurate control of the tip, the

magnetic tweezers was mounted to a micromanipulation system (Eppendorf) using a pipet-tip as joined.

17 Results and discussion

17.1 Magnetic manipulation of MNPs in the cytoplasm of living cells

Magnetogenetic manipulation comprises genetically encoded targeting of specific proteins in combination with magnetic nano-manipulation. To this end, we first established a robust approach to accurately manipulate MNPs in the cytoplasm of living cells. Therefore, we microinjected super-paramagnetic nanoparticles into 3T3 fibroblasts.

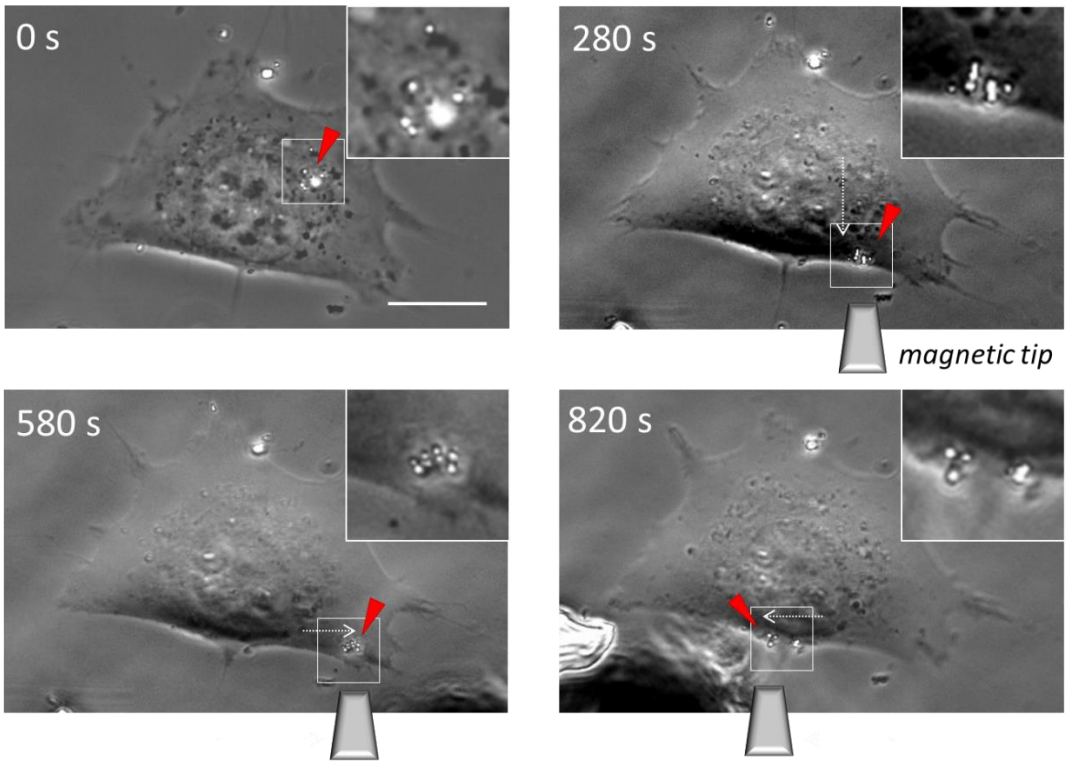

Figure IV.1 Intracellular manipulation of 500 nm MNPs inside 3T3 fibroblast. MNPs appear as bright and white dot in phase contrast images. The scale bar corresponds to 10 µm.

Upon applying magnetic forces (up to 30 pN) using a magnetic tip, MNPs translocated to the border of the cell within a few minutes (Figure IV.1, Video 7). Subsequently, shifting of the magnetic tip to the right and to the left, respectively, allowed spatial and accurate displacement of MNPs. On removing the magnetic tip, the particles diffused back towards the cell interior. This result suggested that spatial and accurate manipulation of MNPs was possible inside living

cells. However, in ~60 % of cases, the MNPs remained immobile, suggesting that the MNPs were probably trapped in the dense cytoskeleton meshwork. In order to optimize this approach, the viscoelastic properties of the MNP micro-environment were investigated in different cells by means of single-molecule microrheology techniques.[24,25] These results revealed that the elastic modulus of COS7 cells and serum starved 3T3 fibroblast was substantially reduced (~10 fold). compared to non-treated 3T3 fibroblasts. Their elastic modulus was sufficiently low so that more than 80% of the MNPs could be reproducibly displaced across the entire cell.

17.2 Bio-functionalization of ^{clickHTL}MNPs *in cellulo*

Since the purification of large proteins and protein-complexes, respectively, is often highly challenging and time consuming, we aimed to bio-functionalize MNPs directly in the cytoplasm of living cells using the HaloTag technology. To this end, streptavidin coated MNPs capable to bind ~1.000 biotinylated antibodies / MNP) were functionalized with biotinylated clickHTL **(7)** *in vitro.* Efficient binding of the HaloTag to ^{clickHTL}MNPs was probed using mCherry fused to the HaloTag (mCherry::HaloTag) as a model protein (Figure IV.2 A).

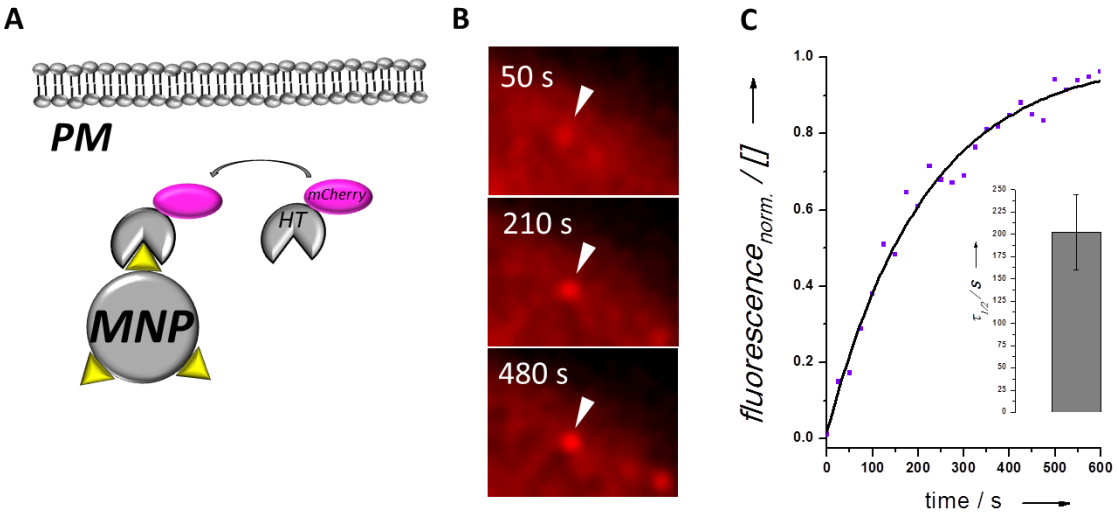

Figure IV.2 Bio-functionalization of MNPs in cellulo. (A) Schematic illustration of MNP bio-functionalization inside living cells. PM = plasmamembrane; HT = HaloTag (B) Time-lapse images of mCherry::HaloTag binding to ^{clickHTL}MNP. The white arrow depicts the location of the MNP. (C) Kinetics of MNP bio-functionalization. Fluorescence intensities were corrected for the cell background surrounding the particles.

After micro-injection of ^{clickHTL}MNPs into COS7 cells expressing HaloTag::mCherry, time lapse imaging revealed rapid binding of HaloTag::mCherry to ^{clickHTL}MNPs (Figure IV.2 B, Video 8). By quantifying the fluorescence increase on the surface of MNPs (Figure IV.2 C) a functionalization time of $\tau_{1/2} \approx 202 \pm 42$ s was obtained. Control experiments (data not shown) using particles without clickHTL showed no enhanced fluorescence at the particle location. These results confirmed efficient targeting of HaloTag fusion proteins to MNPs.

17.3 Recruitment of mEGFP::Rac1 to the surface of ^{TIAM}MNPs

In our magnetogenetic approach, bio-functionalized MNPs were expected to self-assemble into active signaling platforms triggered by the surface-tethered protein. This signaling platform is further thought to propagate a signal to cellular functions by locally activating a pool of endogenous proteins. In order to confirm this concept, as a first step we probed the interaction of TIAM with Rac1 at the plasma membrane inside living cells (Figure IV.3 A). TIAM is a specific guanine nucleotide exchange factor (GEF) activating Rac1, known to induce strong morphological changes upon activation (Figure IV.3 B).[5]

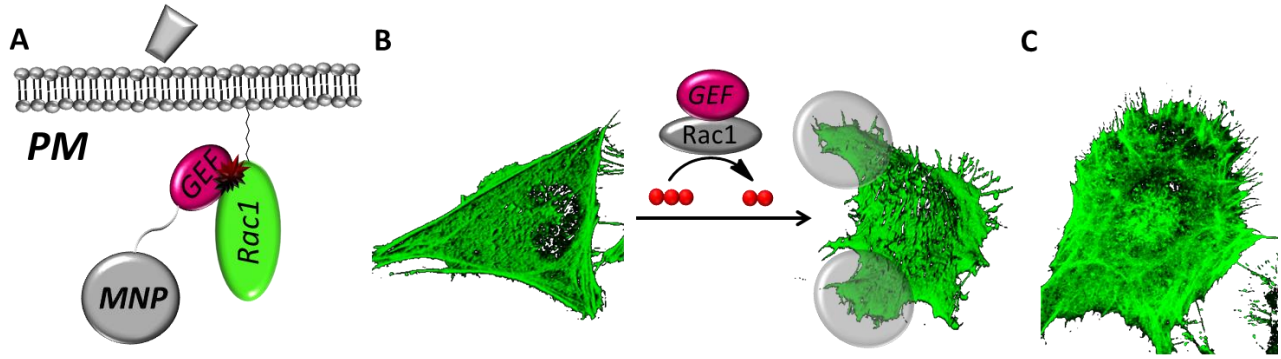

Figure IV.3 Manipulation of Rac1 activity inside living cells. (A) Schematic illustration of Rac1 recruitment by ^{TIAM}MNPs at the plasma membrane. (B) Illustration: Activation of Rac1 by a guanine nucleotide exchange factor (GEF) causes the formation of protrusions (grey cycles). (C) Illustration: GEF overexpression leads to strong phenotypes.

Full-length TIAM causes a strong phenotype when overexpressed (Figure IV.3 C). For this reason, only the catalytic domain of TIAM (TIAM^{DHPH}, aa 1033 – 1406) was fused to mCherry and the HaloTag (TIAM::mCherry::HaloTag). This truncated domain lacks the ability of the full-length protein to localize to the plasma membrane and consequently does not lead to any signaling activity.[26] After micro-injection of ^{clickHTL}MNPs into COS7 cells co-expressing mEGFP::Rac1 and

TIAM::mCherry::HaloTag, as expected no co-localization of TIAM functionalized MNPs (^{TIAM}MNPs), localized in the cytoplasm, with mEGFP::Rac1 was observed (Figure IV.4 A).

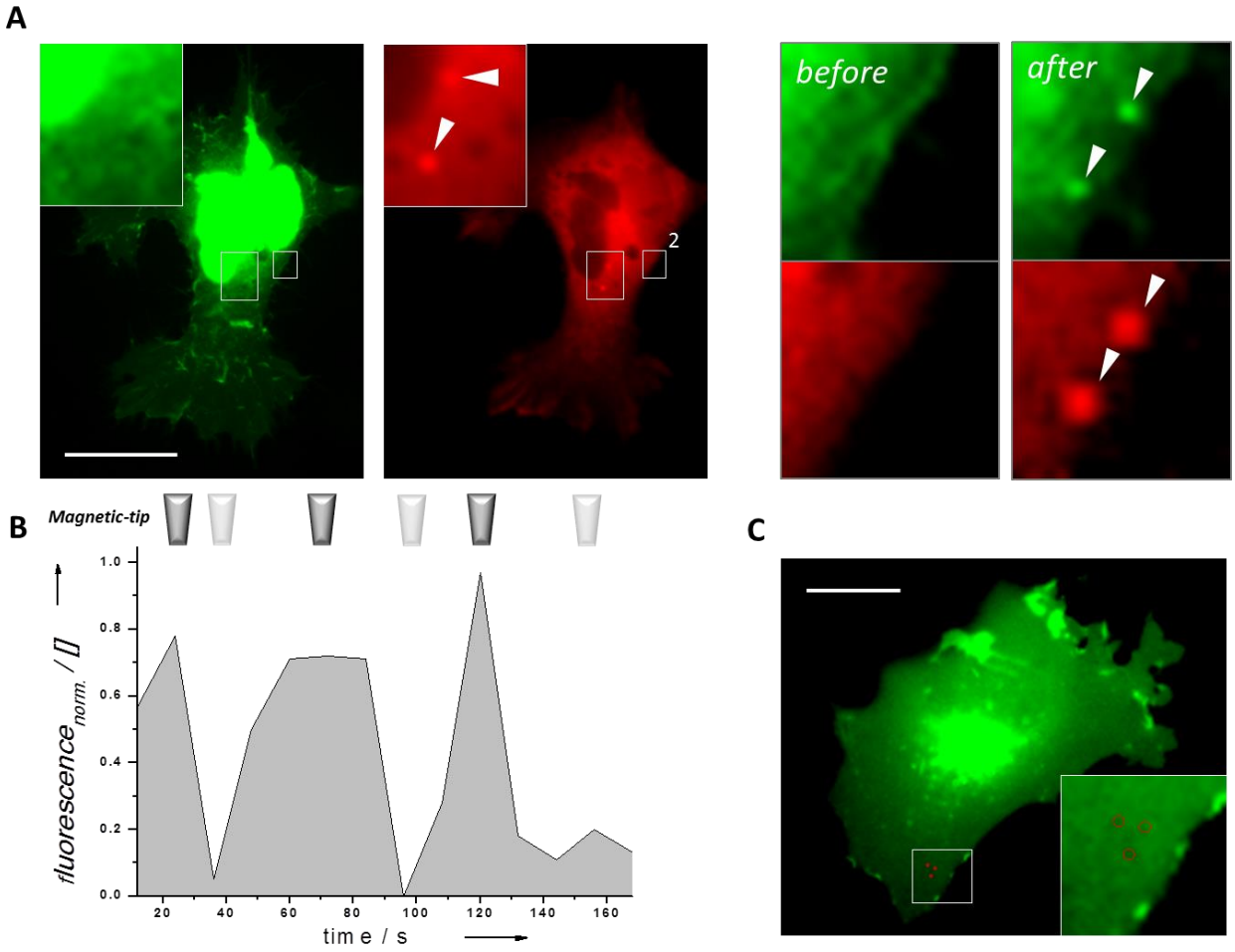

Figure IV.4 Recruitment of Rac1 to the plasma membrane. (A) Left: EPI-images of COS7 cells co-expressing mEGFP::Rac1 and TIAM::mCherry::HaloTag after micro-injection of ^{clickHTL}MNPs. The location of MNPs is indicted by the rectangle. Right: Crop of rectangle(2) before and after applying of magnetic forces (green: mEGFP::Rac1 channel; red: TIAM::mCherry::HaloTag). (B) Magnetic remote control of Rac1 recruitment at the plasma membrane in the presence of the magnetic-tip (grey) and in the absence (light gray). Fluorescence intensities were corrected for the background surrounding the particles. (C) COS7 cells expressing mEGFP::Rac1 upon micro-injection of solely streptavidin coated MNPs (^{SAV}MNPs) and application of magnetic forces. The scale bar corresponds to 10 µm in all images.

Upon application of magnetic forces, recruitment of mEGFP::Rac1 was observed at the plasma membrane as indicated by the bright dots (Figure IV.4 B). The recruitment of mEGFP::Rac1 was highly reversible, and interaction was abrogated when the particles diffused away from the

membrane upon removing the magnetic tip. In contrast, no co-localization could be observed after bringing solely ^{SAV}MNPs in contact with the membrane (Figure IV.4 C).

Subsequently, for probing Rac1 activation by recruitment of ^{TIAM}MNPs, Raichu-Rac1 was employed. Raichu-Rac1 is an intracellular FRET based biosensor of Rac1 activity (Figure IV.5 A).[22] This FRET reporter is composed of a membrane targeting sequence (CAAX) at the N-terminus, followed by YFP (acceptor), the Rac1 GTPase, a linker, a Rac1 GTPase binding domain (GBD) and CFP (donor). In its GDP-bound inactive form, YFP and CFP are located distal from each other. GEF-catalyzed activation of Rac1 induces the association of active GTP-bound Rac1 with the GBD. This intramolecular interaction brings CFP in close proximity to YFP and enables FRET. For investigating the catalytic activity of ^{TIAM}MNPs at the membrane, ^{clickHTL}MNPs were micro-injected into COS7 cells co-expressing TIAM::mCherry::HaloTag and Raichu-Rac1.

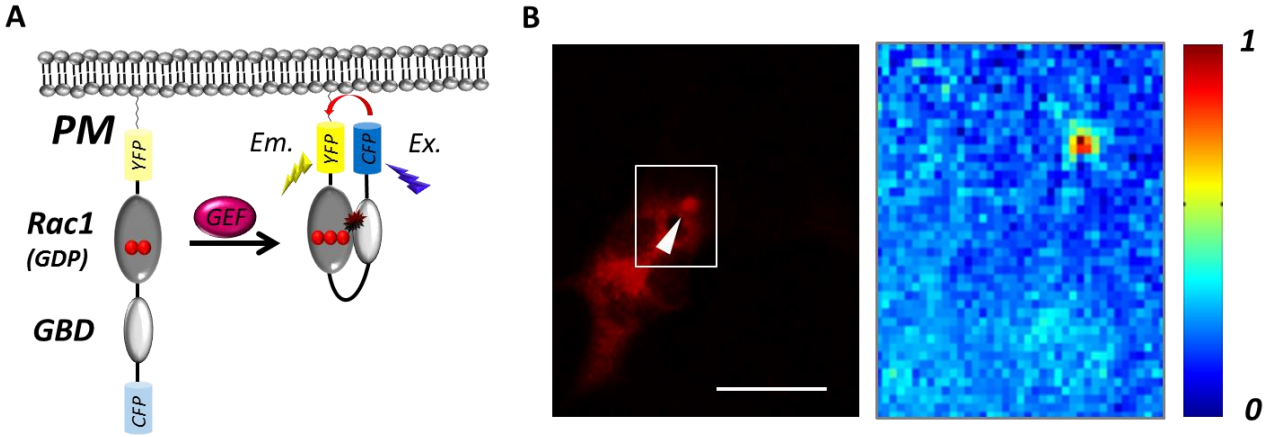

Figure IV.5 Probing Rac1 activation using Raichu-Rac1. (A) Schematic Illustration of Raichu-Rac1 before and after Rac1 activation. GBD: GTPase binding domain; CFP: cyan fluorescent protein; YFP: yellow fluorescent protein; Ex.: Excitation; Em.: Emission. (B) COS7 cells co-expressing TIAM::mCherry::HaloTag and Raichu-Rac1. Left: EPI-image after micro-injection of clickHTLMNPs. Particle location is indicated by the white arrow. Right: Crop of the rectangle, ratio image of Raichu-Rac1 in the presence of magnetic forces. Intensity bar: FRET efficiency was normalized to the basal FRET efficiency of Raichu-Rac1. The scale bar corresponds to 10 µm.

Increased FRET-signals co-localized with ^{TIAM}MNPs were observed in the presence of the magnetic tip (Figure IV.5 B), confirming that the ^{TIAM}MNPs were not only recruiting Rac1 but also actively catalyzing its activation when brought to the membrane.

17.4 Activation of endogenous Rac1 induced morphological changes

Given the successful recruitment and activation of Rac1 by ^{TIAM}MNPs, we next investigated the impact of endogenous Rac1 activation on actin polymerization as a function of the subcellular context (Figure IV.6 A and B). To this end, ^{clickHTL}MNPs were microinjected into COS7 cells co-expressing TIAM::mCherry::HaloTag and Lifeact::mEGFP. Lifeact::mEGFP was employed as sensitive fluorescent reporter to visualize the signaling perturbation caused by ^{TIAM}MNPs.

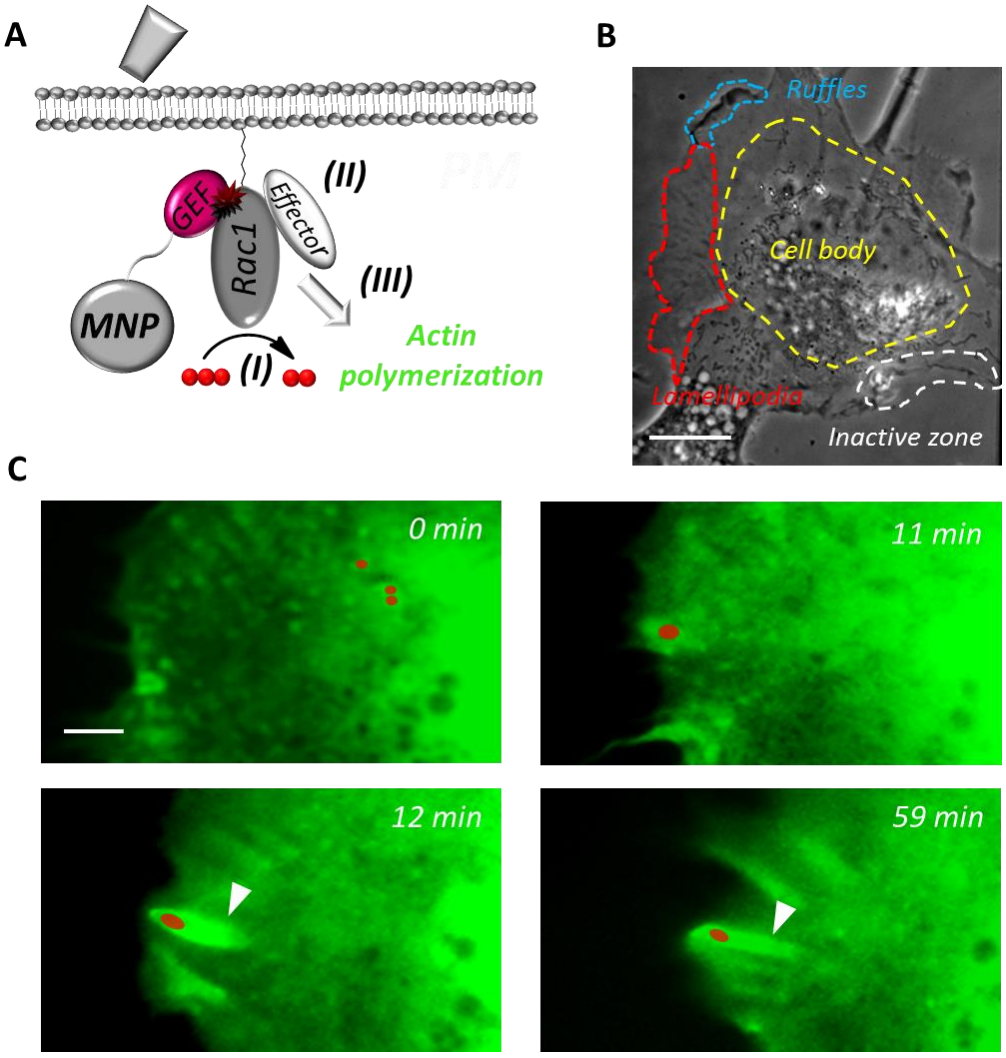

Figure IV.6 Magnetic manipulation of Rac1 activity in cellulo. (A) Schematic illustration of Rac1 activation by exchange of GDP for GTP (I), binding of an effector protein (II) and propagation of downstream signaling initiating actin polymerization (III). (B) COS7 cells divided in different areas of GTPase activities. The scale bar corresponds to 10 µm. (C) Magnetic manipulation of ^{TIAM}MNPs into lamellipodia. Formation of an actin cloud is indicated by the white arrow. The location of ^{TIAM}MNPs is indicated by the red dots. The scale bar corresponds to 1 µm.

By applying magnetic forces, ^{TIAM}MNPs were translocated into lamellipodia, protrusions with enhanced GTPase activities.[27] Within lamellipodia, strong actin polymerization in form of an actin cloud around the particles was observed (Figure IV.6 C). This actin cloud remained stable for more than 40 minutes by keeping the particle in position, and was subjected to the retrograde flow within the lamellipodia (Video 9). Interestingly, actin polymerization was only observed in protrusive areas. By contrast, wherever ^{TIAM}MNPs were brought to the plasma membrane, Rac1 activation was observed using the Raichu-Rac1 biosensor. These results indicated that the perturbation of Rac1 signaling was context-dependent. In order to confirm this observation, ^{TIAM}MNPs were translocated into an area with no membrane activity. Within a few minutes, actin polymerization started and the formation of a protrusion was observed. Consistent with the previous observation in lamellipodia, this was followed by the formation of an actin cloud (Figure IV.7).

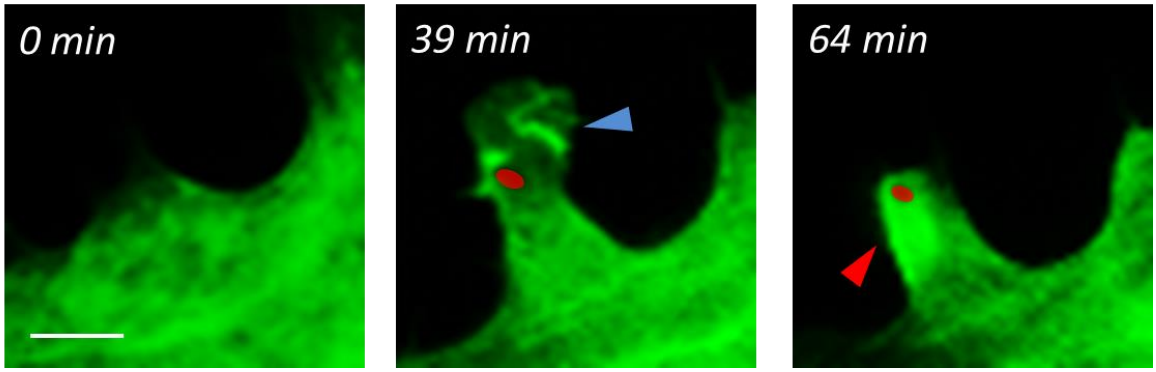

Figure IV.7 Magnetic manipulation of ^{TIAM}MNPs into an area with no membrane activity. The formation of a protrusion is indicated by the blue arrow and the actin cloud is indicated by the red arrow. The location of ^{TIAM}MNPs is indicated by the red dots. The scale bar corresponds to 1 µm.

In a control experiment using MNPs functionalized with solely mCherry::HaloTag, only the basal activity of the cell was observed (Video 10). This suggested that actin polymerization resulted from the perturbation of Rac1 signaling by ^{TIAM}MNPs and not from mechanical stimuli on the membrane caused by MNPs.

Together, these results demonstrated that MNPs can be employed as self-assembled nanoscopic signaling platforms for spatial and accurate manipulation of protein activities inside living cells. Furthermore, these experiments provide clear evidence that Rac1 signaling depents on the subcellular-context by spatial isolation of distinct signaling pathways.

17.5 Probing of protein-protein interaction on the surface of MNPs *in cellulo*

Beyond the application of MNPs in magnetogenetic approaches, these MNPs provide a well-defined platform for studying protein-protein interactions in the cytoplasm of living cells. For this purpose, MNPs are functionalized with a bait-protein of interest (bfMNPs) *in vitro*. Upon micro-injection of bfMNPs into cells overexpressing the fluorescently labeled prey-protein of choice, protein-protein interactions take place on the surface of the particles (Figure IV.8 A). Since protein-protein interactions are dynamic processes of continuous binding and unbinding events, this allows probing exchange rates using fluorescence recovery after photo bleaching (FRAP) (Figure IV.8 B). If dissociation is the rate limiting step ($k_{on}*c >> k_{off}$), the complex stability (k_{off}) can be directly fitted from the resulting fluorescence recovery curve using a mono-exponential model.

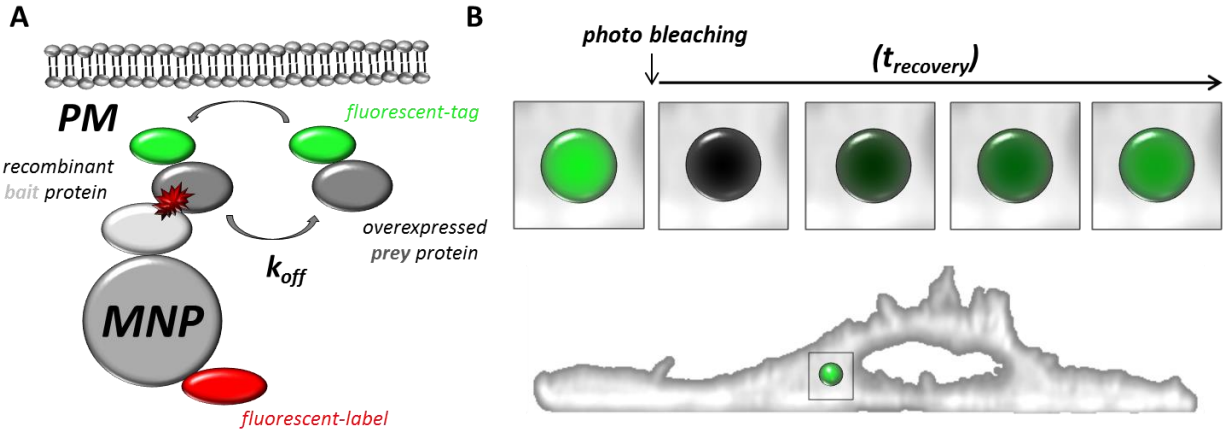

Figure IV.8 Schematic Illustration of bait-prey protein interactions probed by FRAP in cellulo. (A) Fluorescently labeled MNPs functionalized with a bait-protein of interest interacting with a prey-protein of choice labeled with a fluorescent-tag. (B) Schematic FRAP- experiment: After photo bleaching the fluorescence recovery on the particle surface is monitored over time.

In so doing, the interaction of Cdc42 and N-WASP was investigated inside living cells. To this end, we first probed binding of purified and constitutively active Cdc42 ($Cdc42^{Q61L}$) to the immobilized GTPase binding domain of N-WASP (GBD-NWASP) *in vitro*. The GBD was covalently immobilized on a maleimide-activated PEG polymer brush and binding was monitored in real-time after injection of $Cdc42^{Q61L}$ by RIf detection (Figure IV.9 A). Fitting of the resulting binding curve using a model for pseudo-first order reactions revealed an association rate constant $k_{on,\ in}$

vitro of 5.7 ± 0.5 * 10^5 M^{-1} s^{-1} and a dissociation rate constant of $k_{off,\ in\ vitro}$ of 0.08 ± 0.03 s^{-1} confirming that dissociation was the rate limiting step at concentration about 100 nM.

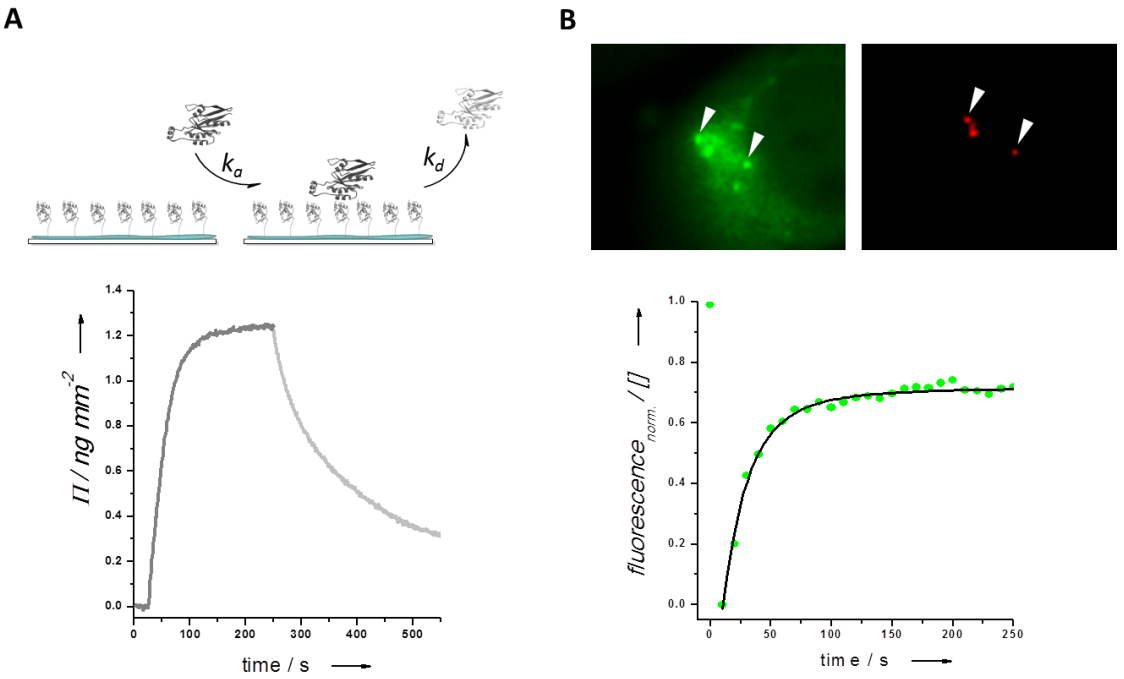

Figure IV.9 Probing the interaction of Cdc42 with GBD of N-WASP and N-WASP, respectively, in vitro and in cellulo. (A) Interaction of $Cdc42^{Q61L}$ with GBD in vitro monitored by RIf. (B) Interaction of $^{Cdc42Q61L}MNPs^{AT647N}$ with N-WASP::mEGFP overexpressed in COS7 cells. Top left: N-WASP::mEGFP channel, top right: $^{cdc42Q61L}MNPs^{AT647N}$ channel. Bottom: typical fluorescence recovery curve obtained from a photo bleaching experiment. Fluorescence intensities were corrected for the cell background.

Next, ^{SAV}MNPs (~500 nm in diameter) were functionalized *in vitro* with biotinylated, constitutively active Cdc42 ($^{BT}Cdc42^{Q61L}$) and labeled with ATTO 647N ($^{Cdc42Q61L}MNPs^{AT647N}$) for visualization. After micro-injection of $^{Cdc42Q61L}MNPs^{AT647N}$ into 3T3 fibroblasts overexpressing full-length N-WASP fused to mEGFP (N-WASP::mEGFP), N-WASP::mEGFP was recruited to the surface of MNPs on a time scale of a few seconds indicating that the concentration of N-WASP was sufficiently high. Bleaching of N-WASP::mEGFP co-localized with MNPs and fitting the resulting recovery curve revealed an exchange rate constant $k_{off,\ in\ cellulo}$ of 0.04 ± 0.01 s^{-1} (Figure IV.9 B and Video 11). This dissociation rate constant was similar, yet different to the dissociation rate constant obtained *in vitro*. This could be explained as a consequence of N-WASP regulation due to the formation of a N-WASP-complex by interaction with canonically regulative proteins (e.g. WIP-familiy proteins and Toca1)[28] inside living cells. In a control experiment, with MNPs

functionalized with dominant negative Cdc42 ($Cdc42^{T17N}$), no fluorescence increase at the particle location was observed (data not shown), confirming that the interaction of ^{Cdc42Q61L}MNPs with N-WASP::mEGFP was specific. These experiments demonstrated that immobile MNPs of large size can also be employed as nano-platform for quantitatively probing the stability of bait-prey protein interactions inside living cells.

18 Summary & Conclusions

Cells exhibit a multitude of distinct functions. The maintenance of these functions is often based on the asymmetry of protein distribution and activity. The aim of this collaborative project was to establish methods, which allow the manipulation and probing of protein activities inside living cells at a subcellular scale. Based on magnetic nanoparticles, we developed a method for genetically encoded targeting of specific proteins in combination with magnetic and precise nano-manipulation. In this approach, MNPs were employed as nanoscopic and self-assembled signaling-platforms, which could be spatially manipulated with high accuracy using a magnetic tip. Optogenetic methods and photoactivatable reagents are limited by diffusional spreading of photo activated proteins. By contrast, magnetogenetics enabled manipulation of proteins with micrometer accuracy and maintenance of the spatial restricted signaling for more than 1 hour. By keeping the signaling platform in position, these experiments are only limited by the functional integrity of the conjugated protein and the viability of the cell, respectively. This approach moreover allowed manipulation of endogenous proteins, thereby facilitating the investigation of cellular responses to protein activation under physiological concentrations. This approach was critically dependent on the site-specific and efficient targeting of protein to the surface of MNPs. Based on the engineered HTL-ligand in Chapter II, MNPs were rapidly bio-functionalized with HaloTag fusion proteins directly in the cytoplasm of living cells. The HaloTag technology can also be employed to bio-functionalize MNPs *in vitro,* i.e. by using cell lysates containing the overexpressed HaloTag fusion protein of interest. This is of particular importance with respect to working with genetically un-modified cells under physiological conditions, since it prevents artifacts caused by overexpression of the protein of interest. However, magnetic translocation of 500 nm MNPs was only possible on a time scale of

a few minutes demonstrating a low temporal resolution. To overcome this limitation, smaller stealth MNPs (R_G < 30 nm) without unspecific interactions, which are also not trapped by organelles or in the cytoskeletal meshwork, could significantly enhance the response to magnetic forces. Additionally, small size MNPs can be delivered into cells by pinocytosis.[29] This represents a key prerequisite for systematical studies on cell behavior by up-scaling from the single cell level to multi cell approaches. The application of MNPs as mobile and controllable carrier molecules can readily be extended to other biomolecules (e.g. DNA, mRNA, peptides etc.) whose localization is critical in many biological processes. Overall, magnetogenetics provide a powerful tool with great potential for further applications.

Also, we established a generic approach for specifically probing bait-prey protein interactions in the cytoplasm of living cells based on FRAP. In this method 500 nm MNPs were employed as immobile nanoscopic hot spots. Whereas nanoparticles with R_G < 30 nm are mobile in the cytoplasm, larger particles are entrapped in the cellular environment, which represents an advantage for FRAP applications. An additional advantage of large NPs is given by the high number of proteins, which can be immobilized on the MNP surface (~600–1000 proteins / 500 nm MNP). Thus, the exchange kinetics of Cdc42 interacting with N-WASP were probed with high spatial precision and high contrast. In comparison to conventional intracellular FRAP applications, the resulting recovery curve could simply be fitted using a model for mono-exponential reactions on the precondition where dissociation (k_{off}) is the rate limiting step. For Cdc42 interacting with GBD, dissociation as the rate limiting step was investigated *in vitro*. This criterion can be estimated by comparing characteristic association- and dissociation-times monitored upon micro-injection of bfMNPs into cells and FRAP, respectively. For instance, accociation of Cdc42 interacting with N-WASP *in cellulo* was so fast that only the equilibrium of the interaction could be observed on the particle surface. By contrast, the characteristic dissociation half times were ~30 s, so that dissociation can be assumed as the rate limiting step. Investigating protein activity at a subcellular scale requires methods which allow to probe protein activities with high spatial precision and at defined subcellular locations. This can be realized by utilizing 500 nm MNPs in combination with magnetic nano-manipulation. Furthermore, of general interest is the interrogation of spectroscopic properties to the nanoparticle material. For instance, upconversion nanoparticles could be used for luminescence

resonance energy transfer excitation of target proteins upon excitation with infra-red light, efficiently decreasing background or bleed-trough fluorescence of the donor.[30] In addition, localized surface plasmon resonance of nobel metal nanoparticles such as gold or silver can be exploited as ultra-sensitive biosensors which would enable label free detection of bait-prey protein interactions.[31]

19 References

1. Vartak, N. & Bastiaens, P. Spatial cycles in G-protein crowd control. *EMBO J* **29**, 2689-99 (2010).
2. Scott, J.D. & Pawson, T. Cell signaling in space and time: where proteins come together and when they're apart. *Science* **326**, 1220-4 (2009).
3. Mayer, G. & Heckel, A. Biologically active molecules with a "light switch". *Angew Chem Int Ed Engl* **45**, 4900-21 (2006).
4. Umeda, N., Ueno, T., Pohlmeyer, C., Nagano, T. & Inoue, T. A photocleavable rapamycin conjugate for spatiotemporal control of small GTPase activity. *J Am Chem Soc* **133**, 12-4 (2011).
5. Wu, Y.I. et al. A genetically encoded photoactivatable Rac controls the motility of living cells. *Nature* **461**, 104-8 (2009).
6. Levskaya, A., Weiner, O.D., Lim, W.A. & Voigt, C.A. Spatiotemporal control of cell signalling using a light-switchable protein interaction. *Nature* **461**, 997-1001 (2009).
7. Phillip, Y., Kiss, V. & Schreiber, G. Protein-binding dynamics imaged in a living cell. *Proc Natl Acad Sci U S A* **109**, 1461-6 (2012).
8. Khait, R. & Schreiber, G. FRETex: a FRET-based, high-throughput technique to analyze protein-protein interactions. *Protein Eng Des Sel* **25**, 681-7 (2012).
9. Sprague, B.L. & McNally, J.G. FRAP analysis of binding: proper and fitting. *Trends Cell Biol* **15**, 84-91 (2005).
10. Sprague, B.L., Pego, R.L., Stavreva, D.A. & McNally, J.G. Analysis of binding reactions by fluorescence recovery after photobleaching. *Biophys J* **86**, 3473-95 (2004).
11. Bausch, A.R., Ziemann, F., Boulbitch, A.A., Jacobson, K. & Sackmann, E. Local measurements of viscoelastic parameters of adherent cell surfaces by magnetic bead microrheometry. *Biophys J* **75**, 2038-49 (1998).
12. Bausch, A.R., Moller, W. & Sackmann, E. Measurement of local viscoelasticity and forces in living cells by magnetic tweezers. *Biophys J* **76**, 573-9 (1999).
13. de Vries, A.H., Krenn, B.E., van Driel, R. & Kanger, J.S. Micro magnetic tweezers for nanomanipulation inside live cells. *Biophys J* **88**, 2137-44 (2005).
14. de Vries, A.H., Krenn, B.E., van Driel, R., Subramaniam, V. & Kanger, J.S. Direct observation of nanomechanical properties of chromatin in living cells. *Nano Lett* **7**, 1424-7 (2007).
15. Mannix, R.J. et al. Nanomagnetic actuation of receptor-mediated signal transduction. *Nat Nanotechnol* **3**, 36-40 (2008).
16. Huang, H., Delikanli, S., Zeng, H., Ferkey, D.M. & Pralle, A. Remote control of ion channels and neurons through magnetic-field heating of nanoparticles. *Nat Nanotechnol* **5**, 602-6 (2010).
17. Hoffmann, C. et al. Spatiotemporal control of microtubule nucleation and assembly using magnetic nanoparticles. *Nat Nanotechnol* **8**, 199-205 (2013).
18. Machacek, M. et al. Coordination of Rho GTPase activities during cell protrusion. *Nature* **461**, 99-103 (2009).
19. Iden, S. & Collard, J.G. Crosstalk between small GTPases and polarity proteins in cell polarization. *Nat Rev Mol Cell Biol* **9**, 846-59 (2008).

20. Rudolph, M.G. et al. Thermodynamics of Ras/effector and Cdc42/effector interactions probed by isothermal titration calorimetry. *J Biol Chem* **276**, 23914-21 (2001).
21. Piehler, J., Brecht, A., Valiokas, R., Liedberg, B. & Gauglitz, G. A high-density poly(ethylene glycol) polymer brush for immobilization on glass-type surfaces. *Biosens Bioelectron* **15**, 473-81 (2000).
22. Aoki, K. & Matsuda, M. Visualization of small GTPase activity with fluorescence resonance energy transfer-based biosensors. *Nat Protoc* **4**, 1623-31 (2009).
23. Etoc, F. et al. Subcellular control of Rac-GTPase signalling by magnetogenetic manipulation inside living cells. *Nat Nano* **8**, 5 (2013).
24. Chen, Y.Q. et al. Intracellular viscoelasticity of HeLa cells during cell division studied by video particle-tracking microrheology. *J Biomed Opt* **19**, 11008 (2014).
25. Wirtz, D. Particle-tracking microrheology of living cells: principles and applications. *Annu Rev Biophys* **38**, 301-26 (2009).
26. Michiels, F. et al. Regulated membrane localization of Tiam1, mediated by the NH2-terminal pleckstrin homology domain, is required for Rac-dependent membrane ruffling and C-Jun NH2-terminal kinase activation. *J Cell Biol* **137**, 387-98 (1997).
27. Jaffe, A.B. & Hall, A. Rho GTPases: biochemistry and biology. *Annu Rev Cell Dev Biol* **21**, 247-69 (2005).
28. Stradal, T.E. & Scita, G. Protein complexes regulating Arp2/3-mediated actin assembly. *Curr Opin Cell Biol* **18**, 4-10 (2006).
29. Okada, C.Y. & Rechsteiner, M. Introduction of macromolecules into cultured mammalian cells by osmotic lysis of pinocytic vesicles. *Cell* **29**, 33-41 (1982).
30. Gonzalez, D. et al. Luminescence resonance energy transfer in the cytoplasm of live Escherichia coli cells. *Biochemistry* **50**, 6789-96 (2011).
31. Guo, X. Surface plasmon resonance based biosensor technique: a review. *J Biophotonics* **5**, 483-501 (2012).

V Summary

The aim of my PhD research was to develop and establish techniques for surface functionalization of nanoparticles, which can be employed to study the dynamics, function and activity of recombinantly expressed as well as endogenous proteins inside living cells. A prerequisite to achieve this goal was the ability to bio-functionalize nanoparticles with proteins in the cytoplasm of living cells. The HaloTag technology was utilized for generic site-specific targeting of nanoparticles to proteins. Fast and efficient targeting of nanoparticles to proteins was then achieved by using an engineered clickHTL exhibiting fast reactivity towards the HaloTag-enzyme. Application of this approach to track individual proteins in the outer membrane of mitochondria revealed that the physicochemical properties of the nanoparticles biased the mobility of the targeted proteins. To circumvent this, a model nanoparticle was systematically engineered in order to identify physicochemical properties that are important for tracking intracellular membrane proteins without affecting their diffusion dynamics. Nanoparticles exhibiting stealth properties were finally obtained upon densely coating the nanoparticle surface with PEG_{2k}. These particles were mono-functionalization with clickHTL, to ensure labeling in a 1:1 stoichiometry, and could be successfully used for unbiased tracking of individual membrane proteins. Beyond the observation of proteins, generic approaches that allow intracellular manipulation and probing of protein activities are desired. To this end, 500 nm superparamagnetic nanoparticles were used as mobile nanoscopic hotspots self-assebled into active signaling platforms. Inside living cells, precise and accurate manipulation of endogeneous Rac1 activity was possible at different subcellular locations and over extended time periods. These experiments demonstrated that Rac1 signaling is dependent on the subcellular-context by spatial isolation of distinct signaling pathways. Furthermore, these MNPs provided well defined platforms for selective spectroscopy in order to quantify bait-prey protein interactions in the cytoplasm as was demonstrated by the interaction of cdc42 and N-WASP.

VI Appendix

20 Abbreviations

ACN	Acetonitrile
AEX	anion exchange chromatography
APP	azidophenylpropionic acid
aSEC	analytical size exclusion chromatography
DBCO	Dibenzyl cyclooctyne
DhaA	*Rhododcoccus* dehalogenase
DIPEA	N,N-Diisopropoylethylamine
DMSO	Dimethysulfoxid
DTT	Dithiothreitol
CLSM	confocal laser scanning microscope
DLS	dynamic light scattering
DMF	Dimethylformamid
DOD	degree of degradation
DOF	degree of functionalization
DOL	degree of labeling
EPI	echo planar fluorescence imaging
ESI-MS	Electrospray ionization mass spectrometry
FCS	fluorescence correlations spectroscopy / fetal calve serum
FNPs	fluorescent nanopartilces
FPLC	fast protein liquid chromatography
FRAP	fluorescence recovery after photo bleaching
FRET	Förster resonance energy transfer
GAP	GTPase-activating protein
GEF	guanine nucleotide-exchange factor

HBTU	*O*-(Benzotriazol-1-yl)-N,N,N',N'-tetramethyluronium hexafluorophosphate
HPLC	high performance liquid chromatography
HT	HaloTag-protein
HTL	HaloTag-ligand
LCF	light chain Ferritin
LSPR	localized surface plasmon resonance
MEM	minimum essential medium
MNPs	magnetic nanoparticles
MPA-NHS	3-(Maleimido)propionic acid N-Hydroxy-succinimide ester
MTT	multi-target tracing
NEAA	non-essential amino acids
NHS	N-Hydroxysuccimide
NPs	nanoparticles
PPI	protein-protein interaction
QDs	Quantum dots
R_G	radius of gyration
Rif	reflectance interferometry
SEC	size exclusion chromatography
TIRFM	total internal reflection fluorescence microscopy
TIRFS	total internal reflection fluorescence spectroscopy
TFA	Trifluoro acetic acid
TMR	Tetramethylrhodamine
TOPO	

21 Curriculum Vitae

Name:	Domenik Liße
Date of birth:	27.02.1980
Place of Birth:	Köln
Address:	Wersenerstraße 104a, 49090 Osnabrück

Eduction

09/97-02/01	**Chemical technician** Dystar GmbH Leverkusen
09/02-06/03	**Advanced technical certificate** Technical Secondary School Leverkusen
10/03-09/08	**Graduate engineer of Biotechnology** University of Applied Science Aachen
03/09-Present	**Promotion** University of Osnabrück – Division of Biophysics

---

Work Experience

02/01-11/01	**Chemical technician; organic chemical syntheses of dyes** Dystar GmbH Leverkusen
01/02-08/02	**Chemical technician; extraction, purification and reprocessing of phospholipids** Nattermann GmbH Köln

22 Publications

D. Liße, C. P. Richter, C. Drees, O. Birkholz, C. You, J. Piehler; Mono-functional stealth nanoparticles enables unbiased tracking of membrane proteins inside living cells. *In preparation*

F. Etoc, D. Liße, Y. Bellaiche, J. Piehler, M. Coppey, M. Dahan; Subcellular control of Rac-GTPase signalling by magnetogenetic manipulation inside living cells. (2013) *Nature Nanotechnology* **8**, 193-198

C. You, S. Wilmes, C. P. Richter, O. Beutel, D. Liße, J. Piehler; Electrostatically controlled quantum dot monofunctionalization for interrogating the dynamics of protein complexes in living cells. (2012) *ACS chemical biology* **8(2),** 320-326

S. Wilmes, M. Staufenbiel, D. Liße, C. P. Richter, K. Busch, S. Hess, J. Piehler; Triple-Color Super-Resolution Imaging of Live Cells: Resolving Submicroscopic Receptor Organization in the Plasma Membrane. (2012) *Angewandte Chemie Int. Ed.* **124**, 4868-4871

D. Liße, V. Wilkens, C. P. Richter, K. Busch, J. Piehler: Specific targeting of nanoparticles to proteins inside living cells; (2011) *Angewandte Chemie Int. Ed.* **50,** 9352-9355

Declaration

I hereby declare that the presented thesis “Surface functionalization of nanoparticles for probing and manipulation of proteins inside living cells” was prepared entirely on my own and I have not used outside sources without declaration in the text. Any concepts or quotations applicable to these sources are clearly attributed to them. I have not attempted a promotion before.

Osnabrück, 5th November 2013 Domenik Liße